

**Multiphase Flow Modelling of Electrochemical Systems
an analytical approach**

Rajora, A.

DOI

[10.4233/uuid:62479ffc-c389-4d3d-8320-f7b3ad8d0829](https://doi.org/10.4233/uuid:62479ffc-c389-4d3d-8320-f7b3ad8d0829)

Publication date

2023

Document Version

Final published version

Citation (APA)

Rajora, A. (2023). *Multiphase Flow Modelling of Electrochemical Systems: an analytical approach*. [Dissertation (TU Delft), Delft University of Technology]. <https://doi.org/10.4233/uuid:62479ffc-c389-4d3d-8320-f7b3ad8d0829>

Important note

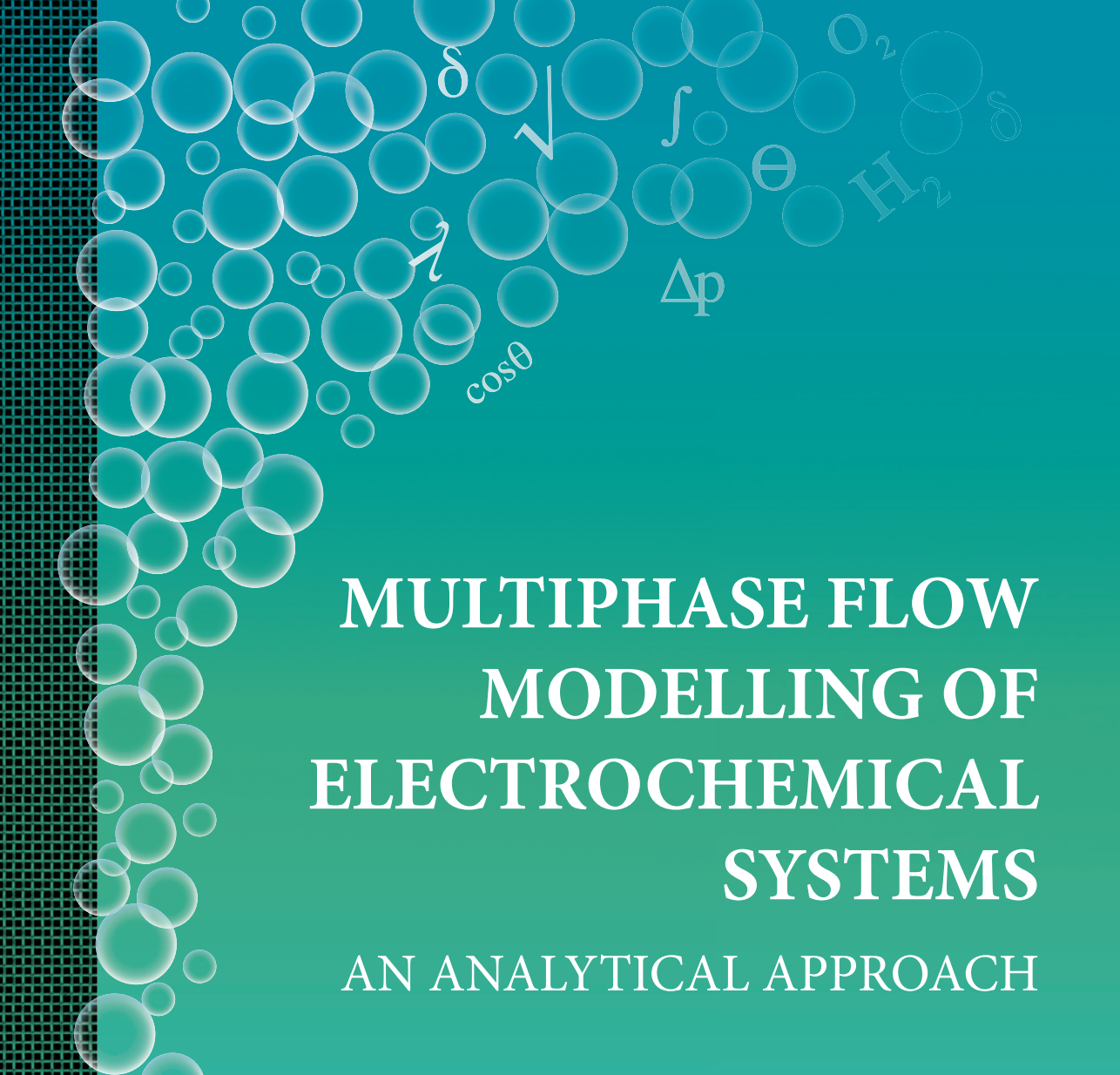
To cite this publication, please use the final published version (if applicable).
Please check the document version above.

Copyright

Other than for strictly personal use, it is not permitted to download, forward or distribute the text or part of it, without the consent of the author(s) and/or copyright holder(s), unless the work is under an open content license such as Creative Commons.

Takedown policy

Please contact us and provide details if you believe this document breaches copyrights.
We will remove access to the work immediately and investigate your claim.



MULTIPHASE FLOW MODELLING OF ELECTROCHEMICAL SYSTEMS

AN ANALYTICAL APPROACH



Aviral Rajora

MULTIPHASE FLOW MODELLING OF ELECTROCHEMICAL SYSTEMS

AN ANALYTICAL APPROACH

MULTIPHASE FLOW MODELLING OF ELECTROCHEMICAL SYSTEMS

AN ANALYTICAL APPROACH

Dissertation

for the purpose of obtaining the degree of doctor
at Delft University of Technology,
by the authority of the Rector Magnificus prof.dr.ir. T.H.J.J. van der Hagen,
chair of the Board for Doctorates,
to be defended publicly on
Wednesday 14 June 2023 at 15:00 o'clock

by

Aviral RAJORA

Master of Science in Mechanical Engineering,
Delft University of Technology, The Netherlands,
born in Pantnagar, India.

This dissertation has been approved by the promotor.

Composition of the doctoral committee:

Rector Magnificus,	chairperson
Prof. dr. ir. J. T. Padding,	Delft University of Technology, promotor
Dr. ir. J. W. Haverkort,	Delft University of Technology, copromotor

Independent members:

Prof. dr. F. M. Mulder	Delft University of Technology
Prof. dr. ir. R. Pecnik	Delft University of Technology
Prof. dr. ir. A. W. Vreman	Technische Universiteit Eindhoven
Prof. dr. P. Mandin	Universite Bretagne Sud, France
Dr. ir. D. A. Vermaas	Delft University of Technology



Copyright © 2023 by A. Rajora

ISBN 978-94-6469-410-9

An electronic version of this dissertation is available at
<http://repository.tudelft.nl/>.

To my father who's shown me what it means to persevere

I dedicate this thesis with love and admiration

and to late Dr. A. P. J. Abdul Kalam

who showed me that our dreams can be realized through hardwork and dedication and
that our potential is limitless if we have the courage to pursue it

CONTENTS

1	Introduction	1
1.1	Societal Relevance	2
1.2	Multiphase Flow in Electrochemical Cells	4
1.3	This Thesis	6
2	An Analytical Model for Liquid and Gas Diffusion Layers in Electrolyzers and Fuel Cells	9
2.1	Introduction	10
2.2	Mathematical model	11
2.2.1	Model equations	11
2.2.2	Boundary condition	14
2.3	Analytical solutions	15
2.3.1	Analytical solution for the saturation.	15
2.3.2	Analytical solution for the maximum current	16
2.3.3	Interpretation	17
2.4	Performance losses in a diffusion layer	18
2.4.1	Activation overpotentials η	18
2.4.2	Wetting overpotential η_χ	18
2.4.3	Concentration overpotential η_c	19
2.4.4	Effective diffusivity D_{eff}	20
2.4.5	Diffusion limited current density j_{lim}	20
2.5	Results and Discussions.	22
2.5.1	Verification of the analytical model	22
2.5.2	Maximum current density	24
2.5.3	Limiting current density	24
2.5.4	Mass transport losses	25
2.5.5	Design limitations on \bar{L}	25
2.6	Conclusions.	26
3	Multiphase flow model for membraneless gas-evolving flow-through porous electrodes	35
3.1	Introduction	36
3.2	Multiphase flow-through electrode model	38
3.2.1	Governing equations.	38
3.2.2	Numerical solutions	39
3.2.3	Analytical solution	40
3.3	Experimental validation.	41
3.4	Discussion	43
3.5	Conclusion	44

4	An Analytical Multiphase Flow Model for Parallel Plate Electrolyzers	47
4.1	Introduction	48
4.2	Mathematical Model	48
4.2.1	Model Configuration	48
4.2.2	Numerical Model	49
4.3	Analytical Model	51
4.3.1	Volume fraction	52
4.3.2	Plume thickness	52
4.3.3	Governing equation and boundary conditions	52
4.3.4	Electrolyte velocity	53
4.3.5	Electrode surface gas fraction	54
4.3.6	Pressure Drop	55
4.3.7	Wall shear stress	56
4.4	Validation and Discussions	56
4.4.1	Validation of Numerical Model	56
4.4.2	Validation of Analytical Model	63
4.5	Design Guidance	65
4.6	Conclusions.	68
5	An analytical model for the velocity and gas fraction profiles near gas evolving electrodes	75
5.1	Introduction	76
5.2	Model Equations	77
5.3	Analytical model	79
5.3.1	Exponential gas fraction profile	80
5.3.2	Step-function gas fraction profile	81
5.4	Verification using Numerical Solutions	85
5.5	Conclusions.	91
6	Summary, Discussion, and Outlook	99
	References	105
	List of Publications	117
	Acknowledgments	119

LIST OF SYMBOLS

Abbreviations

AEM	Anion Exchange Membrane
CL	Catalyst Layer
DL	Diffusion Layer
FC	Fuel Cell
GDE	Gas Diffusion Electrode
GDL	Gas Diffusion Layer
PEM	Proton Exchange Membrane
WE	Water Electrolyzer

Dimensionless variables

\bar{j}	Current density j / j_i
\bar{L}	dimensionless DL thickness $\bar{L} \equiv r_{\max} L / K$
χ	Wetted fractional surface area, [-]
$\bar{\delta}$	dimensionless plume thickness = $\frac{\delta_g}{l}$
ϵ	Porosity, [-]
λ	Pore size distribution index $p_c = p_t s^{-1/\lambda}$
\mathcal{E}	Effectiveness factor, [-]
Pr_b	bubble Prandtl number
Θ	Fractional bubble coverage, [-]
ϵ	gas fraction
c_1	Material constant $K / \epsilon^3 d_{\max}^2$, [-]
k_i	Relative permeability
m	Exponent in $D = D_0 \epsilon^m$
n	Exponent in $D_{\text{eff}} = D s^n$

q	Exponent in $k_w = s^q$ (chapters 2 and 3); $q \equiv \delta_f/\delta_g$ (chapters 4 and 5)
r	Order of the reaction
s	Saturation of the <i>wetting</i> phase (chapter 2), liquid saturation (chapter 3)
z_i	Stoichiometric coefficient
Re	Reynolds number

Subscripts and other notation

'	Derivative $d/d\bar{x}$ in chapter 3 and derivative d/dx in chapter 2
-, +	Left (-) or right (+) of interface
0	properties at $x = 0$
1	DL-CL interface, $\bar{x} = 1$
-	Dimensionless quantity
a	anode
c	cathode
nc	properties for flow due to natural convection
~	Pertaining to catalyst layer
g	gaseous property
m	mixture property
max	maximum value of the variable
min	minimum value of the variable
s	slip
\hat{x}	unit vector in horizontal direction
\hat{z}	unit vector in vertical direction
i	Phase index n or w
I_n^λ	$\equiv \int (1-s)^3 ds^{-1/\lambda}$
I_w^λ	$\equiv \int s^3 ds^{-1/\lambda}$
n	Non-wetting phase
w	Wetting phase
*	When $\frac{\bar{J}_n}{(1-s)^3} = \frac{\bar{J}_w}{s^3}$

Symbols

$\langle W \rangle$	average vertical superficial liquid velocity, [m/s]
\mathcal{A}	dimensional constant in $\delta_g = \mathcal{A} \frac{z^a}{\langle W \rangle^b}$, [m ^{1+b-a} /s ^b]
z	vertical coordinate [m]
d_b	bubble diameter, [m]
δ_f	flow boundary layer thickness [m]
δ_g	gas plume thickness [m]
η	Activation overpotential, [V]
η_c	Concentration overpotential, [V]
η_χ	Wetting overpotential, [V]
κ	Effective electrode conductivity $\approx \kappa_0 \epsilon^{1.5}$, [-]
U	superficial velocity vector given by $U\hat{x} + W\hat{z}$
μ	Dynamic viscosity, [Pa·s]
ν	kinematic viscosity [m ² /s]
ρ	Density, [kg/m ³]
σ	Surface tension, [N/m]
U	superficial velocity in the x direction [m/s]
W	characteristic velocity in Eq. (5.8) [m/s]
θ	Contact angle, [rad]
u	interstitial velocity in the x direction [m/s]
w	interstitial velocity in the z direction [m/s]
w'	strain rate at the electrode $\equiv \left. \frac{\partial w}{\partial x} \right _{x=0}$ [1/s]
w_b	$\equiv \frac{\rho g l^2}{12\mu}$, characteristic velocity due to buoyancy, [m/s]
u	interstitial velocity vector given by $u\hat{x} + w\hat{z}$
\mathcal{V}_m	molar volume, [m ³ /mol]
$\langle W_g \rangle$	average vertical superficial gas velocity, [m/s]
b	Tafel slope, [V]

C	Reactant inlet concentration, [mol/m ³]
c	Reactant concentration, [mol/m ³]
D_0	Reactant diffusivity, [m ² /s]
D_b	Bubble diffusion coefficient [m ² /s]
d_b	bubble diameter [m]
D_{eff}	Effective diffusivity $\frac{D}{\int_0^1 s^{-n} d\bar{x}}$, [m ² /s]
d_{max}	Maximum pore diameter, [m]
D	Reactant diffusivity in porous medium, $D = D_0 e^m$ [m ² /s]
F	Faraday constant 96485.3329, [C/mol]
g	acceleration due to gravity, [m/s ²]
h	height of the electrode, [m]
i	Local electronic current density, [A/m ²]
j	Current density magnitude, [A/m ²]
j_i	See Eq. (2.7) $j_i = J_i / \bar{L}$ [A/m ²]
j_*	Exchange current density, [A/m ²]
$j_{\text{iim}0}$	Single phase limiting current density $j_{\text{iim}0} = \frac{FDc_0}{z_w L}$ [A/m ²]
j_{lim}	Limiting j when $c_1 = 0$, [A/m ²]
j_{max}	Maximum j when $s_1 = s_{\text{min}}$, [A/m ²]
K	Absolute permeability, [m ²]
L	Thickness of the diffusion layer in chapter 2 and electrode thickness in chapter 3 [m]
l	electrode-wall distance [m]
l	inter-electrode gap in chapter 4 and electrode-wall distance in chapter 5, [m]
P	reduced pressure = $p + \rho g z$, [Pa]
p	Pressure, [Pa]
p_c	Capillary pressure, [Pa]
p_t	Threshold pressure, [Pa]
R	Gas constant 8.31446, [J/mol/K]

r_{\max}	Maximum pore radius, [m]
T	Operating temperature, [K]
w_p	$\equiv -\frac{\partial P}{\partial z} \frac{l^2}{12\mu}$, characteristic velocity due to pressure gradient, [m/s]
x	Coordinate across DL in chapter 2, across the electrode in chapter 3 and across the gap in chapters 4 & 5, [m]
z_{eff}	height at which the analytical flow rate matches the numerical flow rate [m]

1

INTRODUCTION

1.1. SOCIETAL RELEVANCE

As per Intergovernmental Panel on Climate Change [1], the rise in global mean surface temperature (GMST) beyond 1.5° C from pre-industrial (1850 AD-1900 AD) level has associated impacts such as increased frequency of heatwaves, increased intensity of heavy precipitation events and droughts, and rise in sea level. This will severely impact health, food security, economic growth, and overall loss of biodiversity. Due to the rapid industrialization and human activities, the emissions of greenhouse gases have already increased the GMST by approximately 1.3° C (<https://globalwarmingindex.org/>) compared to the pre-industrial revolution level, see Fig. 1.1 reproduced from <http://www.columbia.edu/~mhs119/Temperature/>, using the monthly updates of global temperature. If the current unconstrained rise ($\approx 0.18^\circ$ per decade) in GMST continues, a 1.5° increase in GMST could occur before 2040. Therefore, immediate mitigation strategies are needed at multiple frontiers to minimize the negative impacts of climate change.

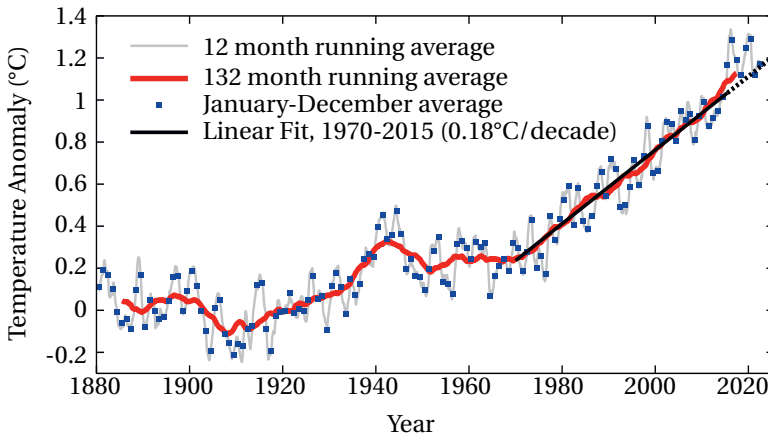


Figure 1.1: Evolution of global mean surface temperature over time relative to 1880-1920 average showing a rapid and sustained increase post the industrial revolution. Figure reproduced from the monthly updates of global temperature on <http://www.columbia.edu/~mhs119/Temperature/>

At the heart of these mitigation strategies lies the transition from non-renewable fossil fuel energy resources to renewable energy resources such as wind and solar. These energy sources are intermittent and unevenly distributed across the earth. However, the demand for energy is relatively constant. As such, we require large-scale energy storage solutions to make renewable energy a viable alternative to non-renewable energy sources. The role of hydrogen in energy transition has been recognized across the globe [2–4]. It is arguably well-placed as a promising energy carrier and is expected to play a crucial role in decarbonization through its use as industrial feedstock [5] and secondary energy source. The global demand for hydrogen is projected to increase seven-fold from 70 million metric tonnes in 2019 to more than 500 million metric tonnes in 2070 in the sustainable development scenario [6]. Therefore, it is critical that hydrogen production and its use is clean, sustainable, and economical.

One of the existing ways of producing clean hydrogen is using water electrolyzers. Water electrolyzers can use electrical energy from renewable sources and split water into hydrogen and oxygen. The produced hydrogen can be used later to generate electricity using fuel cells or as an industrial feedstock to produce useful chemicals such as ammonia and hydrogen peroxide. Water electrolysis accounts for only 4% of the total hydrogen production [7, 8]. However, decreasing capital cost, increasing production rate and efficiency, decreasing cost of renewable electricity, and increasing carbon taxes will help water electrolyzers gain a competitive advantage over less sustainable hydrogen production processes. In the sustainable development scenario, more than half of the hydrogen is expected to be produced through electrolysis [8], see Fig. 1.2.

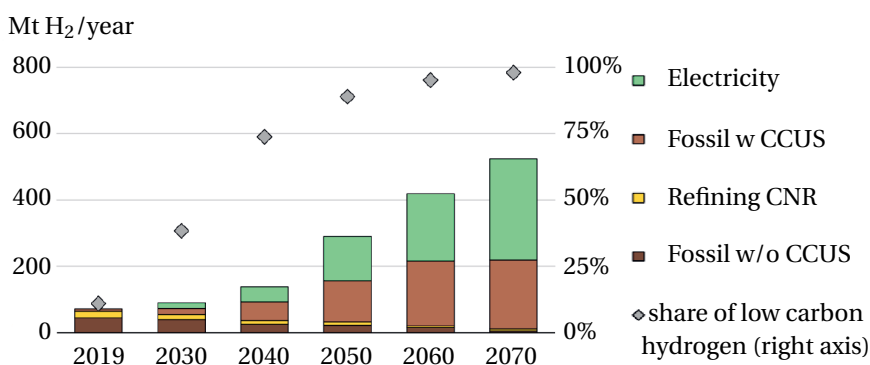


Figure 1.2: Global hydrogen production by technology in Sustainable Development scenario of International Energy Agency. Figure taken from the report on Energy Technology Perspectives, 2020 [8].

While the electrolyzer technology is not new, research efforts are ongoing to improve it further. From an electrochemical point of view, researchers are looking for more durable, cheaper, and better catalysts through morphology control and doping [9–14]. Emphasis on the scale-up of electrochemical cells has led to fundamental research in gas evolution near the electrodes and resulting multiphase hydrodynamics inside such devices.

High current density operation of electrochemical cells, required for higher production rate, inevitably produces a large amount of gas near the electrodes. Due to the increased amount of gas and usually low solubility of gases in liquid electrolytes, gas bubbles are formed leading to multiphase flow hydrodynamics in the electrochemical devices. Due to the low conductivity of the gas bubbles, the ohmic resistance of the whole cell may increase. The evolved gas bubbles may also block a part of the reactive surface area of the electrode, further increasing the losses in the electrochemical cell. Therefore, the performance of an electrochemical device is closely linked to its multiphase hydrodynamics.

1.2. MULTIPHASE FLOW IN ELECTROCHEMICAL CELLS

Different types of multiphase flow can occur in an electrochemical cell depending on its configuration. We will briefly discuss the relevant configuration for this work. Conventional proton exchange membrane (PEM) fuel cells and electrolyzers have a membrane electrode assembly (MEA) consisting of a diffusion layer, catalyst layer, and a membrane as shown in Fig. 1.3. Darcy flow may occur in the porous diffusion layer in electrochemical cell configurations, where the gas and liquid move through very small pores due to the capillary pressure gradient. The capillary pressure depends on the relative saturation of the two phases and the pore structure of the diffusion layer. While many researchers have studied the transport of gases and liquids in porous diffusion layers through numerical simulations and experiments, very few attempts have been made to study such flows analytically.

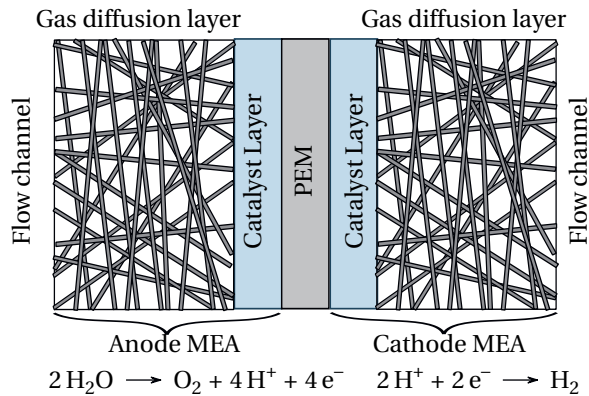


Figure 1.3: Schematic of a Membrane electrode assembly commonly used in PEM/AEM fuel cells and electrolysis. The reaction shown at the bottom is for PEM electrolysis.

Another configuration where Darcy flow may occur is porous flow through electrodes recently proposed for membraneless electrolysis operation. Membraneless flow through electrolyzer uses flow to avoid gases crossing over to the opposing electrodes, as shown in Fig. 1.4. This has the advantage that costs, resistance and potential degradation associated with the membrane or a separator are not present. However, the geometrical design parameters such as electrode thickness, height, gap thickness, and pore size may directly affect the pumping power for the required flow rate. The current design of the membraneless electrolyzer is mostly influenced by previous experimental studies, and an analytical understanding of the design is limited.

Membraneless electrochemical cells can operate in another configuration with parallel plate electrodes, as shown in Fig. 1.5. In such electrolyzers, the gas evolves as dispersed bubbles at both electrodes and moves in a plume that grows in thickness along the height of the electrode. The gas plume may set the liquid electrolyte in motion due to buoyancy. Many researchers in the past have studied this configuration, mostly with the help of experiments and numerical simulations. A few attempts have also been made to understand the multiphase flow in such a configuration. However, a simple analytical

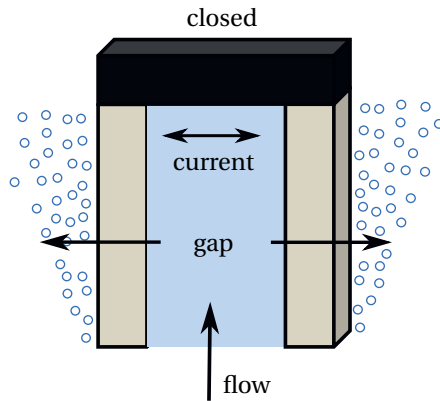


Figure 1.4: A schematic view of flow-through configuration considered with, inside the porous electrodes, flow *parallel* to the current, *outwards* from the gap, *through* the electrodes. The liquid pushes the gas bubbles to the backside of the electrodes [15].

relation for the maximum allowable height for a given electrode gap and current density is still missing from the literature. Such a design equation would be very helpful in the initial design estimates for electrochemical cells.

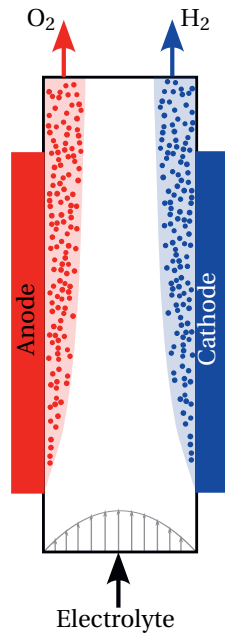


Figure 1.5: A schematic view of membraneless parallel plate electrolyzer. The bubbles are generated on the electrode surface and move inside the inter/electrode gap. The flow, either forced or buoyancy/driven, is used to separate the two gases. The shaded region represents the gas plume

The gas bubble plumes are also relevant for another potentially useful configuration of a zero-gap electrochemical cell, as shown in Fig. 1.6. The two electrodes are brought very close to the membrane or a separator in a zero-gap electrochemical cell. This results in a much shorter distance between the electrolyte, leading to a smaller ohmic resistance of the electrolyte. As there is little or no space between the electrodes and the separator, the gas is released at the back of the electrode, forming a gas plume in the channel behind the electrodes. A similar configuration is also relevant for traditional alkaline water electrolyzers where a single gas plume is formed between the electrode and the membrane. Analytical characterization of the gas plumes in such configurations is required before establishing analytical design principles.

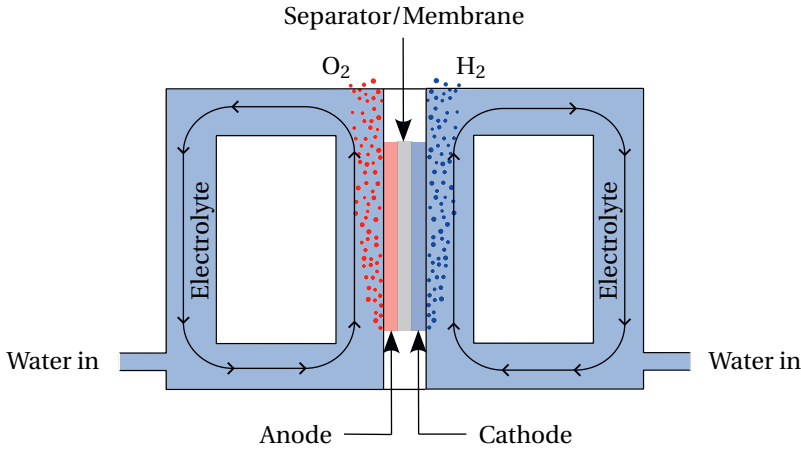


Figure 1.6: A schematic representation of the zero-gap electrolyzer. The gas is generated on the back side of the electrode. The gas bubbles rise due to buoyancy and induce a buoyancy-driven electrolyte flow in the chamber. The chamber is replenished with water from the bottom of the electrolyte chamber.

1.3. THIS THESIS

The primary objective of this work is to provide new analytical models to support the theoretical understanding of multiphase flows in various electrochemical systems. Most of the previous works in this field use either experiments or numerical simulations to understand the hydrodynamics of the multiphase flows. In this thesis, various new analytical models are derived for different cell configurations discussed in section 1.2 and new design equations are provided that can be readily used as a first estimate for a new electrochemical cell. The novelty of this work lies in providing new analytical approaches to develop a theoretical understanding of electrochemical cells.

RESEARCH QUESTIONS AND OUTLINE

In particular, this thesis answers the following specific research questions in the subsequent chapters:

CHAPTER 2

"How does multiphase flow influence the limiting current in a gas diffusion layer?"

To answer this question, a new analytical framework in 1-D based on visco-capillary equations is provided that provides simple relations for liquid saturation, effective diffusivity, and limiting current density taking into account the pore size distribution of a porous diffusion layer.

CHAPTER 3

"What is the minimum velocity required to operate a membraneless flow-through electrolyzer effectively?"

A relation for the minimum required velocity that avoids bubbles entering the gap is derived using the visco-capillary equations to answer this question.

CHAPTER 4

"What is the maximum height of a parallel plate electrolyzer without a separator at a given operating condition using only buoyancy-driven flow?"

Using a mixture model formulation, a simplified semi-analytical framework is proposed for multiphase flow in a parallel plate electrolyzer without a separator. This framework provides simple relations for electrode surface gas fraction, pressure drop, and the maximum height of the electrolyzer.

CHAPTER 5

"How does the gas plume thickness, electrode surface gas fraction, peak liquid velocity and flow rate scale with the height and current density of the electrolyzer?"

First, a certain velocity profile and gas fraction profile are assumed based on numerical simulations. Using these profiles in the mixture model equations and integrating them over the control volume, scaling laws are derived for the useful quantities listed in the research question.

CHAPTER 6

This chapter summarizes the key findings of this thesis, addresses their limitations, and proposes future research outlook based on the insights gained from this thesis.

2

AN ANALYTICAL MODEL FOR LIQUID AND GAS DIFFUSION LAYERS IN ELECTROLYZERS AND FUEL CELLS

The diffusion layer is a crucial part of most fuel cells and electrolyzers. We analytically solve a simplified set of visco-capillary equations for the gas and liquid saturation profiles inside such layers. Contrary to existing numerical simulations, this approach allows us to obtain general scaling relations. We derive simple explicit equations for the limiting current density associated with reactant starvation, flooding, and membrane dehydration, including the effect of fluid properties, contact angle, tortuosity, and the pore size distribution. A more even pore size distribution generally allows higher currents. Explicit expressions for the minimum pore size and maximum layer thickness show that modern diffusion layers are typically well-designed.

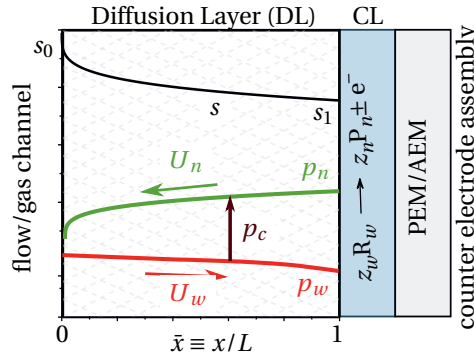


Figure 2.1: Illustrative profiles of s , p_n , and p_w throughout a diffusion layer. The wetting-phase saturation s is the volume fraction of the wetting phase reactant R_w relative to the total fluid volume. It runs between s_0 at $x = 0$ at the channel-DL interface and s_1 at $x = L$ at the DL-CL interface. The difference between the non-wetting phase pressure p_n and wetting phase pressure p_w is the capillary pressure p_c . The wetting and non-wetting phases moves with a superficial velocity \mathbf{U}_w and \mathbf{U}_n to the left and right, respectively. As a result the capillary pressure always increases and the saturation always decreases in the direction of \bar{x} .

2.1. INTRODUCTION

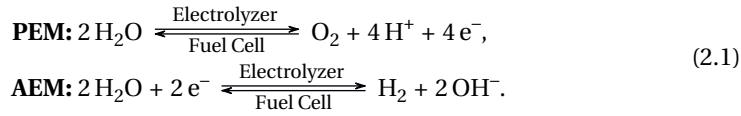
Increased awareness of greenhouse gases has prompted accelerated efforts for switching to renewable and cleaner sources of energy. Primary renewable energy sources like solar and wind have intermittent supply and hence require energy storage [17]. Hydrogen is an attractive energy carrier that can be obtained sustainably through electrolysis of water [18] and converted back to electricity using fuel cells [19, 20].

Fuel cells (FC) and water electrolyzers (WE) generally consists of a membrane electrode assembly (MEA) comprising a diffusion layer (DL), catalyst layer (CL), and a membrane, as shown in Fig. 2.1. The membrane is often a polymer electrolyte membrane (PEM) that transports cations, like protons, or an anion exchange membrane (AEM) that transports anions, like hydroxyl ions. The membrane serves to separate the reactants and the products formed at the two electrodes. The diffusion layer facilitates the transport of reactants and products to and from the catalyst layer. It provides an electrical connection between the catalyst layer and the current collector and provides the mechanical strength to allow high-pressure operation. Simultaneously, reaction products should be able to leave through the diffusion layer, while reactants move in the opposite direction to the catalyst layer. Therefore in the case of gaseous reactants and liquid products, as in a hydrogen fuel cell, for example, a *hydrophobic* gas diffusion layer (GDL) is used. The hydrophobicity makes the reactant gases the wetting phase, facilitating the transport of gases into the system. For the same reason, a *hydrophilic* diffusion layer is used in, for example, water electrolyzers, where water is the wetting phase. Reference [21] illustrates an exception where a hydrophobic layer is used to obtain bubble-free alkaline water electrolyzer operation, which requires water to be supplied from the opposite direction.

Figure 2.1 shows the transport of the wetting and non-wetting phases across the dif-

fusion layer.

For PEM/AEM water electrolyzers and hydrogen fuel cells, the half-reactions in which liquid and gas phases move in opposite directions, are written as:



In both fuel cells and water electrolyzers, water management is crucial. In water electrolyzers, water is the reactant and water starvation should be avoided [22, 23]. Accumulation of oxygen in the anode catalyst layer is often held responsible for observed mass transport losses [24] although the origin is still very much under debate [25] and various, arguably less convincing hypotheses, have recently been proposed [26, 27].

In hydrogen fuel cells, too much product water can flood the diffusion layer, preventing the reactant gases from reaching the catalyst layer [28]. On the other hand, some water needs to be present to hydrate the membrane sufficiently for it to remain well conducting.

Various studies [29–33] provide models and insights, focusing on a single application. Here, we highlight the similarities in transport between different applications in which gases and liquids move in opposite directions. This is relevant for a wide range of applications including AEM/PEM hydrogen fuel cells [34–36], water electrolyzers (WE) [37, 38], direct alcohol fuel cells [39] like direct methanol fuel cells (DMFC) [40, 41] and direct ethanol fuel cells (DEFC) [42, 43], alkaline anion exchange membrane (AAEM) fuel cells [44], and CO₂ gas diffusion electrodes (CO₂-GDE) [45–48].

We assume that in the diffusion layer no phase change occurs, which is a good approximation when a gaseous phase enters fully saturated. This allows us to provide explicit formulas that would enable engineering estimates, provide useful insight into the relevant parameters and their scalings, can be used for analytical optimization, and in real-time energy management systems.

We first introduce the model equations and their approximate analytical solutions. We define and provide expressions for the limiting current density and overpotentials associated with the diffusion layer. We discuss the accuracy of the analytical model by comparing with numerical solutions and, finally, summarize the key insights gained from the model.

2.2. MATHEMATICAL MODEL

2.2.1. MODEL EQUATIONS

Using a multiphase Darcy model [49–52] in 1-D, we write the pressure gradient of a phase i as:

$$\frac{dp_i}{dx} = -\frac{\mu_i U_i}{K k_i}, \quad (2.2)$$

where the *phase index* $i = w, n$ denotes either the wetting or non-wetting phase, U_i is the x -component of the *superficial velocity*, which can be both positive or negative, μ_i is the dynamic viscosity, k_i is the relative permeability, and K is the absolute permeability.

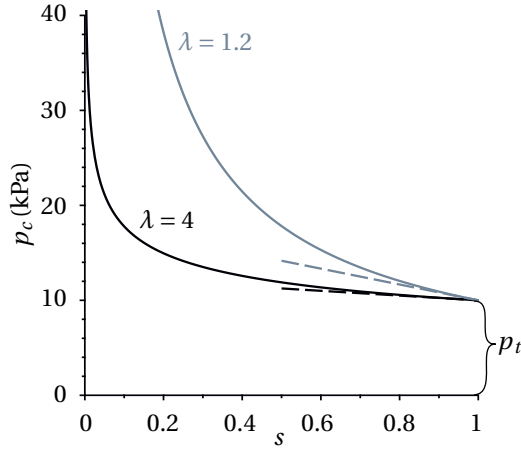


Figure 2.2: Capillary pressure curves for different pore size distribution index λ for $p_t = 10$ kPa. The dashed lines show the linearization $p_c = p_t \frac{1+\lambda-s}{\lambda}$ near $s = 1$ for the two different values of λ .

The above equation assumes that both phases independently obey the Darcy law, i.e., there is no mutual friction between the two phases. This is generally true in the case of fuel cells and electrolyzers where the reactant and products are in the gaseous and the liquid phases. Depending on the hydrophobicity of the porous medium, the gas, and the liquid will encounter varying degrees of resistance depending on the pore size and tortuosity of the medium. Consequently, the gases and liquid will form separate continuous pathways in different regions of the porous diffusion layers. For example, in the case of fuel cells, with hydrophobic diffusion layers, the liquid will be localized in the large pores with smaller threshold pressure, while the gas will occupy the small pores.

Using Faraday's law

$$U_i = \pm \frac{z_i V_i}{F} j, \quad (2.3)$$

with a plus sign for $i = w$ and a minus sign for $i = n$. Here j is magnitude of the total current density, V_i is the molar volume¹, F is Faraday's constant, and z_i is the stoichiometric coefficient introduced in Fig. 2.1.

The relative permeabilities are expressed as $k_w = s^q$ and $k_n = (1-s)^q$ [50], where s is the saturation of the wetting phase. In this work we use $q = 3$, although different powers between 2 and 8 have also been used in the recent literature [30]. We provide expressions for general q in 2.D.

The capillary pressure is the pressure difference between the non-wetting and the wetting phase. Various models are proposed in the literature, like the Leverett-Udell model [49, 53], the Van-Genuchten model [54], the Brooks-Corey model [55] or analytical fractal models [56, 57]. The Leverett-Udell model is an empirical model that relates

¹2.C illustrates that V_i corresponds to the total molar volume, not the partial molar volume of the reaction or product species in case of mixtures. For an ideal gas, $V_i = RT/p_i$, where R is the gas constant, p_i is the partial pressure and T is the operating temperature.

the water content to the capillary pressure using a capillary pore radius distribution. It assumes that the soil is composed of identical pores with a log-normal distribution of radii. The Brooks-Corey model, on the other hand, is a more mechanistic model that assumes that a power-law distribution of pore sizes. The Van-Genuchten model assumes the presence of at least one interconnected pore-pathway that contains pores of sufficient size such that capillary pressure can be disregarded. The primary distinction between the Van-Genuchten and Brooks-Corey models is that while the Brooks-Corey model includes an entry pressure (where capillary pressure is non-zero at unity saturation), the Van-Genuchten model does not. The analytical fractal model is more complex and accounts for fractal nature of pore structure. It is computationally demanding and requires detailed information of the pore structure. We use the Brooks-Corey relation [58–60], because of its mathematical simplicity, to describe the capillary pressure as

$$p_c \equiv p_n - p_w = p_t s^{-1/\lambda}. \quad (2.4)$$

For hydrophilic layers, s is the liquid saturation, while for hydrophobic layers, s is the gas saturation.

The threshold displacement pressure may be related to the surface tension σ and contact angle θ by the Young-Laplace equation, that is valid for the capillary pressure when the pores would form cylindrical channels of radius r_{\max} , as

$$p_t = \frac{2\sigma |\cos(\theta)|}{r_{\max}}. \quad (2.5)$$

In a general porous medium Eq. (2.5) may be seen as the definition of p_t , loosely related to the maximum pore size r_{\max} . A high value of the pore size distribution index λ is associated with a relatively flat capillary pressure curve, as illustrated in Fig. 2.2. This is associated with a more narrow pore size distribution, with most pores near the maximum pore size, and only a small fraction of smaller pores. Lower values of λ correspond to wider pore size distributions.

Combining Eq. (2.2) and (2.3) with Eq. (2.4), using $\bar{x} = x/L$, we obtain

$$\frac{ds^{-1/\lambda}}{d\bar{x}} = \frac{\bar{j}_n}{(1-s)^3} + \frac{\bar{j}_w}{s^3}, \quad (2.6)$$

where $\bar{j}_i = k_i |d(p_i/p_t)/d\bar{x}| = \mu_i |U_i|/p_t K$ is a dimensionless pressure gradient or velocity. With Eq. (2.3) it can also be seen as a dimensionless current density. Note that because the wetting phase moves in the positive x -direction and the non-wetting phase in the negative x -direction, both terms in Eq. (2.6) are positive, despite the minus sign in Eq. (2.4). With $\frac{ds^{-1/\lambda}}{d\bar{x}} = -\frac{1}{\lambda} s^{-\frac{1}{\lambda}-1} \frac{ds}{d\bar{x}}$ we thus see that s is a monotonously decreasing function of \bar{x} .

With Eqs. (2.2) and (2.3) we can write $\bar{j}_i = j/j_i$ where

$$j_i = \frac{p_t K}{\mu_i L} \frac{F}{z_i V_i} = \frac{\overbrace{2\sigma |\cos(\theta)| F}^{J_i}}{V_i \mu_i z_i} \overbrace{\frac{1}{r_{\max} L}}^{1/L}. \quad (2.7)$$

It should be noted that for applications like air fuel cells there will be consumption of oxygen at the catalyst layer, which has to be replenished. This can be done in part by diffusion but necessarily also at least in part by the so-called Stefan flow [61–63] as described in 2.C. In such cases, the \bar{j}_w that we mention will actually be lower than the one calculated using Eq. (2.3). For simplicity and providing insights, we will, however, continue to use the value of \bar{j}_w given by Eq. (2.7).

Based on the work of Ref. [64], Refs. [65, 66] relate the permeability to the capillary pressure curve as $K = \alpha \epsilon^3 \int_0^1 \frac{(\sigma \cos \theta)^2}{p_c^2} ds$, where the material-dependent constant α is of order unity. With Eq. (2.4) this gives²

$$K = \frac{\alpha \epsilon^3}{4} \frac{\lambda}{\lambda + 2} r_{\max}^2. \quad (2.8)$$

This gives for $\bar{L} = r_{\max} L / K$

$$\bar{L} \equiv \frac{4(1 + 2/\lambda)}{\alpha \epsilon^3} \frac{L}{r_{\max}}. \quad (2.9)$$

so for a given porous material \bar{L} is a multiple of the characteristic maximum pore size r_{\max} .

2.2.2. BOUNDARY CONDITION

The relative permeability model of Eq. (2.2) assumes that there are continuous pathways for each phase. When applied to different porous media, the pressures across their interface are also assumed to be continuous. When bubbles or droplets are present at the flow channel-DL interface, they will typically be much larger than the maximum pore size so that their capillary pressure is much smaller than p_t . From Eq. (2.4), this implies that s remains close to its maximum, $s_0 \approx 1$.

As s_0 approaches unity, the interstitial velocity $u_n = U_n / \epsilon(1 - s_0)$ of the non-wetting phase starts to exert a non-negligible dynamic pressure $\frac{1}{2} \rho_n u_n^2$. With continuity of pressure we can approximately equate this to p_t to give with Eq. (2.3)

$$s_0 \approx 1 - \sqrt{\frac{\rho_n}{2p_t} \frac{z_n \mathcal{V}_n}{\epsilon F} j}. \quad (2.10)$$

Even for very large current densities of many A/cm² this usually negligibly deviates from $s_0 = 1$. Therefore, from now on, *we will use* $s_0 = 1$ as a boundary condition. Recent measurements found this indeed to hold true over a wide range of current densities in PEMWEs [25]. For PEMFCs something similar is found, although there the exact value of s_0 depends also on the relative humidity of the inlet gas and can be substantially different behind flow channel ribs [68]. Also the presence of a micro-porous layer can disturb the entire saturation profile s_0 [69].

Other authors have previously used a different constant value [49, 70] or semi-empirical formula [71] as a boundary condition for s_0 . In 2.B we treat the general case in which the capillary pressure of small droplets or bubbles cannot be neglected.

²Comparing with the Karman-Cozeny [67] result $K = \frac{d_p^2 \epsilon^3}{180(1-\epsilon)^2}$, for a porous medium consisting of spherical particles of diameter d_p , this gives $r_{\max} = \frac{d_p}{1-\epsilon} \sqrt{\frac{1+2/\lambda}{45\alpha}}$.

Note that we may modify Eq. (2.4) to $p_c = p_t (s^{-1/\lambda} - s_0^{-1/\lambda})$ without changing (2.6). In this case the maximum pore size disappears and for $s > s_0$ the capillary pressures becomes negative as in, for example, Ref. [72]. Such a capillary pressure curve may roughly approximate a hydrophobic medium in which the largest pores are coated with a hydrophilic layer, or vice versa. Equal gas and liquid pressures at the channel-DL interface give $s = s_0$ as a boundary condition, as was also used in Ref. [35]. Also, sometimes part of the saturation is considered immobile [73]. This fraction can, however, for most purposes be simply added to the solid volume fraction.

2.3. ANALYTICAL SOLUTIONS

2.3.1. ANALYTICAL SOLUTION FOR THE SATURATION

As discussed below Eq. 2.6, the wetting phase saturation s_1 at the DL-CL interface will be below that at the channel-DL interface, s_0 . An exact analytical solution to Eq. (2.6) is not possible, so we approximate the solution by dividing the domain into two parts where we neglect either the first or the second term on the right-hand side, respectively. We define the saturation s_* as the saturation for which both terms are equal, which is the case when

$$s_* = \frac{1}{1 + (J_w/J_n)^{1/3}}. \quad (2.11)$$

Here $J_w/J_n = \mu_n z_n \nu_n / \mu_w z_w \nu_w$ is a constant, independent of the current density j , that depends only on ratios of fluid properties and reaction stoichiometries.

For $s > s_*$ we neglect the second term on the right-hand side of Eq. 2.6, so that integrating gives

$$\bar{j}_n \bar{x} = I_n^\lambda \Big|_{s_0}^s \quad (s > s_*). \quad (2.12)$$

The integral $I_n^\lambda \equiv \int (1-s)^3 ds^{-1/\lambda} = -\frac{1}{\lambda} \int (1-s)^3 s^{-1-\frac{1}{\lambda}} ds$ can be performed analytically, giving

$$I_n^\lambda \Big|_0^s = s^{-\frac{1}{\lambda}} \left(1 + \frac{3s}{\lambda-1} - \frac{3s^2}{2\lambda-1} + \frac{s^3}{3\lambda-1} \right). \quad (2.13)$$

Solving Eq. 2.12 for s in terms of \bar{x} can only be done numerically. An approximation near $s \approx 1$ can however be obtained using the linearized capillary pressure shown in Fig. (2.2). Equation (2.6) with the second term neglected becomes

$$-\frac{1}{\lambda} \frac{ds}{d\bar{x}} = \frac{\bar{j}_n}{(1-s)^3} \quad (s \approx 1), \quad (2.14)$$

which is solved by $s \approx 1 - ((1-s_0)^4 + 4\lambda \bar{j}_n \bar{x})^{1/4}$, or with the boundary condition $s_0 = 1$ ³

$$s \approx 1 - (4\lambda \bar{j}_n \bar{x})^{1/4} \quad (s \gtrsim 0.6). \quad (2.15)$$

³Comparing with the numerical solution for large λ shows that this is accurate to a relative error in $1-s$ of at most 10 % when used for $s \gtrsim 0.6$. For lower values of $\lambda = 3, 2, 1$ rather only apply it for $s \gtrsim 0.65, 0.7, 0.75$, respectively.

This analytical solution is similar to that obtained in Ref. [74] for a Leverett-J function capillary pressure relation.

When $s = s_*$ at $x = x_*$, Eq. (2.12) gives

$$\bar{x}_* = \frac{I_n^\lambda|_{s_0}^{s_*}}{\bar{J}_n} \begin{matrix} s_* \gtrsim 0.6 \\ s_0 \approx 1 \end{matrix} \frac{(1 - s_*)^4}{4\lambda\bar{J}_n}. \quad (2.16)$$

where the final expression was obtained from Eq. (2.15).

For $\bar{x} \geq \bar{x}_*$ the saturation drops below s_* and we will neglect the first term on the right-hand side of Eq. (2.6), so that integrating Eq. (2.6) gives

$$\bar{J}_w(\bar{x} - \bar{x}_*) = I_w^\lambda \Big|_{s_*}^s \quad (s > s_*). \quad (2.17)$$

The wetting integral $I_w^\lambda \equiv \int s^3 ds^{-1/\lambda}$ evaluates to

$$I_w^\lambda \Big|_0^s = -\frac{s^{3-\frac{1}{\lambda}}}{3\lambda-1}, \quad (2.18)$$

so that Eq. (2.17) gives

$$s \approx \left[s_*^{3-\frac{1}{\lambda}} - (3\lambda-1)\bar{J}_w(\bar{x} - \bar{x}_*) \right]^{\frac{1}{3-1/\lambda}} \quad (s \leq s_*). \quad (2.19)$$

2.3.2. ANALYTICAL SOLUTION FOR THE MAXIMUM CURRENT

Various problems, like flooding in hydrogen fuel cells or membrane dehydration in water electrolyzers, are associated with a low saturation s_1 . We here consider the question what maximum current density is associated with a minimum saturation s_{\min} . The reasons for such a minimum saturation can be diverse, and may also depend on subjective criteria, an analysis of which is beyond the scope of this work.

When $s > s_*$, Eq. (2.12) immediately gives $j_{\max} = j_n I_n^\lambda|_{s_0}^{s_{\min}}$. Although useful and accurate when s_{\min} is well above s_* , an arguably more insightful result is obtained when additionally $s_{\min} \gtrsim 0.6$ so that we may use the final expression in Eq. (2.15) to write

$$j_{\max} \approx \frac{j_n}{\lambda} \frac{(1 - s_{\min})^4}{4} \quad (s_{\min} \geq s_*). \quad (2.20)$$

Inserting Eq. (2.7) and Eq. (2.8) shows more clearly the dependence on the various parameters

$$j_{\max} \approx J_n \frac{e^3}{\lambda+2} \frac{r_{\max}}{L} \frac{(1 - s_{\min})^4}{16}. \quad (2.21)$$

where $J_n = 2\sigma|\cos(\theta)|F/V_n\mu_n z_n$ contains the non-wetting phase fluid properties. In terms of the diffusion layer properties, clearly a sufficient porosity ϵ and a pore aspect ratio r_{\max}/L are beneficial for obtaining a high maximum current density while maintaining a sufficient saturation s_{\min} . The influence of the pore size distribution parameter is less strong and only shows a strong negative influence in case of very uniform pore size distributions with $\lambda \gg 1$.

When $s_{\min} < s_*$ we can solve Eq. (2.19) with $s = s_{\min}$ at $\bar{x} = 1$ for $\bar{j}_w = j/j_w$, to give

$$j_{\max} \approx \frac{j_w}{\lambda} \frac{s_*^{3-\frac{1}{\lambda}} - s_{\min}^{3-\frac{1}{\lambda}}}{(1-\bar{x}_*)(3-1/\lambda)} \quad (s_{\min} \leq s_*). \quad (2.22)$$

This is an implicit equation, since \bar{x}_* depends on current density. If $s_* \gtrsim 0.6$, or from Eq. (2.11) $j_w \lesssim 0.3j_n$, we can use the final expression in Eq. (2.16) to give⁴

$$j_{\max} \approx j_n \frac{(1-s_*)^4}{4\lambda} + j_w \frac{s_*^{3-\frac{1}{\lambda}} - s_{\min}^{3-\frac{1}{\lambda}}}{3\lambda-1} \quad (s_{\min} \leq s_*). \quad (2.23)$$

We note that there may just as well be a maximum s_{\max} to avoid, for example, membrane dehydration in case of a gas-fed fuel cell. In this case the above equations can be used for a minimum current density j_{\min} , by interchanging the subscripts max and min.

2.3.3. INTERPRETATION

With $s_0 \approx 1$ the diverging first term on the right-hand side of Eq. (2.6) causes a rapid drop in saturation near the channel-DL interface as described by Eq. (2.15) and illustrated in Fig. 2.1. In this regime, Eq. (2.20) determines the maximum current density associated with a minimum saturation s_{\min} . The interpretation of this result is relatively straightforward. From Eq. (2.4) we have a driving capillary pressure gradient $dp_c/dx \approx -(p_t/\lambda) ds/dx$ near $s = 1$. This shows how a wider pore size distribution, associated with a lower value of λ , gives a higher driving capillary pressure gradient allowing a higher maximum current density. With $k_w = 1$, Eq. (2.14) would be solved by $s \approx 1 - \lambda \bar{j}_n$ so that $j_{\max} = j_n \frac{1-s_{\min}}{\lambda}$. The wetting phase however strongly increases the friction through the relative permeability $(1-s)^3$, which introduces the 4 in both the power and denominator of Eq. (2.20).

For $s \leq s_*$ the second term on the right-hand side of Eq. (2.6) dominates. This term represents the friction of the wetting phase, which in this regime determines the maximum current density. The presence of the non-wetting phase through the relative permeability s^3 , in this case, introduces the $3 - 1/\lambda$ in Eq. (2.22). Once the wetting phase pressure gradient starts to dominate, the saturation has already decreased to s_* , but also the remaining distance $L - x_*$ to the catalyst layer, over which the capillary pressure gradient acts, has decreased, explaining the appearance of these terms in Eq. (2.22).

Finally, Eq. (2.23) combines the results of Eqs. (2.20) and Eq. (2.22). This may be interpreted in analogy with a series circuit of ‘resistances’ proportional to $1/j_n$ and $1/j_w$, but also depending non-linearly on the ‘potential’ s .

We note that, while in accordance with the discussion in section 2.2.2 we assumed a boundary condition $s_0 = 1$, it is straightforward to generalize the above equations to an arbitrary value of s_0 . We note that when $s_0 \leq s_*$, we can use Eq. (2.19) with $s_* = s_0$ and $\bar{x}_* = 0$.

With a gaseous reactant and liquid product, usually $j_w/j_n = \frac{\mu_n z_n V_n}{\mu_w z_w V_w} \ll 1$ so that, from Eq. (2.11), $s_* \gtrsim 0.6$ and Eqs. (2.15), (2.20), and (2.23) can be used. Note that in this case, usually, the first term in Eq. (2.23) can be neglected.

⁴For a general s_0 , $(1-s_*)^4$ is replaced by $(1-s_*)^4 - (1-s_0)^4$.

Given the right integral I_n^λ , Eq. (2.12) can be used for any type of capillary pressure relation. Different relative permeability models can be accommodated after suitably redefining s_* . In 2.G we work out the integral I_n^λ for the Leverett-J function.

2.4. PERFORMANCE LOSSES IN A DIFFUSION LAYER

2.4.1. ACTIVATION OVERPOTENTIALS η

A limiting current density arises when reactants cannot diffuse to the catalyst layer at a sufficient rate. We assume that the concentration-dependent Tafel equation describes the half-reaction in the catalyst layer as:

$$j = \chi j_\star \left(\frac{c_1}{c_0} \right)^r \exp\left\{ \frac{\eta}{b} \right\}, \quad (2.24)$$

where r is the order of the reaction in the reactant concentration c_1 , assumed constant throughout the thin catalyst layer, χ is the fraction of total surface area covered by the wetting phase reactant, j_\star is the superficial exchange current density of the catalyst layer [75] at the bulk concentration c_0 at $\bar{x} = 0$, and the Tafel slope $b = RT/\alpha F$ [76], where $\alpha \lesssim 1$ is the charge transfer coefficient. Rearranging Eq. (2.24), we can split the activation overpotential η into three separate terms

$$\eta = \overbrace{b \ln \frac{j}{j_\star}}^{\eta_a} + \overbrace{b \ln \frac{1}{\chi}}^{\eta_\chi} + \overbrace{r b \ln \frac{c_0}{c_1}}^{\eta_c}. \quad (2.25)$$

Here η_a is the overpotential required when the entire reactive area is wetted with reactant at the concentration c_0 . In Eq. (2.25) η_χ is the additional overpotential due to the non-wetting phase covering a fraction χ of the reactive area, and η_c is the concentration overpotential.

We note here that an often considered voltage loss that is not mentioned in Eq. (2.25) is the change in equilibrium potential due to the dissolved gases [22, 23, 27, 33, 71, 77, 78]. If the associated reaction steps are not rate-determining, they may be considered in equilibrium and described by the Nernst equation

$$\Delta E_{\text{mt}} = \frac{RTz_n}{F} \ln \frac{C}{C_{\text{ref}}}, \quad (2.26)$$

with C the concentration of the dissolved product gases at the position of the catalyst layer, and C_{ref} a reference value. See, for example, Ref. [27] for a simple model to estimate C .

2.4.2. WETTING OVERPOTENTIAL η_χ

The surface coverage can be calculated using $\chi = \bar{s}^{\frac{\bar{\lambda}-1}{\bar{\lambda}}}$ from 2.F, so that

$$\eta_\chi = (1/\bar{\lambda} - 1) b \ln \bar{s}. \quad (2.27)$$

Variables dressed with a *tilde* denote the properties of the catalyst layer. As the catalyst layer pore size distribution parameter $\tilde{\lambda} \rightarrow 1$ Eq. (2.27) gives that $\eta_\chi \rightarrow 0$ and the surface coverage does not adversely impact performance. The reason is that the smallest pores, that have most of the surface area, remain available for the reaction. If $\tilde{\lambda} \gg 1$, Eq. (2.27) reduces to $\eta_\chi = -b \ln \tilde{s}$, which is used, for example, in Refs. [70, 71]. In liquid-phase electrolyzers this is often referred to as the bubble overpotential [23].

For a very thin catalyst layer formed by spraying small particles on the diffusion layer, we may use $\tilde{s} = s_1$. For a more extended layer, with potentially a wettability different from that of the diffusion layer, we may assume continuity of the capillary pressure [79, 80] which, from Eq. (2.4), gives $\tilde{s} = (p_t s_1^{-1/\lambda} / \tilde{p}_t)^{-\tilde{\lambda}}$. Both of these models are, however, obviously simplifications that have to be used with caution. The latter formula for example, may give rise to $\tilde{s} > 1$ in case of very small catalyst layer pores, something that may be ameliorated by including dynamic pressures as in 2.A. Often there will be a mixed wettability in the catalyst layer, influencing the relation between s_1 and \tilde{s} .

2.4.3. CONCENTRATION OVERPOTENTIAL η_c

In water electrolyzers, water is always present in high concentrations ($c_1 \approx c_0$) and any transport losses occur mainly due to the surface area of the catalyst layer getting covered by gas. For applications such as hydrogen fuel cells or CO₂-reduction-GDEs, reactant gases have to diffuse through either a mixture of gases or through water to reach the catalyst surface [81]. In the dilute limit, c_1 can then be obtained from Fick's law [82, 83] for the molar flux

$$\frac{z_w}{F} j = D_{\text{eff}} \frac{c_0 - c_1}{L}, \quad (2.28)$$

where D_{eff} is the effective diffusion coefficient, modified by the saturation profile. A limiting current is obtained when $c_1 \rightarrow 0$, which gives

$$j_{\text{lim}} = \frac{F D_{\text{eff}} c_0}{z_w L}. \quad (2.29)$$

In the absence of the non-wetting phase we have a limiting current density

$$j_{\text{lim}0} = \frac{F D c_0}{z_w L}, \quad (2.30)$$

where $D = D_0 \epsilon / \tau$ in terms of the porosity ϵ and tortuosity τ , and the single phase diffusivity D_0 . Often a power law relation $\tau = \epsilon^{1-m}$ approximately holds so that $D = D_0 \epsilon^m$. It has been pointed out that $m = 1.5$ as in Bruggeman's correlation underestimates the effect of tortuosity in diffusion layers and often a value between 2 and 5 is more appropriate [84, 85].

Inserting c_1 from Eq. (2.28) in η_c from Eq. (2.25) gives the concentration overpotential as

$$\eta_c = r b \ln \left(\frac{1}{1 - j / j_{\text{lim}}} \right). \quad (2.31)$$

2.4.4. EFFECTIVE DIFFUSIVITY D_{EFF}

Since the diffusivity of gases in liquids is several orders of magnitude lower than that in gases, we neglect the transport of gases in the liquid phase. This implies that the transport of reactant gas in the presence of liquids will be slower than in a dry GDL, leading to a lower limiting current. In the presence of liquid non-wetting phase, the effective diffusivity of the gaseous wetting phase is reduced, as described by Eq. (2.79):

$$\frac{D}{D_{\text{eff}}} = \int_0^1 s^{-n} d\bar{x}. \quad (2.32)$$

In general, the exponent n can differ from the exponent m , but is also typically in the range between 2 and 5 [84, 85]. Equation (2.32) shows that the effective diffusivity tends to zero as the saturation of the non-wetting gaseous phase, s approaches 1. However, in such cases, we will have small molecular diffusion through the liquid which is neglected in Eq. (2.32). To approximate this integral we use the same approach as in section 2.3.1 and split the integral in two parts. Between $\bar{x} = 0$ and \bar{x}_* we neglect the final term in

Eq. (2.6) so that we can make a change of variables and write $\int_0^{s_*} s^{-n} d\bar{x} = \frac{\lambda_n}{\lambda} \frac{I_n^{\lambda_n}|_{s_0}^{s_1}}{\bar{j}_n}$, as shown in Eq. (2.83). Here $\lambda_n = \frac{\lambda}{1+\lambda n}$ or

$$\frac{1}{\lambda_n} = \frac{1}{\lambda} + n. \quad (2.33)$$

We hope that no confusion arises because of our use of a subscript n here, not referring to the non-wetting phase but instead to the exponent n in Eq. (2.32). Beyond \bar{x}_* we neglect again the first term in Eq. (2.6) resulting in

$$\frac{D}{D_{\text{eff}}} \approx \begin{cases} \frac{\lambda_n}{\lambda} \frac{I_n^{\lambda_n}|_{s_0}^{s_1}}{\bar{j}_n} & s_1 > s_* \\ \frac{\lambda_n}{\lambda} \left(\frac{I_n^{\lambda_n}|_{s_0}^{s_*}}{\bar{j}_n} + \frac{I_w^{\lambda_n}|_{s_*}^{s_1}}{\bar{j}_w} \right) & s_1 \leq s_*. \end{cases} \quad (2.34)$$

The quantity in Eq. (2.34), inversely proportional to the effective diffusivity, is a dimensionless mass transfer resistance and has the structure of two resistances in series.⁵

2.4.5. DIFFUSION LIMITED CURRENT DENSITY j_{LIM}

First we consider the case in which $s_1 \geq s_* \gtrsim 0.6$ so that with $s_0 \approx 1$, Eq. (2.15) can be used. In this case we can derive the Eq. (2.81), or with $4(4/5)^4 \approx 1.6$

$$\frac{D}{D_{\text{eff}}} \approx \left(1 - \left(1.6\lambda \frac{j}{j_n} \right)^{1/4} \right)^{-n}. \quad (2.35)$$

From Eq. (2.15) this remains valid up to $1.6\lambda \frac{j}{j_n} \approx 0.01$ in which case the diffusivity is reduced by a factor 0.68^n . This exponential dependence on n highlights the importance

⁵Note that for $\lambda = \lambda_n$, using Eqs. (2.16) and Eq. (2.17), the first and last term between brackets of Eq. (2.34) become \bar{x}_* and $1 - \bar{x}_*$ so that $D_{\text{eff}} = D$ as it should for $n = 0$.

of straight non-tortuous gas pathways, potentially using techniques as in Ref. [86], that lower n . Inserting into Eq. (2.29) gives

$$j_{\text{lim}} \approx j_{\text{lim}0} \left(1 - \left(1.6\lambda \frac{j_{\text{lim}}}{j_n} \right)^{1/4} \right)^m. \quad (2.36)$$

Comparing with the numerical solution for $\lambda \geq 1$ shows that this approximation has a relative error below 10 % when $j_{\text{lim}} \lesssim j_n \frac{0.003}{n+\lambda}$. In general, this implicit equation has to be solved numerically. When, however, $n = 4$ we find

$$j_{\text{lim}} \approx \left(j_{\text{lim}0}^{-1/4} + \left(\frac{j_n}{1.6\lambda} \right)^{-1/4} \right)^{-4}. \quad (2.37)$$

Note that j_{lim} will always be lower than the smallest of $j_{\text{lim}0}$ and $j_n/1.6\lambda$. This makes sense, as the presence of the non-wetting phase can only lower the effective diffusivity and therewith the diffusional limiting current. We previously found that the maximum current that can be maintained by capillary action, considering only the friction of the non-wetting phase, is proportional to j_n/λ , see e.g. Eq. (2.20).

Next, we consider the case in which $s_1 < s_*$ for which the bottom result of Eq. (2.34) has to be used. Inserting into Eq. (2.29) gives an implicit equation

$$I_n^{\lambda n} \Big|_{s_0}^{s_*} j_n + I_w^{\lambda n} \Big|_{s_*}^{s_1} j_w \approx j_{\text{lim}0} (1 + \lambda n). \quad (2.38)$$

When the first term can be neglected⁶ this gives, after some algebra

$$j_{\text{lim}} \approx j_w s_*^{3-\frac{1}{\lambda}} \frac{1 - \left(1 + \frac{j_{\text{lim}0}}{j_w} \frac{1-\lambda(3-n)}{s_*^{3-1/\lambda n}} \right)^{\frac{3-1/\lambda}{3-1/\lambda n}}}{(3\lambda - 1)(1 - \bar{x}_*)} \quad (2.39)$$

where s_* and x_* are given by Eqs. (2.11) and Eq. (2.11), respectively. Eq. (2.39) simplifies in the following two limits

$$j_{\text{lim}} \approx \begin{cases} \frac{j_w s_*^{3-\frac{1}{\lambda}}}{1-\bar{x}_*} \frac{1}{3\lambda-1} & \frac{j_{\text{lim}0}}{j_w s_*^{3-1/\lambda n}} \gg 1 \\ \frac{j_{\text{lim}0} s_*^m}{1-\bar{x}_*} & \frac{j_{\text{lim}0}}{j_w s_*^{3-1/\lambda n}} \ll 1. \end{cases} \quad (2.40)$$

The top equation is exactly Eq. (2.23) for $s_{\text{min}} = 0$, which makes sense since when the saturation s_1 vanishes, the effective diffusivity vanishes as well, causing a limiting current. If $s_* \gtrsim 0.6$ we can use Eq. (2.16), similar to in Eq. (2.23), to give for the bottom case of Eq. (2.40)

$$j_{\text{lim}} \approx j_{\text{lim}0} s_*^n + j_n \frac{(1-s_*)^4}{4\lambda}. \quad (2.41)$$

⁶When $s_* \gtrsim 0.6$ we can use Eqs. (2.16), Eq. (2.18), Eq. (2.11) to write $\frac{1-s_*}{4\lambda n} \ll \frac{s_*^{3-\frac{1}{\lambda n}} - s_1^{3-\frac{1}{\lambda n}}}{s_*^3(3\lambda n - 1)}$. This is usually the case when s_1 drops somewhat below s_* , or from Eq. (2.16) when $j \gtrsim j_n \frac{(1-s_*)^4}{4\lambda}$.

Here $j_{\text{lim}0}$ is reduced by a factor s_*^n due to the lower saturation s_* , which in this limit does not drop much further. The final term in Eq. (2.41) adds a bit for the initial part where $s > s_*$.

2.5. RESULTS AND DISCUSSIONS

For the hydrophobic SGL carbon paper, Toray090, E-Tek Cloth “A” and Lyflex felts, λ lies between 0.95-4 and p_t varies between 6-39 kPa [87]. These hydrophobic diffusion layers are typically a few hundred micrometres thick [87, 88]. Water electrolyzers usually have titanium-based hydrophilic layers with the largest pore diameter roughly 12-16 μm , the permeability of the order 10^{-12} m^2 , and a thickness around 1 mm [89] corresponding to a threshold pressure p_t of the order of 10 kPa. For illustration, we choose the diffusion layer parameters for both electrolyzers and fuel cells to be same as that of Toray090 [87] for which $\lambda \approx 4$ and $p_t = 10 \text{ kPa}$. Table 2.1 lists the properties for exemplary gaseous and liquid wetting phase cases, representative of a typical PEM fuel cell and water electrolyzer, respectively.

Table 2.1: Characteristics and operating conditions for example diffusion layers at 1.2 bar and 60°C. The common structural parameters used are $K = 8 \cdot 10^{-12} \text{ m}^2$, $p_t = 10 \text{ kPa}$, $r_{\text{max}} = 10 \mu\text{m}$, $2\sigma|\cos\theta| = 0.1 \text{ N/m}$, $\lambda = 4$, $m = n = 3$, and $\epsilon = 0.78$ [87]. A diffusivity $D_{O_2} = 2 \cdot 10^{-5} \text{ m}^2/\text{s}$ for oxygen in air gives $j_{\text{lim}0} = 11 \text{ A/cm}^2$. Note that for μ_n and ν_n property we used the wetting phase properties of the adjacent column.

Wetting phase	Gaseous	Liquid
Examples	PEMFC, AEMFC, CO ₂ -GDE	PEMWE, AEMWE, Di- rect alcohol fuel cells
L [μm]	300 [87]	1000 [89]
$\bar{L} = r_{\text{max}}L/K$	375	1250
μ_w [Pa-s]	$2.2 \cdot 10^{-5}$	$4.7 \cdot 10^{-4}$
ν_w [m^3/mol]	$23 \cdot 10^{-3}$	$1.8 \cdot 10^{-5}$
$1/z_w$	4	2
$1/z_n$	2	4
s_*	0.75	0.25
J_w/J_n	0.03	30
J_w [A/m^2]	$7.6 \cdot 10^{10}$	$2.3 \cdot 10^{12}$
J_n [A/m^2]	$2.3 \cdot 10^{12}$	$7.6 \cdot 10^{10}$
j_w [A/m^2]	$2 \cdot 10^8$	$1.8 \cdot 10^9$
j_n [A/m^2]	$6.1 \cdot 10^9$	$6.1 \cdot 10^7$
j [A/m^2]	$2 \cdot 10^4$	$2 \cdot 10^4$

2.5.1. VERIFICATION OF THE ANALYTICAL MODEL

Figure 2.3(a) shows a comparison between analytical and numerical saturation profiles for the two cases listed in Table 2.1. The analytical solution for the wetting phase saturation is always higher than the numerical solution. This is expected, because we always

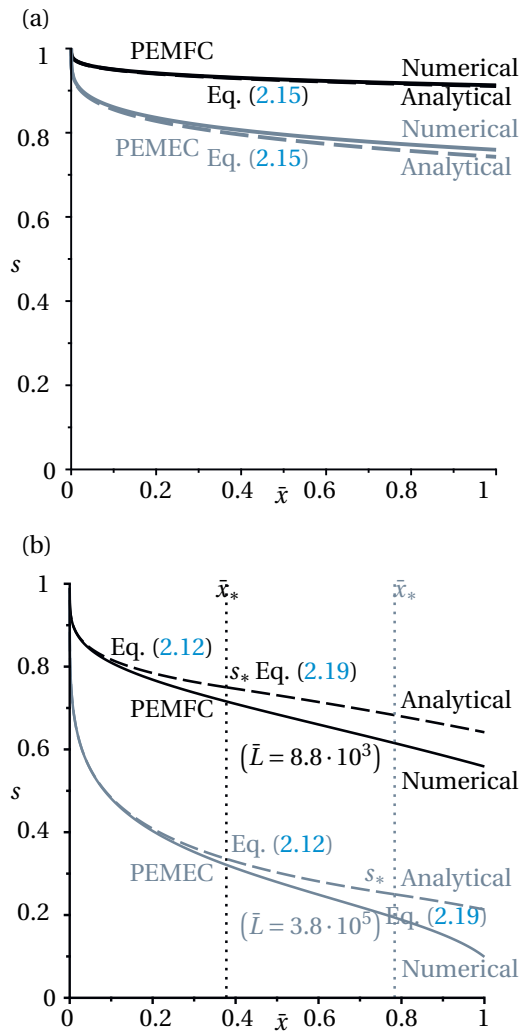


Figure 2.3: A comparison between the analytical and numerical wetting phase saturation s across the diffusion layer for $j = 2 \text{ A/cm}^2$ and the typical diffusion layer properties listed in Table 2.1 (a). For the bottom figure (b) we used a much higher $\bar{L} = 8.8 \cdot 10^3$ and $3.8 \cdot 10^5$ for the PEMFC and PEMWE case respectively to show the effect of, for example, a much smaller pore size. For $\bar{x} < \bar{x}_*$, the non-wetting phase dominates and Eq. (2.12) is used for analytical solution while for $\bar{x} > \bar{x}_*$, the wetting phase dominates and Eq. (2.19) is used.

neglect one of the terms on the right-hand side of Eq. (2.6) and hence underestimate the capillary pressure gradient. The agreement with Eq. (2.15) is nonetheless good since s remains rather high.

In Fig. 2.3(b) we also show a case where we increased \bar{L} to show the effect of, for example, a much smaller pore size. In this case in part of the diffusion layer the wetting phase pressure gradient dominates, represented by the final term in Eq. (2.6). In this case we used the analytical result of Eq. (2.19) for which the agreement with the numerical

result is reasonable.

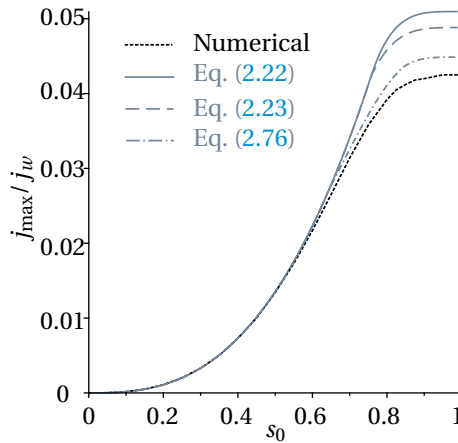


Figure 2.4: The maximum current for which $s_1 = s_{\min} = 0$ as a function of s_0 for the *gaseous* wetting phase properties given in Table 2.1. The solid black line indicates the numerical result obtained by solving Eq. (2.6), the solid gray line indicates the two-regime analytical solution described in section 2.3.2 and the dashed gray line indicates the three-regime analytical solution described in 2.H. In this model we also consider a third domain where the saturation profile is assumed to be linear, and contributions from both \bar{j}_n and \bar{j}_w are important.

2.5.2. MAXIMUM CURRENT DENSITY

For the properties listed in Table 2.1, to reach $s_{\min} = 0$, according to Eq. (2.22) requires a current density $j_{\max} \approx 10^7$ A/m² for both layers. This extremely high current density shows that for the typical diffusion layer properties of Table 2.1 there will be no risk of approaching $s_{\min} = 0$.

Although the boundary condition $s_0 \approx 1$ was argued to be the relevant boundary condition for most cases, in Fig. 2.4 we show the effect of s_0 on the limiting currents. This can be useful for mixed-wettability layers and because different boundary conditions are sometimes used [35, 70, 71]. Figure 2.4 shows that the limiting current j_{\max} is insensitive to the exact boundary condition when s_0 is close to 1. The reason is the large drop in s that occurs in a very thin layer near $\bar{x} = 0$ seen in Fig. (2.3). This strong decrease is caused by the first term on the right-hand side of Eq. (2.6) and described by the formula given just above Eq. (2.15).

2.5.3. LIMITING CURRENT DENSITY

Air with 21 v% of oxygen at 1.2 bar and 60° has an oxygen concentration of $c_0 = 9.1$ mol/m³⁷, so that with $D_{O_2} = 2 \cdot 10^{-5}$ m²/s, $n = 3$, and the gaseous wetting phase properties in Table 2.1, we find a single phase diffusion-limited current density of $j_{\lim 0} = FDc_0/z_wL \approx 11$ A/cm². Since this is below $0.01j_w/4\lambda$ we can use Eq. (2.35) to calculate D_{eff} . Solving Eq. (2.29) for $j = j_{\lim}$ iteratively gives $j_{\lim} \approx 8.1$ A/cm². The presence of wa-

⁷From 2.C, a better approximation would be to use $\ln \frac{1}{1-0.21} \approx 0.24$ times the molar volume, but in line with present dilute approximation we use 0.21, instead.

ter in this case actually only moderately decreases the limiting current density, which is expected giving the high saturation throughout the diffusion layer, shown in Fig. 2.3(a).

Using the explicit Eq. (2.37) gives $j_{\text{lim}} \approx 7.3 \text{ A/cm}^2$, which is slightly lower than the numerical value because it was derived for a higher value $n = 4$.

2.5.4. MASS TRANSPORT LOSSES

The limiting current densities calculated in section 2.5.3 are well above typical desirable current densities so that the associated concentration overpotentials will be small. With $j = 2 \text{ A/cm}^2$, for example, Eq. (2.31) gives $\eta_c/b = 0.28$ amounting to at most a few tens of millivolts. It has been pointed out previously that modern diffusion layers do not contribute significantly to transport limitations [81].

For a water electrolyzer concentration overpotentials are negligible, but the lowered saturation at the catalyst layer can incur a wetting or bubble overpotential η_χ according to Eq. (2.27). With $\tilde{\lambda} = 4$ and $\bar{s} = s_1 = 0.75$ from Fig. 2.3 this gives $\eta_\chi/b \approx 0.21$.

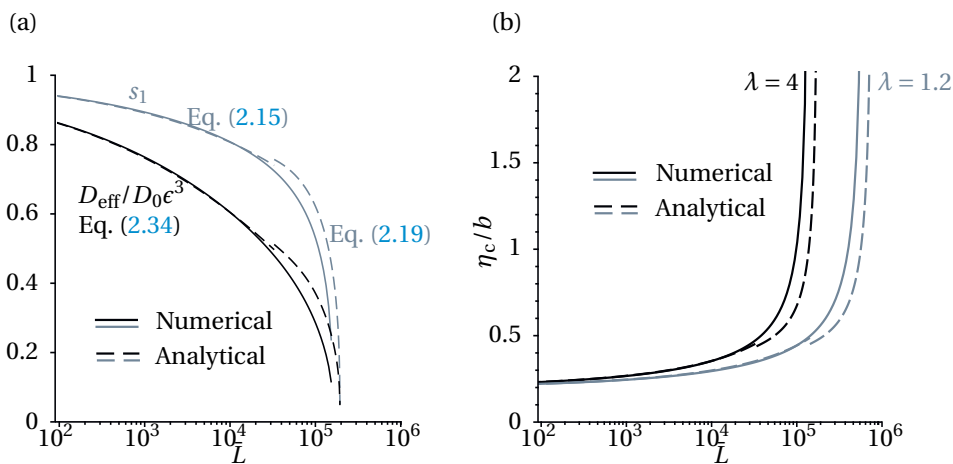


Figure 2.5: (a) The effective diffusivity D_{eff} (black) and the saturation s_1 (grey) at the DL-CL interface as a function of $\bar{L} = r_{\text{max}}L/K$ at a current density of 2 A/cm^2 for the gaseous wetting phase properties listed in Table 2.1. A discontinuity appears because the approximation Eq. (2.15) is used only for high s . (b) The associated concentration overpotentials, calculated using Eq. (2.25). The diffusion coefficient is taken to be equal to $D_{O_2} = 2 \cdot 10^{-5} \text{ m}^2/\text{s}$.

2.5.5. DESIGN LIMITATIONS ON \bar{L}

Figure 2.5 shows the saturation s_1 at the DL-CL interface and the effective diffusivity D_{eff} as well as the associated concentration overpotential as a function of the dimensionless diffusion layer thickness \bar{L} . For not too low $s \gtrsim 0.6$, we can use Eq. (2.37) to calculate explicitly what the maximum dimensionless layer thickness $\bar{L} = Lr_{\text{max}}/K$ is to reach a

desired limiting current density j_{lim} ⁸

$$\bar{L} \approx \frac{J_n}{1.6\lambda} (j_{\text{lim}}^{-1/4} - j_{\text{lim}0}^{-1/4})^4. \quad (2.42)$$

With the values from Table 2.1, this gives $\bar{L} \approx 2 \cdot 10^5$ for $\lambda = 4$ and $\bar{L} \approx 7 \cdot 10^5$ for $\lambda = 1.2$. Despite the different value $m = 4$ used to derive Eq. (2.42) this is in reasonable agreement with the results of Fig. 2.5.

The value of $\bar{L} \approx 2 \cdot 10^5$ for $\lambda = 4$ corresponds to a very small maximum pore size of $r_{\text{max}} \approx 0.02 \mu\text{m}$ for the same thickness, L and is actually not much smaller than the pores of $r_{\text{max}} \approx 0.1 \mu\text{m}$ typically used in a microporous layer [73, 90, 91]. These microporous layers are, however, typically much thinner than the diffusion layers so that their contribution to the mass transport resistance remains limited.

Even for $j_{\text{lim}} = 6 \text{ A/cm}^2$ the value $\bar{L} = 2 \cdot 10^4$ is well above the 375 in Table 2.1. This shows that even with substantially smaller pores the liquid saturation does not decreasing the limiting current density to values in the typically desired operating window. Therefore, the diffusion layer designs are often influenced by other considerations such as electrical resistance and mechanical strength [92].

When $s_* \gtrsim 0.6$, usually the case for gaseous reactants, we can use Eqs. (2.23) and (2.20) to find the value of \bar{L} that corresponds to a desired s_1 :

$$\bar{L} \approx \begin{cases} \frac{J_n}{j_{\text{max}}} \frac{(1-s_1)^4}{4\lambda} & s_1 \geq s_* \\ \frac{J_n}{j_{\text{max}}} \frac{(1-s_*)^4}{4\lambda} + \frac{J_w}{j_{\text{max}}} \frac{s_*^{3-\frac{1}{\lambda}} - s_1^{3-\frac{1}{\lambda}}}{3\lambda-1} & s_1 < s_*. \end{cases} \quad (2.43)$$

Using Eq. 2.9 in the top result gives

$$\frac{(2+\lambda)L}{\alpha \epsilon^3 r_{\text{max}}} \approx \frac{J_n}{j} \left(\frac{1-s_1}{2} \right)^4, \quad s_1 \geq s_* \quad (2.44)$$

where $r_{\text{max}} = 2\sigma |\cos(\theta)| / p_t$ and $J_n = 2\sigma |\cos(\theta)| F / V_n \mu_n z_n$ from Eqs. (2.5) and (2.7). Eq. (2.44) shows the various geometrical diffusion layer parameters on the left, and operational and material parameters on the right.

This shows that, for example, for the same s_1 at a two times higher current density would require, equivalently, halving the DL thickness L , doubling r_{max} or increasing ϵ by a factor $2^{1/3} \approx 1.26$.

2.6. CONCLUSIONS

We thoroughly studied the multiphase flow in porous diffusion layers, providing a general unified framework, valid for both fuel cells and electrolyzer as long as gas and liquid move in opposite directions. The obtained expressions can be readily used to provide guidance on choosing for example the layer thickness and pore size distribution.

⁸With Eq. (2.30) we can also solve Eq. (2.42) explicitly for L , to give $L \approx \frac{\frac{J_n K}{1.6\lambda j_{\text{lim}} r_{\text{max}}}}{\left(1 + \left(\frac{J_n K}{1.6\lambda j_{\text{lim}} r_{\text{max}}} \frac{z_w}{FD \epsilon_0}\right)^{1/4}\right)^4}$

We derived accurate semi-analytical expressions for saturation profiles, Eqs. (2.19) and Eq. (2.15). These were used in Eqs. (2.20)-(2.23) to calculate the maximum current density for which the saturation at the diffusion layer-catalyst layer interface becomes critically low. Equations (2.37)- (2.41) give useful expressions for the diffusion-limited current density.

These results show that for modern gas diffusion layers the wetting phase saturation usually remains above 0.8 so that performance is only modestly impacted and that they are well-designed for their intended operating conditions.

APPENDICES

2.A. BOUNDARY CONDITION FOR s_1

Here we consider what happens when the porosity or wetting properties suddenly change. This is relevant, for example, at the interface between the diffusion layer and microporous layer or catalyst layer, but also at the interface between the diffusion layer and the channel. Neglecting friction over the interface we can use Bernoulli's equation to equate the total pressure $p_i + \frac{1}{2}\rho_i u_i^2$ on either side of the interface. Using a + and - to denote properties right (slightly larger x) and left (lower x) of the interface this gives with $p_c = p_n - p_w$:

$$\begin{aligned} p_{c-} + \frac{1}{2}(\rho_{n-} u_{n-}^2 - \rho_{w-} u_{w-}^2) \\ = p_{c+} + \frac{1}{2}(\rho_{n+} u_{n+}^2 - \rho_{w+} u_{w+}^2) \end{aligned} \quad (2.45)$$

Usually dynamic pressures $\frac{1}{2}\rho_i u_i^2$ are negligible, resulting in the frequently used continuity of capillary pressure $p_{c-} = p_{c+}$ [79, 80]. With an explicit capillary pressure-saturation relation this can then be used to relate the saturations on either side of the interface. Using e.g. Eq. (2.4) gives $p_{t-} s_-^{-1/\lambda_-} = p_{t+} s_+^{-1/\lambda_+}$, or

$$s_+ = \left(\frac{p_{t+}}{p_{t-}}\right)^{\lambda_+} s_-^{\lambda_+/\lambda_-} \quad (2.46)$$

If the threshold pressure of the right medium is much larger than that of the left, as may be the case for a diffusion layer - microporous layer interface this equation may give $s_+ > 1$ so that the dynamic pressure of the non-wetting phase has to be included to give, assuming $\rho_{n+} = \rho_{n-} = \rho_n$

$$\frac{1}{2}\rho_n (u_{n-}^2 - u_{n+}^2) = p_{c+} - p_{c-} \quad (2.47)$$

The average interstitial velocity $u_n = U_n/\epsilon(1-s)$ where, from Eq. (2.3) we have $U_n^2 = (z_n \mathcal{V}_n j/F)^2$. With an capillary pressure-saturation relation like (2.4) this gives an explicit relation between s_+ and s_- that has to be solved numerically in general. There are obviously several assumptions in this analysis that require further investigation and validation, which is beyond the scope of this work.

2.B. BOUNDARY CONDITION FOR s_0

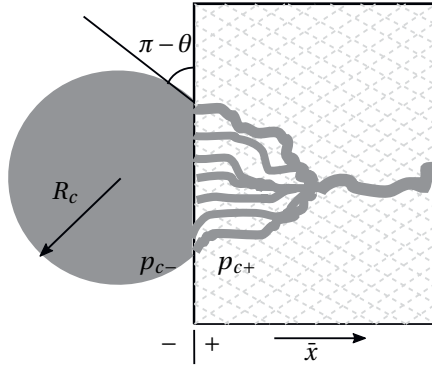


Figure 2.6: Schematic of a potential transition region near a droplet (or bubble, in which case $\pi - \theta$ becomes θ) the flow channel, we assume any deviation from one-dimensionality to be negligible. The '-' and '+' are denoted in the figure. The contact angle is denoted as θ and the radius of curvature of bubble/droplet is denoted as R_c .

Near $x = 0$, the presence of bubbles or droplets on the diffusion layer surface may cause the saturation to show variations also in the normal directions as schematically indicated in Fig. 2.6 similar to what was postulated for near the catalyst layer in Ref. [73]. Likely this disturbance from one-dimensional profiles is of the order of the droplets or bubble. Here we will assume the transition zone to be negligibly thin compared to the diffusion layer thickness. The capillary pressure of the droplets or bubbles will be

$$p_{c-} \approx \frac{2\sigma |\cos(\theta)|}{R_c} = p_t \frac{r_{\max}}{R_c} \quad (2.48)$$

where R_c is the radius of curvature of the bubble or droplet. Here we assumed that the contact angle is the same as inside the porous medium. Correcting for an effective contact angle will be possible using the Cassie-Baxter equation [93, 94].

Usually $R_c \gg r_{\max}$ so that the capillary pressure of the droplets or bubbles is negligible compared to that inside the porous medium. With $p_{c+} = p_t s_0^{-1/\lambda}$ this implies that s_0 will be close to unity. Neglecting therefore the dynamic pressure of the wetting-phase, we can use Eq. (2.47) to write

$$\frac{\rho_n U_n^2}{2p_t} \left(\frac{1}{\Theta^2} - \frac{1}{\epsilon^2 (1-s_0)^2} \right)^2 = s_0^{-1/\lambda} - \frac{r_{\max}}{R_c} \quad (2.49)$$

where Θ is the fractional bubble coverage, for which correlations exist in terms of j [95]. This implicit relation for s_0 can be re-written to

$$s_0 \approx 1 - \frac{1}{\epsilon \sqrt{\frac{1}{\Theta^2} - \sqrt{\frac{2p_t}{\rho_n U_n^2} \left(s_0^{-1/\lambda} - \frac{r_{\max}}{R_c} \right)}}} \quad (2.50)$$

where $U_n^2 = (z_n \nu_n j / F)^2$. In the circumstances where dynamic pressures dominate over capillary pressures, this gives for the saturation of the wetting phase $1 - s_0 \approx \Theta / \epsilon$, which represents the fraction of the pores covered with the non-wetting phase. In the more common case of dominant capillary pressure, this gives that s_0 is close to unity. With $r_{\max} \ll R_c$ Eq. (2.10) results.

2.C. STEFAN VELOCITY

In the model of section 2.2 we assume purely convective transport of reactants. However, if the reactant forms only a small fraction of the total wetting phase it will be transported primarily by diffusion, as assumed in sections 2.4.3-2.4.5. Here we consider the general case in which transport consists of both diffusion and advection, a problem referred to as Stefan flow.

Consider the case of a reacting species with concentration c and a nonreacting species with concentration c_N . They may, for example, correspond to oxygen and nitrogen in an air mixture at the cathode of a fuel cell. We assume that the total concentration

$$C = c_N + c \quad (2.51)$$

is a constant, which is a good approximation for gases. The flux of non-reacting species $uc_N - Ddc_N/dx = 0$, with D the mutual diffusion coefficient. Or, with Eq. (2.51):

$$0 = u(C - c) + D \frac{dc}{dx}. \quad (2.52)$$

With boundary conditions $c_0 = fC$ at the flow channel at $x = 0$ and $c_1 = 0$ at the CL at $x = L$, the differential equation (2.52) can be solved for the Stefan velocity u as

$$u = \frac{D}{L} \ln \frac{1}{1-f}. \quad (2.53)$$

Using Eq. (2.52), the reacting species flux is $N = uc - Ddc/dx = uC$ so that the velocity reads $u = N/C = fN/c_0$. We thus see that in Eq. (2.3) the molar volume is that of the total mixture. In the dilute limit $f \ll 1$ we have $\ln \frac{1}{1-f} \approx f$ so that from Eq. (2.53) Fick's law $N = uC = \frac{Dc_0}{L}$ is obtained.

2.D. EFFECT OF POWER q IN RELATIVE PERMEABILITY AND SATURATION RELATIONSHIP

Using a power law, we write the relative permeabilities as

$$k_w = s^q \text{ and } k_n = (1-s)^q \quad (2.54)$$

Values of q between 2 and 8 have been reported in recent literature [30]. In the main text, we used $q = 3$, which is actually inconsistent with the use of the Brooks-Corey power law capillary pressure model for which it can be derived that

$$k_w = s^{3+2/\lambda} \text{ and } k_n = (1-s)^2 \left(1 - s^{1+\frac{2}{\lambda}}\right) \quad (2.55)$$

See e.g. Ref. [65]. Only in the limit $\lambda \gg 1$ do these reduce to Eq. (2.54) with $q = 3$. The added complexity, in particular of the expression for k_n in Eq. (2.55), does not weigh up to the potential improvement in accuracy.

For general q and s_0 , Eq. (2.15) is easily generalized to

$$s \approx 1 - \left((1 - s_0)^{q+1} + (q+1) \lambda \bar{j}_n \bar{x} \right)^{\frac{1}{q+1}} \quad (2.56)$$

Note that for the Brooks-Corey relative permeability k_n of Eq. (2.55) actually a somewhat higher accuracy can be obtained Eq. (2.56) using a value for q slightly lower than 3. A suitable value can be found by solving $(1 - s)^2 \left(1 - s^{1 + \frac{2}{\lambda}} \right) = (1 - s)^q$ for a desired s in the range of interest.

Equation (2.12) can be generalized as

$$\bar{x} = \frac{s^{-\frac{1}{\lambda}}}{\bar{j}_n} \left(1 - \sum_{z=1}^q \frac{(-1)^z s^z}{z!(z\lambda - 1)} \prod_{k=0}^{z-1} (q - k) \right) \Big|_{s_0}^s, \quad (2.57)$$

and Eq. (2.19) can be replaced by

$$s = \left[s_*^{\frac{q\lambda-1}{\lambda}} - (q\lambda - 1) \bar{j}_w (\bar{x} - \bar{x}_*) \right]^{\frac{\lambda}{q\lambda-1}}. \quad (2.58)$$

For a non-integer power q , the solution to Eq. (2.6) must be obtained numerically. Figure 2.7 shows that as the power q increases, the limiting current density decreases.

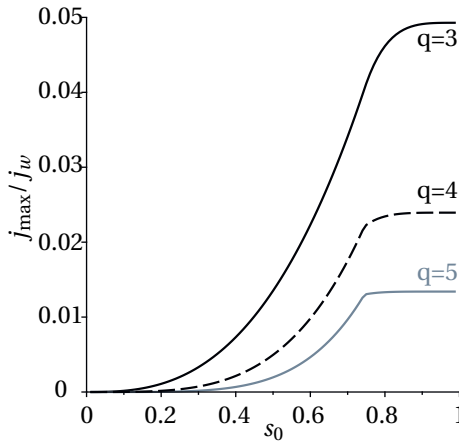


Figure 2.7: Effect of parameter ‘ q ’ in the power law of Eq. (2.54) on the limiting current density in a fuel cell obtained using Eq. (2.57) and Eq. (2.58) for the gaseous wetting phase layer parameters listed in Table 2.1.

2.E. APPROXIMATE SATURATION FOR GENERAL λ

The solution shown in Eq. (2.12) and Eq. (2.57) is valid for all values of λ except for integer values $r \equiv \frac{1}{\lambda}$. The solution for $r = \frac{1}{\lambda}$ can be written as:

$$\bar{x} = \frac{s^{-\frac{1}{\lambda}} - \left(\frac{q^{(q-1)} \ln s}{(-1)^r} + \sum_{\substack{r=1 \\ r\lambda \neq 1}}^q \frac{(-1)^r s^{r-\frac{1}{\lambda}} \prod_{k=0}^{r-1} (q-k)}{r!(r\lambda-1)} \right) \Big|_{s_0}}{\bar{J}_n}, \quad (2.59)$$

where $\binom{q-1}{r-1} = \frac{(q-1)!}{(q-r)!(r-1)!}$ is the binomial coefficient. For example, if $q = 3$ and $\lambda = 1$, Eq. (2.12) is not valid and therefore Eq. (2.59) can be written as:

$$\bar{x} = \frac{1}{\bar{J}_n} \left(\frac{s^2}{2} - 3s + \frac{1}{s} + 3 \ln s \right) \Big|_{s_0}^s, \quad (s > s_*), \quad (2.60)$$

which is the same expression as in Eq. (2.12) when we consider the limit $\lambda \rightarrow 1$. Under this limit, the term $\frac{3s^{1-\frac{1}{\lambda}}}{\lambda-1}$ becomes $3 \ln s$. Similarly, if $q = 3$ and $\lambda = 1/2$, (2.59) can be written as:

$$\bar{x} = \frac{1}{\bar{J}_n} \left(2s - \frac{6}{s} + \frac{1}{s^2} - 6 \ln s \right) \Big|_{s_0}^s, \quad (s > s_*). \quad (2.61)$$

If $q = 3$ and $\lambda = 1/3$, (2.59) can be written as:

$$\bar{x} = \frac{1}{\bar{J}_n} \left(\frac{1}{3s^3} - \frac{3}{2s^2} + \frac{3}{s} + \ln s \right) \Big|_{s_0}^s, \quad (s > s_*). \quad (2.62)$$

2.F. SURFACE AREA FROM SATURATION

The wetting phase saturation $s \equiv \frac{\mathcal{V}_w}{\mathcal{V}_{\text{pore}}}$, where \mathcal{V}_w is the volume of the pores occupied by the wetting phase and $\mathcal{V}_{\text{pore}}$ is the total volume of the pores. The total surface area of the pores covered by the wetting phase can be related to the capillary pressure as [96]

$$A_w = \frac{1}{\sigma |\cos(\theta)|} \int_0^{\mathcal{V}_w} p_c d\mathcal{V}_w. \quad (2.63)$$

The capillary pressure in the Brooks-Corey model [55] can be written as $p_c = p_t s^{-1/\lambda}$, where $p_t = 2\sigma |\cos(\theta)|/r_{\text{max}}$ and λ is the pore size distribution for the porous medium. Dividing Eq. (2.63) with $\mathcal{V}_{\text{tot}} = \mathcal{V}_{\text{pore}}/\epsilon$ gives

$$a_w = \frac{2\epsilon}{r_{\text{max}}} \int_0^s s^{-\frac{1}{\lambda}} ds = \frac{2\epsilon}{r_{\text{max}}} \frac{\lambda}{\lambda-1} s^{\frac{\lambda-1}{\lambda}}, \quad (2.64)$$

where $a_w \equiv A_w/\mathcal{V}_{\text{tot}}$ is the volumetric surface area covered by the wetting phase. It should be noted that Eq. (2.64) is only valid for $\lambda > 1$. For $\lambda \leq 1$, the integral diverges unless we define a minimum saturation. The reason is that for such a wide pore size distribution the smallest pores have an infinite surface area. When $s = 1$, Eq. (2.64) gives $a_{w,\text{max}} = \frac{2\epsilon}{r_{\text{max}}} \frac{\lambda}{\lambda-1}$, while at a saturation s the relative surface area covered by the wetting phase is given by

$$\chi \equiv \frac{a_w}{a_{w,\text{max}}} = s^{\frac{\lambda-1}{\lambda}}. \quad (2.65)$$

2.G. UDELL LEVERETT-J FUNCTION

The dimensionless capillary pressure p_c/p_t is often referred to as the Leverett J-function. In the main text we used $J(s) = s^{-\lambda}$. A particularly popular function is that by Udell [49]:

$$J(s) = 1.417(1-s) - 2.12(1-s)^2 + 1.263(1-s)^3 \quad (2.66)$$

Note that in Eq. (2.66) the capillary pressure vanishes for $s = 1$, the pressure p_t is no longer associated with the capillary pressure of the largest pores as in Eq. (2.5). Equation (2.6) is now replaced by

$$\frac{dJ(s)}{ds} \frac{ds}{d\bar{x}} = \frac{\bar{j}_n}{(1-s)^3} + \frac{\bar{j}_w}{s^3}, \quad (2.67)$$

Similar to the main text we can again introduce a non-wetting phase integral

$$I_n \equiv \int_0^s (1-s)^3 \frac{dJ(s)}{ds} ds \quad (2.68)$$

$$= (1-s)^4 \left(\frac{1.417}{4} - \frac{4.24(1-s)}{5} + \frac{3.789(1-s)^2}{6} \right) - 0.13775 \quad (2.69)$$

Note that Eq. (2.66) corresponds to a fixed normalized pore size distribution, so there is no free parameter like λ in the Brooks-Corey model. The slope $\left. \frac{1}{p_t} \frac{dp_c}{ds} \right|_{s=1} = -1.417$ using Eq. (2.66). This is equal to the $-1/\lambda$ of the Brooks-Corey model. The variation in capillary pressure however is much smaller for intermediate s . At $s = 0.5$, for example, the same slope is obtained for $\lambda \approx 9$. For s close to 1, solving $-1.417 \frac{ds}{d\bar{x}} = \frac{\bar{j}_n}{(1-s)^3}$, similar to Eq. (2.14), gives

$$s \approx 1 - (2.82 \bar{j}_n \bar{x})^{1/4} \quad (2.70)$$

Similarly, for $I_w(s)$, we have

$$I_w \equiv \int_0^s s^3 \frac{dJ(s)}{ds} ds \quad (2.71)$$

$$= -s^4(0.6315s^2 - 0.6676s + 0.2415) \quad (2.72)$$

The integrals Eq. (2.69) and (2.71) can be used in, for example, Eqs. (2.12), (2.12), and (2.34) to calculate for example j_{\max} and j_{\lim} .

2.H. THREE-REGIME SOLUTION

In the analysis of the main text, we always neglect one of the pressure gradients in Eq. (2.6). However, around s_* , both the wetting phase and the non-wetting phase pressure gradients are important. We define $s_{*,1}$ as the saturation above which the ratio $\frac{dp_n/dx}{dp_w/dx} = \frac{k_w j_w}{k_n j_n} \gtrsim 5$ and we neglect the wetting phase pressure gradient. We also define $s_{*,2}$ as

the saturation below which the ratio $\frac{dp_w/dx}{dp_n/dx} = \frac{k_n \bar{j}_n}{k_w \bar{j}_w} \gtrsim 5$ and we neglect the non-wetting phase pressure gradient. By using Eq. (2.6) and above definition for $s_{*,1}$ and $s_{*,2}$, we can write⁹

$$s_{*,1} = \frac{1}{1 + \left(\frac{\bar{j}_w}{5\bar{j}_n}\right)^{1/3}}, \quad \text{and} \quad s_{*,2} = \frac{1}{1 + \left(\frac{\bar{j}_w}{5\bar{j}_n}\right)^{1/3}}. \quad (2.73)$$

When $s > s_{*,1}$, we use Eq. (2.12) to calculate the saturation. When $s < s_{*,2}$, we use Eq. (2.19) to calculate the saturation. For $s_{*,1} < s < s_{*,2}$, we consider a linear variation of saturation. At $s_a \equiv (s_{*,1} + s_{*,2})/2$, using Eq. (2.6) we can write

$$\left. \frac{ds}{d\bar{x}} \right|_{\bar{x}=\bar{x}_a} = \left(\frac{\bar{j}_n}{(1-s_a)^3} - \frac{\bar{j}_w}{s_a^3} \right) \lambda s_a^{\lambda+1}. \quad (2.74)$$

The non-dimensional coordinates $\bar{x}_{*,1}$ at which $s = s_{*,1}$ and $\bar{x}_{*,2}$ at which $s = s_{*,2}$ are evaluated using Eq. (2.12) or Eq. (2.57). If $s_{*,2} < s_0 < s_{*,1}$, we take $\bar{x}_{*,1} = 0$ and $s_{*,1} = s_0$ in Eq. (2.74). In the linear part, we then have

$$s = s_{*,1} + (\bar{x} - \bar{x}_{*,1}) \left. \frac{ds}{d\bar{x}} \right|_{\bar{x}=\bar{x}_a}. \quad (2.75)$$

The limiting current for a three-regime analysis is given as

$$\frac{j_{\max}}{j_w} = \frac{s_{*,2}^{\frac{3\lambda-1}{\lambda}} - s_{\min}^{\frac{3\lambda-1}{\lambda}}}{(1 - \bar{x}_{*,2})(3\lambda - 1)}. \quad (2.76)$$

2.1. EXPRESSION FOR THE EFFECTIVE DIFFUSIVITY

We assume that the diffusion of gas through liquid is negligible and the diffusion flux of the reactant is a constant and given by Fick's law in the dilute limit as:

$$\frac{z_w j}{F} = D s^n \frac{dc}{dx}. \quad (2.77)$$

Integrating from $x = 0$ to $x = L$, we get,

$$c_1 - c_0 = \frac{jLz_w}{FD_{\text{eff}}}. \quad (2.78)$$

where the effective diffusivity

$$D_{\text{eff}} = \frac{D}{\int_0^1 s^{-n} d\bar{x}} \quad (2.79)$$

For a high- s design GDL $s \geq s_* \gtrsim 0.6$. When, furthermore $s_0 \approx 1$ we can use Eq. (2.15) to write

⁹We chose the ratio $\frac{dp_w/dx}{dp_n/dx} \gtrsim 5$ to neglect dp_w/dx and $\frac{dp_w/dx}{dp_n/dx} \gtrsim 5$ to neglect dp_n/dx as it gives the best approximation for the numerical solution. For values between 3 and 8, the analytical solution does not change significantly but for higher or lower values, the analytical solution gives a larger deviation.

$$\frac{D}{D_{\text{eff}}} = \int_0^1 s^{-n} d\bar{x} \approx \int_0^1 \left(1 - (4\lambda\bar{j}_n\bar{x})^{1/4}\right)^{-n} d\bar{x}, \quad (2.80)$$

To first order in $(4\lambda\bar{j}_n\bar{x})^{1/4}$ the integrand reads $1 + n(4\lambda\bar{j}_n\bar{x})^{1/4}$. Performing the integrating therefore gives to leading order $1 + \frac{4n}{5}(4\lambda\bar{j}_n)^{1/4} \approx \left(1 - \frac{4n}{5}(4\lambda\bar{j}_n)^{1/4}\right)^{-n}$. The second expression is a substantially more accurate approximation, with which Eq. (2.80) becomes

$$\frac{D}{D_{\text{eff}}} \approx \left(1 - \frac{4}{5}(4\lambda\bar{j}_n)^{1/4}\right)^{-n}. \quad (2.81)$$

For a low- s design GDL, we consider that $s < s_*$. Therefore we can write the effective diffusivity D_{eff} as:

$$\frac{D}{D_{\text{eff}}} = \int_0^1 s^{-n} d\bar{x} = \int_0^{\bar{x}_*} s^{-n} d\bar{x} + \int_{\bar{x}_*}^1 s^{-n} d\bar{x}, \quad (2.82)$$

clearly showing how the effective diffusion resistance proportional to $1/D_{\text{eff}}$ is split into the sum of the two resistances, one in the domain 0 to \bar{x}_* and the other in the domain \bar{x}_* to 1. Inserting Eq. 2.6 in Eq. (2.82) and neglecting the wetting phase pressure gradient for $\bar{x} < \bar{x}_*$ and the non-wetting phase pressure gradient for $\bar{x} > \bar{x}_*$, we can integrate by changing variables to give

$$\begin{aligned} \frac{D}{D_{\text{eff}}} &= \int_{s_0}^{s_*} \frac{-s^{-\frac{1}{\lambda}-m-1}(1-s)^3}{\lambda\bar{j}_n} ds + \int_{s_*}^{s_1} \frac{-s^{2-\frac{1}{\lambda}-m}}{\lambda\bar{j}_w} ds \\ &= \frac{\lambda_n}{\lambda} \left(\frac{\int_{s_0}^{s_*} (1-s)^3 ds^{-\frac{1}{\lambda_n}}}{\bar{j}_n} + \frac{\int_{s_*}^{s_1} ds^{3-\frac{1}{\lambda_n}}}{\bar{j}_w(1-3\lambda_n)} \right), \end{aligned} \quad (2.83)$$

where $\lambda_n \equiv \frac{\lambda}{n\lambda+1}$. These integrals are those of Eq. (2.12) and (2.18) with λ_n instead of λ . Therefore we can rewrite Eq. (2.83) as

$$\frac{D}{D_{\text{eff}}} = \frac{\lambda_n}{\lambda} \left(\frac{I_n^{\lambda_n} \Big|_{s_0}^{s_*}}{\bar{j}_n} + \frac{I_w^{\lambda_n} \Big|_{s_*}^{s_1}}{\bar{j}_w} \right) \quad (s_1 < s_*). \quad (2.84)$$

It is also possible to include the diffusion of liquid through the gas by interchanging the pressure gradients \bar{j}_n and \bar{j}_w in Eq. (2.83) and adding these two expressions to Eq. (2.83), forming a parallel circuit. Since diffusion of liquid in gas is much faster than the diffusion of gas in liquid, this effect is usually negligible.

3

MULTIPHASE FLOW MODEL FOR MEMBRANELESS GAS-EVOLVING FLOW-THROUGH POROUS ELECTRODES

Flow-through electrolyzers, with flow parallel to the current, are used in a wide range of industrial applications. The presence of flow avoids concentration gradients but can also be used to separate evolved gases, allowing membrane-less operation. In this work, we propose a simple multiphase flow-through electrode model. We derive and experimentally validate an analytical expression for the minimum velocity required to ensure effective gas separation. We show that this minimum velocity increases as a square root of current density for thin electrodes and linearly with current density for thick electrodes.

3.1. INTRODUCTION

Porous flow-through electrodes have been studied for a long time due to their superior mass transfer [97, 98]. Flow-through porous electrodes are traditionally used in electrosynthesis [99, 100], redox flow batteries [101–103], metals removal from waste streams [104–106], electrochemical destruction of cyanide [107, 108], and water electrolysis [109–113].

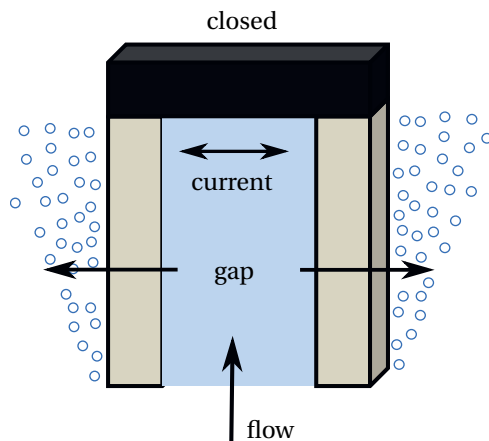


Figure 3.1: A schematic view of flow-through configuration considered with, inside the porous electrodes, flow parallel to the current, outwards from the gap, through the electrodes.

The flow in a porous electrode can be parallel to the current as in Fig. 3.1, normal, or a combination as in the interdigitated configuration [114]. A flow-through electrode with flow parallel to the current has traditionally in the literature often been referred to as flow-by [115, 116] a term nowadays, particularly in the flow battery literature, more commonly reserved for flow that largely bypasses the electrodes in a separate channel next to the electrodes, see e.g. [102, 117]. Here we will consider the flow configuration of Fig. 3.1 in which the flow enters in between and flows out through the electrode. This configuration has similarities with both crossflow and dead-end separators used for filtration.

In many electrochemical processes the gases are evolved in a liquid electrolyte, including the chlor-alkali process used for producing chlorine, the electrosynthesis of chlorate [118], or fluorine [119], the Hall-Héroult process for smelting aluminium, electrowinning of metals, various forms of CO₂ reduction [120], and water electrolysis.

Typically a membrane or separator is used to avoid gases crossing over to the opposing electrode where they may react back and cause inefficiencies, cause product impurity, or safety concerns as in the case of oxygen and hydrogen for example [121–123]. Various membraneless designs have also been proposed, for example based on selective coating [124] or lift forces on bubbles [125]. Since a membrane or separator adds costs, resistance, and potential degradation, there seems significant potential for membraneless designs. The design under consideration here uses outward flow to separate the produced gases, as depicted schematically in Fig. 3.1. This configuration was already

studied for water electrolysis in e.g. Refs. [109, 126, 127] but only recently its potential for membraneless operation has been highlighted in Refs. [110, 111, 128, 129].

Many studies have been devoted to modelling flow-through electrodes [115, 116, 130, 131] focusing mostly on mass transfer [127, 132, 133] while far fewer include the effect of gas evolution [134–138]. All these models assume that distinct bubbles move with a velocity proportional to the liquid velocity. This assumption is likely invalidated when the pores become smaller than the $100\ \mu\text{m}$ [118] that is typical for the diameter of electrolytically generated bubbles. For the small pores typically present in rocks or the diffusion layers of PEM fuel cells [35, 49, 50] and electrolyzers [32, 70, 71], often the assumption is made that gas forms continuous pathways rather than bubbles [16]. This can be likened to the annular flow regime in pipe flow. In this case Darcy's law, which supposes a linear relation between pressure gradient and velocity, can be assumed to hold approximately. Although this is a strong simplification with various limitations [139] we will discuss here the conclusions that follow from such a model and contrast it with the hitherto used bubble flow assumption.

A largely unanswered question is: what values for the various geometrical design parameters in Fig. 3.1, like electrode thickness, height, gap thickness, and pore size, are optimal from the perspective of energy efficiency. The answer crucially depends on both the flow direction and the minimum required flow rate. When flow is used for mass transfer, various useful references exist [115, 116, 131, 140, 141]. However, when flow is used to allow membrane-less operation of a gas-evolving electrolyzer very little is known. Reference [112] achieved, in a membraneless alkaline water electrolyzer, a current density of roughly $2\ \text{A}/\text{cm}^2$ at a cell voltage of 2.5 V and $4\ \text{A}/\text{cm}^2$ at 3.3 V. Compared to, typically much thinner, separators the used 2.5 mm gap seems to leave significant room for improvement. Smaller gaps however also require smaller pores, to ensure good distribution of flow, hence our interest in models beyond the assumption of bubbly flow.

Recently [113] an extremely high current density of $25\ \text{A}/\text{cm}^2$ was obtained at 3.5 V, for more than 100 hours, in an alkaline water electrolyzer with flow through a microfibre nickel felt *perpendicular* to the current. These results were obtained using an extremely thin polyethersulfone 0.1–0.15 μm thickness membrane, which showed immediate failure due to heat at even higher current densities.

The likely reasons that high multi-A/cm² current densities have been achieved in alkaline systems only in the presence of flow is likely due to flow-enhanced mass transfer of dissolved gases, electrolyte, and bubbles, reducing the Nernstian open-circuit potential or concentration polarization [142, 143], bubble overpotentials [144–146] and increase the limiting current density [123, 147], respectively.

Our primary goal here will be to determine the optimal geometrical and operational conditions for membrane-less flow-through electrolysis, to ascertain whether this can be competitive with conventional operation with a separator. A question that, however, first has to be answered is: what is the required flow velocity, as a function of current density, to allow membraneless operation.

3.2. MULTIPHASE FLOW-THROUGH ELECTRODE MODEL

3.2.1. GOVERNING EQUATIONS

In the model previously used in Refs. [134–138] and considered in 3.A.2, gas bubbles always move in the direction of the flow so that any non-zero velocity allows effective gas separation. Obviously, especially at large current densities, gas bubbles will also enter the gap between the electrodes, unless an unknown minimum flow-through liquid velocity is used. Here we consider a simple multiphase electrode model to obtain explicit analytical expressions for this velocity. We consider pores that are small compared to the electrode thickness so that an average description over many pores can be used. The gas will be assumed to form continuous pathways so that the extended Darcy equation can be used.

For a hydrophilic electrode, we may use the following differential equation, discussed in more detail in section 2.2, to describe the liquid fraction or *saturation* s ,

$$\frac{dp_t s^{-1/\lambda}}{dx} = -\frac{\mu_g U_g}{K(1-s)^n} + \frac{\mu_l U_l}{K s^n}. \quad (3.1)$$

The left-hand side shows the derivative of the capillary pressure, the gas pressure minus the liquid pressure, with respect to the x -coordinate through the electrode; with $x = 0$ upstream, at the gap, and $x = L$ downstream, at the rear. According to Darcy's law, the gas and liquid pressure gradients are proportional to the gas and liquid superficial velocities U_g and U_l and viscosities μ_g and μ_l . The capillary pressure $p_t s^{-1/\lambda}$ is related to the saturation through the Brooks-Corey relation, with λ the pore size distribution index - a smaller value corresponding to a more narrow distribution. The threshold pressure p_t is the capillary pressure at $s = 1$, so corresponding to the largest pore. It is routinely measured in the analytical porosimetry technique as the 'bubble point pressure', the minimum pressure that has to be applied to the gas phase on one side of a porous medium to see bubbles appearing on the other side.

The permeability K for the liquid is reduced by the presence of the gas through the 'relative permeability' s^n , and similarly $(1-s)^n$ for the gas permeability. Although actually only consistent with the Brooks-Corey relation for $n = 3$ in the limit $\lambda \rightarrow \infty$ [65] (see section 2.2), often a power-law fits well to experiments, see for example Ref. [148]. We note that in the following analysis, approximations near $s = 1$ are used.

Approximating the pores as cylinders with a maximum diameter d_{\max} we can write ¹

$$p_t = \frac{4\sigma}{d_{\max}}, \quad K = c_1 \epsilon^3 d_{\max}^2. \quad (3.2)$$

Here ϵ is the porosity and c_1 a material-dependent parameter [16, 64–66].

If both the gas and the electronic current move to the right through the porous electrode, the gas velocity U_g will be proportional to local electronic current density i by Faraday's law as

$$U_g = \frac{z_i v_m i}{F}. \quad (3.3)$$

¹Assuming a strongly water wetting medium with zero contact angle θ , otherwise we may replace σ with $\sigma \cos\theta$. We have $c_1 = \frac{\alpha}{16} \frac{\lambda}{\lambda+2}$ in the notation of [66] where $\alpha = z_i \beta$ in the notation of Ref. [65].

Here the gas molar volume of an ideal gas $V_m = RT/p$, z_i is the stoichiometric coefficient for a single electron transfer, and F is Faraday's constant giving the charge of a mole of electrons.

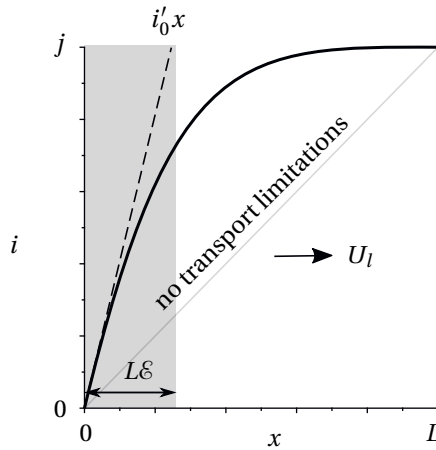


Figure 3.2: A possible profile of the electronic current i throughout the electrode, with most of the current generated in the shaded region within a distance εL to the gap, minimizing the ohmic drop that ions have to travel.

At the gap side $x = 0$ both U_g and i vanish, and at the rear both are at their maximum and $i(x = L) = j$ the current density magnitude. In general we can write $i'_0 \equiv \left. \frac{di}{dx} \right|_{x=0} = \frac{1}{\varepsilon} \frac{j}{L}$, in terms of the electrode effectiveness factor ε as illustrated in Fig. 3.2. Using the approximation of Eq. (3.17) this gives

$$i'_0 \approx \frac{j}{L} \left(1 + \frac{jL}{2\kappa b} \right), \quad \kappa \approx \varepsilon^{1.5} \kappa_0. \quad (3.4)$$

The effective conductivity of the porous electrode is often approximated by the Bruggemans relation $\kappa \approx \varepsilon^{1.5} \kappa_0$ in terms of the electrolyte conductivity κ_0 . Here we neglect the influence of the gas fraction, which we show in 3.A to be modest, consistent with the approximation that s is close to 1.

3.2.2. NUMERICAL SOLUTIONS

Figure 3.3 shows the solution to Eqs. (3.1) and (3.3) for a linearly varying current density $i = (x/L)j$ and a boundary condition $s(x = L) = 0.999$. The actual value used for $s(x = L)$ is not of much influence for the solution near $x = 0$. The produced gases hydrogen and oxygen are created in dissolved form first and advected with the flow, before a sufficiently high supersaturation causes nucleation of gas bubbles that grow and coalesce. We therefore assume that a minimum saturation $s(x = 0) = s_0$, which can be slightly below unity, will allow effective membrane-less operation without bubbles entering the gap. Next, we aim to find an analytical expression for the associated minimum liquid velocity.

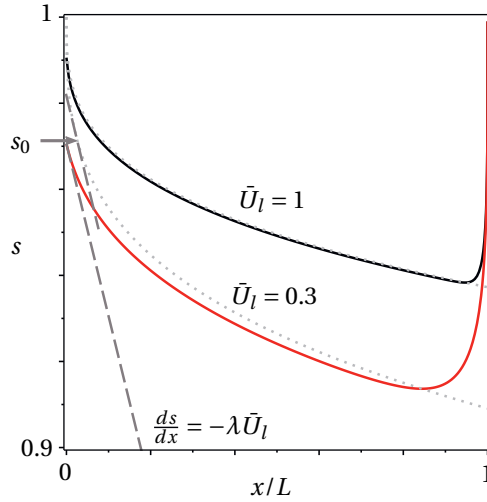


Figure 3.3: The saturation profile throughout the electrode from solving Eqs. (3.1) and (3.3) with a linearly current density profile, or $\frac{ds^{-1/\lambda}}{d(x/L)} = -\frac{\bar{j}(x/L)}{(1-s)^n} + \frac{\bar{U}_l}{s^{\bar{n}}}$ with $n = 3$, $\lambda = \frac{4}{3}$, $\bar{j} \equiv \frac{\mu_g L}{K p_t} \frac{z_i V_m j}{F} = 3 \cdot 10^{-4}$, and $\bar{U}_l \equiv \frac{\mu_l U_l}{K p_t} = 1$ and 0.3. At the rear side, we somewhat arbitrarily assumed $s(L) = 0.999$ but the exact value can be seen to impact only the solution near $x = L$. As the liquid velocity is decreased, $s(x = 0)$ decreases which could result in an accumulation of gas bubbles near the entrance. Over most of the domain the right-hand side of Eq. (3.1) approximately vanishes so that $s \approx 1 / (1 + (\bar{j}(x/L) / \bar{U}_l)^{1/n})$, a solution that is indicated by the dotted lines. Equating the derivative of this solution to that of the solution near $x = 0$, indicated by the grey dashed lines, we obtain $s_0 \approx 1 - \sqrt{\bar{j} / n \lambda} / \bar{U}_l = 0.99$ and 0.97 for $\bar{U}_l = 1$ and $\bar{U}_l = 0.3$, respectively, in agreement with the numerical result. This expression for s_0 is used to derive Eq. (3.5).

3.2.3. ANALYTICAL SOLUTION

The numerical solutions reveal two distinctive features that can be used to find an analytical approximation for the required liquid velocity. First, the second term in Eq. (3.1), representing the frictional pressure gradient due to liquid flow, dominates near $x = 0$ when $s_0 \approx 1$. Locally, this allows the equation to be approximated by $-\frac{1}{\lambda} p_t s' = \frac{\mu_l U_l}{K}$.

A second observation from the numerical solutions of Fig. 3.3 is that, in the rest of the domain, the two terms in Eq. (3.1) approximately cancel so that $(\frac{1-s}{s})^n \approx \frac{\mu_g U_g}{\mu_l U_l}$. Taking the derivative of this expression at $x = 0$ gives $-n(1-s_0)^{n-1} s_0^{-n-1} s' \approx \frac{\mu_g U_g'}{\mu_l U_l}$, where $U_g' \equiv \frac{dU_g}{dx} \Big|_{x=0} = \mu_g K p_t U_g' / n \lambda \mu_l^2$. This solution for s_0 was compared with the numerical result and found to give excellent agreement as long as $s_0 \gtrsim 0.9$. From Eqs. (3.3) and Eq. (3.4) $U_g' = \frac{z_i V_m j}{F} \frac{j}{L} \left(1 + \frac{jL}{2\kappa b}\right)$ so that with Eq. (3.2) we obtain

$$U_l = \sqrt{\frac{c_2 j d_{\max}}{L} \left(1 + \frac{jL}{2\kappa b}\right)}, \quad (3.5)$$

with $c_2 = \frac{4\sigma c_1 \epsilon^3 s_0^{n+1}}{n \lambda (1-s_0)^{n-1}} \frac{\mu_g}{\mu_l^2} \frac{z_i V_m j}{F}$ [$\text{m}^4/\text{C}/\text{s}$]. If we assume that the minimum s_0 re-

quired to avoid bubbles in the gap is approximately constant, Eq. (3.5) gives an expression for the minimally required liquid velocity. This velocity is predicted to increase with $\sqrt{j/L}$ or j for electrodes that are thin or thick relative to $\kappa b/j$, respectively. The associated value of s_0 in this model is a constant that has to be obtained from experiments.

3.3. EXPERIMENTAL VALIDATION

To validate the above model predictions, we consider a typical “filter press”-like [149–151] alkaline water electrolyzer setup used in [15]. Two different configurations are considered using Ni-felt electrodes with a maximum diameter $d_{\max} = 8 \mu\text{m}$, porosity $\epsilon = 0.75$ and permeability $K = 1.3 \times 10^{-13} \text{ m}^2$. In configuration 1, nylon 1 mesh with $d_{\max} = 35 \mu\text{m}$ and thickness $53 \mu\text{m}$ is pressed to the electrodes, while in configuration 2, a much coarser nylon 2 mesh with $d_{\max} = 1930 \mu\text{m}$ is used as a spacer to fill the entire gap of $1100 \mu\text{m}$, see Fig. 3.4.

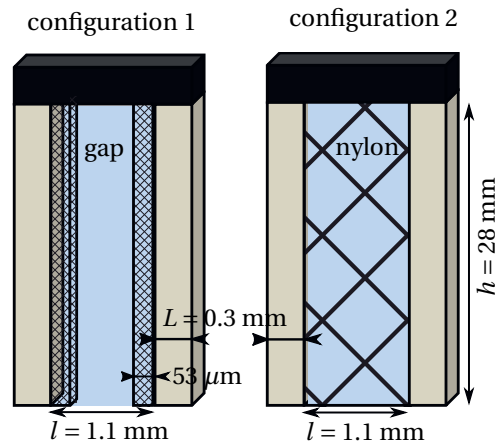


Figure 3.4: In Configuration 1, nylon meshes of thickness $53 \mu\text{m}$, aperture $d_{\max} = 35 \mu\text{m}$, and dimensions slightly larger than the electrodes, are pressed to the electrodes at their circumference by a 1 mm thick rubber gasket. In Configuration 2, a nylon mesh of thickness 1.1 mm and aperture $d_{\max} = 1.93 \text{ mm}$ is used as a spacer between the electrodes.

In Fig. 3.5, the time-averaged steady-state cell voltage for configuration 1 of Fig. 3.4 with the Ni-felt electrode, as a function of liquid flow rate, for three different current densities is shown. The cell voltage at largest used flow rate is subtracted in these results. We see a dramatic increase of almost 1.5 V for $j = 4000 \text{ A/m}^2$, which can be explained by an additional ohmic drop introduced by gas accumulating in front of and inside the electrode. This was further investigated in Ref. [15] using a dedicated visually accessible setup. The additional voltage disappears after applying a larger flow rate showing that bubbles can be pushed into the electrodes.

We define, somewhat arbitrarily, a threshold voltage for bubble-induced losses as 0.1 V. The threshold voltage will relate, among other experimental conditions, to the saturation s_0 . The velocity required to keep the bubble-induced losses below 0.1 V is termed minimum liquid velocity and is plotted in Fig. 3.6.

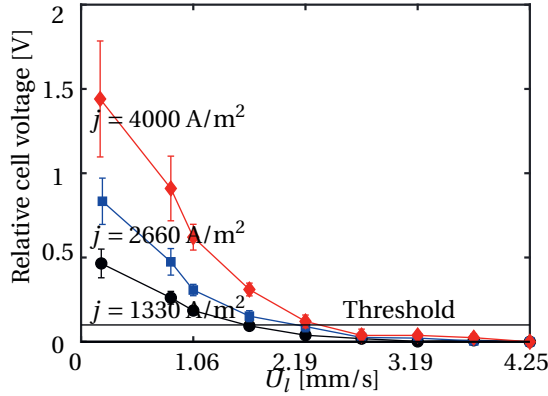


Figure 3.5: The relative cell voltage measured in configuration 1 with nickel felt electrodes, as a function of the superficial liquid velocity, for three different current densities. We subtracted the cell voltage ≈ 2.4 , 2.85 , and 3.5 V recorded at the maximum flow rate for the three current densities, respectively. The horizontal solid line is the threshold of 100 mV used in Fig. 3.6.

With the values from Table 3.1 we have $2\kappa b/L \approx 1.3$ A/cm² so that, in the range of current densities of Fig. 3.6, Eq. (3.5) predicts that the minimum liquid velocity scales approximately with $\sqrt{j/L}$. This proportionality is indeed approximately observed in the data of Fig. 3.6, where the required liquid velocity increases sub-linearly with current density. As an additional test, we also checked the dependence on electrode thickness with $L = 600$ μm . As predicted by Eq. (3.5) a lower liquid velocity is indeed required in this case.

The solid lines in Fig. 3.6 indicate Eq. (3.5) with a coefficient $c_2 = 5 \cdot 10^{-8}$ m²/C/s, showing reasonable agreement for both $L = 300$ μm and 600 μm . With the parameters of Table 3.1 this gives $s_0 \approx 0.97$, well within the range in which Eq. (3.5) is successfully verified against numerical simulations of Eq. (3.1).

Table 3.1: Approximate values used in the calculations, relevant for hydrogen evolution in configuration 1 with 30 w% KOH at ambient conditions. We calculate the effective electrode conductivity from $\kappa \approx \kappa_{\text{el}} e^{1.5}$ with $\epsilon = 0.75$ and $\kappa_{\text{el}} \approx 60$ S/m [152], the molar volume from $V_g = RT/p$, and the Tafel slope from $b = RT/\alpha F$ with charge transfer coefficient $\alpha = 1/2$. The order of magnitude values in the second table were estimated from the measurements in Ref. [15] with $n = 3$.

μ_l	2	mPa s
μ_g	8.4	$\mu\text{Pa s}$
κ	40	S/m
b	50	mV
V_g	25	l/mol
σ	73	mN/m
z_i	1/2	-

Ni-felt - conf. 1		
p_t	0.37	bar
K	10^{-13}	m ²
λ	4/3	-
c_1	$5 \cdot 10^{-3}$	-
c_2	$5 \cdot 10^{-8}$	$\frac{\text{m}^4}{\text{Cs}}$
s_0	0.97	-

We also performed similar validation for configuration 2 of Fig. 3.4. In this case a larger liquid velocity is required. The obtained value of $c_2 = 10^{-7} \text{ m}^4/\text{Cs}$ corresponds with the values in Table 3.1 with $s_0 \approx 0.98$. It seems likely that the hydrophilic nylon 1 with its relatively small aperture size of $35 \text{ }\mu\text{m}$ of nylon 1, not too dissimilar from the pore sizes of the Ni felt, avoids bubbles to enter the gap. Comparing with tests without a nylon spacer, an added advantage seems to be that bubbles trapped in the gap can be removed again upon increasing the flow rate. The aperture size of nylon 2 is, however, too large, both compared to the felt pore sizes as well as typical bubble sizes, to have a strong positive influence.

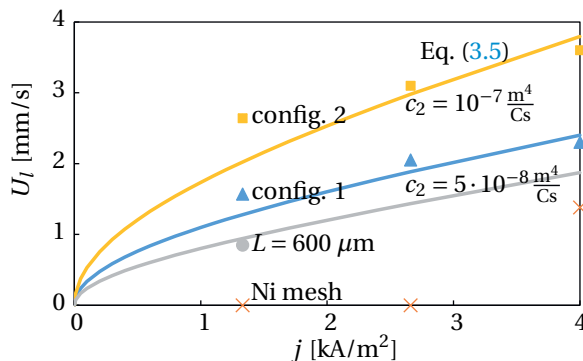


Figure 3.6: The measured minimum required liquid velocity U_l to keep the bubble associated overpotential below 0.1, as outlined in Fig. 3.5. For configuration 1 (diamonds) we varied both the electrode thickness (circles) and the aperture size (crosses). The continuous lines show a comparison with Eq. (3.5) using $c_2 = 5 \cdot 10^{-8} \text{ m}^2/(\text{Cs})$. For configuration 2 (squares) a larger value $c_2 = 1 \cdot 10^{-7} \text{ m}^2/(\text{Cs})$ is required to obtain a reasonable agreement, while for the Ni-mesh we do expect a bubbly flow regime in which the theory behind the equation does not hold.

3.4. DISCUSSION

We have made various simplifications in the analyses that warrant further discussion. First of all, our assumption of a flow regime in which the gas forms a continuous phase rather than dispersed bubbles is likely valid for small enough pores, but the exact conditions under which Darcy's law holds are still under investigation [139]. For definiteness we assumed power-law dependences on the liquid saturation of the relative permeabilities and capillary pressure in Eq. (3.1), but these can easily be replaced by different forms in the derivation of Eq. (3.5). Note that, since the derivation considers high liquid saturations, the model parameters are ideally obtained from empirical fits in this same range.

We considered the porous anode and cathode to have similar properties and focussed on hydrogen evolution in application to water electrolysis. We note that the dynamic viscosity μ_g of oxygen is roughly twice that of hydrogen but also $z_i = 1/2$ is half that for hydrogen evolution, so that the relevant quantity $z_i \mu_g$ in c_2 is similar.

3.5. CONCLUSION

We studied here the potential of flow-through electrodes for membraneless operation in case of gas-evolving reactions. To minimize ohmic dissipation a small gap between the electrodes is preferred, increasing pumping losses. Therefore, an important parameter is the minimally required flow velocity that allows effective membraneless operation without bubbles entering the gap. Previously studied bubble models cannot give insight into this parameter, nor are they suitable to describe electrodes with small pores. Small pores are preferred for their high reactive surface area and sufficient pressure drop to allow a homogeneous flow distribution. Therefore, we studied a multiphase Darcy-flow model from which we derived a simple analytical relation, Eq. (3.5), for the required liquid velocity. This relation was successfully verified with respect to numerical simulations and validated against experimental data.

APPENDICES

3.A. ACTIVATION OVERPOTENTIAL

3.A.1. GENERAL EQUATIONS

The superficial gas velocity is given by Faraday's law as

$$U_g = \frac{z_i V_m}{F} i, \quad (3.6)$$

where i is the electronic current density, which varies from $i = 0$ at $x = 0$ to $i = j$ at $x = L$. Assuming the electrode conductivity is much higher than the electrolyte conductivity and assuming negligible concentration gradients of electrolyte and reactants, Ohm's law and the Tafel equation can be written as [75]

$$\frac{d\eta}{dx} = \frac{j - i}{\kappa s^q}, \quad (3.7)$$

$$\frac{di}{dx} = j_* a e^{\eta/b}. \quad (3.8)$$

Here the surface overpotential η is equal to a constant minus the electrolyte potential, a is the active volumetric surface area, and b is the Tafel slope. We assumed the effective electrode conductivity can be written as κs^q with exponent q , often taken to be 1.5 or 2, to account for the presence of gas [153, 154]. Equation 3.8 gives the overpotential at $x = 0$ as

$$\eta_0 = b \ln \left(\frac{j}{a L j_* \varepsilon} \right), \quad (3.9)$$

where the effectiveness factor $\varepsilon \equiv \frac{j}{L i_0}$.

3.A.2. BUBBLE FLOW REGIME

For completeness and comparison we provide here the analysis for larger pore sizes in which a bubble flow regime may be assumed. The average interstitial gas and liquid velocities, u_g and u_l , are related to superficial velocities, U_g and U_l , as

$$u_g = \frac{U_g}{\varepsilon(1-s)}, \quad u_l = \frac{U_l}{\varepsilon s}. \quad (3.10)$$

Assuming the gas bubbles move with a fraction $f \equiv u_g/u_l$ of the liquid velocity, Eqs. (3.10) and (3.6) combine to give

$$s = \frac{1}{1 + ri/j}, \quad r \equiv \frac{jz_i V_m}{fU_l F}, \quad (3.11)$$

with rf the ratio U_g/U_l at $x = L$. Taking a derivative of Eq. (3.8) with respect to x and inserting Eqs. (3.7) and (3.11) gives

$$\frac{d^2 i}{dx^2} = \left(1 + r \frac{i}{j}\right)^q \frac{j-i}{b\kappa} \frac{di}{dx}. \quad (3.12)$$

With $z \equiv \frac{di}{dx}$, we have $\frac{d^2 i}{dx^2} = z \frac{dz}{di}$ so that Eq. (3.12), using Eq. (3.8), can be written as

$$\frac{d}{di} \left(j_* a e^{\eta/b} \right) = \left(1 + r \frac{i}{j}\right)^q \frac{j-i}{b\kappa}. \quad (3.13)$$

For constant parameters, we can integrate with respect to i between $i(0) = 0$ and $i(L) = j$ to give

$$e^{\eta_0/b} - e^{\eta_L/b} = \frac{j^2}{2j_* a b \kappa_{\text{eff}}}, \quad (3.14)$$

where

$$\frac{\kappa}{\kappa_{\text{eff}}} = \frac{2}{r(1+q)} \left(\frac{(r+1)^{q+2} - 1}{r(2+q)} - 1 \right). \quad (3.15)$$

In the presence of bubbles, the effective conductivity κ_{eff} decreases below κ . With, for example $q = 1, 2$ or 3 , Eq. (3.15) simplifies to

$$\frac{\kappa}{\kappa_{\text{eff}}} = 1 + r \times \begin{cases} \frac{1}{3} & q = 1 \\ \frac{2}{3} + \frac{r}{6} & q = 2 \\ 1 + \frac{r}{2} + \frac{r^2}{10} & q = 3. \end{cases} \quad (3.16)$$

For high current densities we can neglect the term on the left-hand side of Eq. (3.14) with respect to the first, to obtain Eq. (3.9) with the electrochemical Thiele modulus $1/\varepsilon_{jL/\kappa_{\text{eff}}b \rightarrow \infty} = jL/2\kappa_{\text{eff}}b$. This is equal to the ohmic drop of ions reacting halfway the electrode at this effective conductivity [75, 155, 156]. Using the approximation of Ref. [75] we may write

$$\varepsilon \approx \frac{1}{1 + jL/2\kappa_{\text{eff}}b}. \quad (3.17)$$

With this, a general expression

$$\eta_0 \approx b \ln \left(\frac{j}{j_* a L} + \frac{j^2}{2b\kappa_{\text{eff}} j_* a} \right), \quad (3.18)$$

is obtained. To explain the measured overpotentials of 0.1–0.5 V in Ref. [138] required unrealistically high gas fractions $s_0 \geq 0.85$ associated with a very small slip factor $f = u_g/u_l \approx 0.0016$. Visual observations from the set-up of Ref. [15] rather showed $f \approx 1.8$.

3.A.3. DARCY FLOW REGIME

As mentioned in the main text, numerical simulations with $s_0 \approx 1$ show that over most of the domain the two terms of Eq. (3.1) approximately balance so that

$$s \approx \frac{1}{1 + \left(\frac{\mu_g U_g}{\mu_l U_l}\right)^{1/n}}. \quad (3.19)$$

Comparing with Eq. (3.11) we can redo the above analysis replacing ri/j with $R(i/j)^{1/n}$ in Eq. (3.13), where

$$R^n = \frac{\mu_g j z_i V_m}{\mu_l F U_l} = \frac{\mu_g z_i V_m}{\mu_l F} \sqrt{\frac{2\kappa b}{c_2 d_{\max}}}, \quad (3.20)$$

is the ratio between gas and liquid velocities at $x = L$ times the ratio μ_g/μ_l . In the second equality of Eq. (3.20), we neglected the first term in Eq. (3.5) so that $U_l = j\sqrt{c_2 d_{\max}/2\kappa b}$. This is valid for large current densities or thick electrodes. Integrating Eq. (3.13) with $R(i/j)^{1/n}$ instead of ri/j gives, for example with $n = 3$

$$\frac{\kappa}{\kappa_{\text{eff}}} = 1 + R \times \begin{cases} \frac{1}{10} & q = 1 \\ \frac{1}{5} + \frac{R}{28} & q = 2 \\ \frac{3}{10} + \frac{3R}{28} + \frac{R^2}{55} & q = 3. \end{cases} \quad (3.21)$$

With the values from Table 3.1 for Ni-felt and, say, $C = 30$ mM, we obtain $R \approx 0.1$. From Eq. (3.21) this gives $\frac{\kappa}{\kappa_{\text{eff}}} \leq 1.2$ when $q \leq 3$, so only a small correction.

4

AN ANALYTICAL MULTIPHASE FLOW MODEL FOR PARALLEL PLATE ELECTROLYZERS

Membraneless parallel-plate electrolyzers use electrolyte flow to avoid product crossover. Using a mixture model neglecting inertia, and assuming an exponential gas fraction profile, we derive approximate analytical expressions for the velocity profile and pressure drop for thin plumes. We verify these expressions using numerical solutions obtained with COMSOL and validate them using experimental data from the literature. We find that the wall gas fraction increases rapidly at small heights, but becomes fairly constant at larger heights. These expressions serve as a guiding framework for designing a membraneless parallel-plate electrolyzer by quantifying the maximum possible height. We find that buoyancy driven membraneless parallel-plate electrolyzers with a typical 3 mm gap can be designed with a maximum height of around 7.6 cm at 1000 A/m² for operation with 98% product purity at atmospheric pressure. For a forced flow at Re= 1000, the same electrolyzer can be made around 17.6 cm tall at 1000 A/m². These limits can be further improved with smaller bubbles or higher pressure.

4.1. INTRODUCTION

Clean hydrogen can be produced by splitting water in electrolyzers using electricity from renewable sources. Traditionally, a membrane or a separator is used between the cathode and the anode that allows the transport of ions and separates the gaseous products. However, these membranes and separators are susceptible to degradation [158], gas crossover [159] or blockage in the presence of impurities [160] reducing the durability of the electrolyzer.

Membraneless electrolyzers have been studied as one of the promising alternatives to existing electrolyzer technologies. Various designs for membraneless operation of electrochemical cells have been studied including flow-through porous electrodes [15, 110, 128, 158, 161] and flow-by electrodes [103, 124, 162–164]. Esposito [128] provides a good overview of challenges and opportunities for membraneless electrolyzers. In this paper, we deal with electrolyzers without a separator, diaphragm or membrane, where the flow is parallel to the electrodes. Such electrolyzers may offer potential reduction in costs and ohmic resistance.

Previous experimental studies have focused on demonstrating the use of flow to mitigate gas crossover [110, 124, 162, 164, 165]. Pang et al. [165] recently made the first attempt to systematically explore the performance limits and trade-offs between various parameters such as current density, efficiency, product purity, and electrode size in membraneless parallel plate electrolyzers. In the past, many researchers studied the gas evolution between vertical electrodes with narrow interelectrode gap using experiments [118, 166–170] and numerical simulations [161, 171–176] to investigate the two-phase hydrodynamics. Very few researchers made an attempt to analytically model the two-phase flow in a membraneless parallel plate electrolyzer [172, 177–180]. In this work, we develop an analytical model for a membraneless parallel plate electrolyzer without a separator, see Fig. 4.1. We first introduce a numerical model to simulate the multiphase flow under laminar flow conditions in section 4.2. Using the insights from the numerical model and governing equations, we derive approximate analytical expressions in section 4.3 for the velocity profile, superficial velocity, shear stress, and pressure drop. Finally, we provide an expression for the maximum height of the electrolyzer based on interelectrode gap and flow conditions in section 4.5.

4.2. MATHEMATICAL MODEL

4.2.1. MODEL CONFIGURATION

Figure 4.1 shows a configuration of a membraneless parallel plate electrolyzer. The coordinates z and x represent the vertical and wall-normal directions, respectively. The vertical electrodes have a height h and are assumed to have a depth much larger than the interelectrode gap l . This allows us to represent the electrolyzer in 2D. The bubbles in the electrolyzer move in a plume of e-folding thickness $\delta_g(z)$, which is expected to become thicker with height as more gas is generated. The wall gas fraction on the electrode surface is denoted by ε_0 . The liquid electrolyte enters with a vertical interstitial velocity $w(x)$ because of forced flow or buoyancy due to the presence of the bubbles. The heights for the entrance region and the exit region are denoted by h_{en} and h_{exit} .

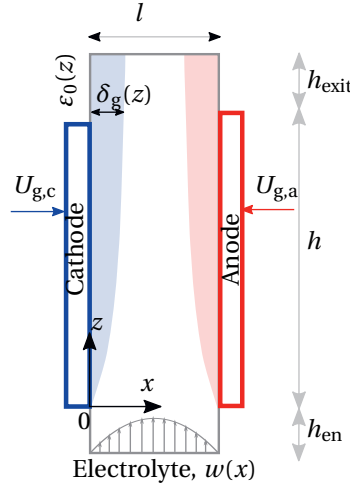


Figure 4.1: Configuration of a membraneless parallel plate electrolyzer. The gas bubbles are generated at the electrode surface and move in a plume of e-folding width δ_g . The wall gas fraction is denoted by ε_0 . The liquid electrolyte moves vertically with interstitial velocity $w(x)$.

4.2.2. NUMERICAL MODEL

We model the two-phase hydrodynamics for laminar flow in the electrochemical cell with the mixture model formulation [171, 172, 181] using COMSOL Multiphysics v5.6, update 2 [182]. The mixture model formulation is valid when the gaseous phase is in equilibrium with the liquid phase. This is a reasonable approximation for small electrochemical bubbles that have a much smaller density than that of the liquid electrolyte. We assume that the gas bubbles are spherical due to their small diameter d_b and that the presence of high molarity electrolytes prevents coalescence [183–185]. The velocities of the liquid phase and the gas phase are denoted by \mathbf{u} and \mathbf{u}_g , respectively, while the gas fraction is denoted by ε . The mixture dynamic viscosity $\mu_m = \mu\mu_r = \frac{\mu}{1-\varepsilon}$ [186], where μ is the dynamic viscosity of the liquid electrolyte and $\mu_r = \frac{1}{1-\varepsilon}$. The mixture density $\rho_m = (1-\varepsilon)\rho + \varepsilon\rho_g$ where ρ_g and ρ are the densities of the gaseous and the liquid phase, respectively. Note that we do not use any subscript for the properties corresponding to the liquid phase, but use subscript 'g' for the properties corresponding to the gaseous phase. The continuity equation for the mixture in steady state is

$$\nabla \cdot (\rho_m \mathbf{U}_m) = 0, \quad (4.1)$$

and the momentum equation for the mixture at steady state is

$$\rho_m \mathbf{U}_m \cdot \nabla \mathbf{U}_m = -\nabla p + \nabla \cdot (\mu_m (\nabla \mathbf{U}_m + (\nabla \mathbf{U}_m)^T)) - \rho_m g \hat{\mathbf{z}}, \quad (4.2)$$

where $\mathbf{U}_m = (1-\varepsilon)\mathbf{u} + \varepsilon\mathbf{u}_g = \mathbf{u} + \varepsilon\mathbf{u}_s$ is the superficial mixture velocity. The difference between the gas and the liquid interstitial velocity is the slip velocity $\mathbf{u}_s \equiv \mathbf{u}_g - \mathbf{u}$. Riviere and Cartellier [180] use a different closure relation for shear stress giving μ instead of

μ_m in the second term of Eq. (4.2). However, past works show that the effective mixture viscosity increases with an increase in gas fraction, and even diverges above a certain maximum gas fraction [187–189]. Nonetheless, In this work we have provided relations for both cases – a constant mixture viscosity case in the main text and a gas fraction dependent increasing mixture viscosity in 4.A.

The continuity equation for the gaseous phase for laminar flow in steady state assuming constant gas density, using $\mathbf{U}_s = \varepsilon(1 - \varepsilon)\mathbf{u}_s$, can be rewritten as

$$\mathbf{U}_m \cdot \nabla \varepsilon = -\nabla \cdot \mathbf{U}_s. \quad (4.3)$$

We describe the relative motion of the gas bubbles as the superposition of relative motion due to various phenomena by writing

$$\mathbf{u}_s = \mathbf{u}_{St} + \mathbf{u}_{Sa} + \mathbf{u}_{Hd} + \mathbf{u}_{Sd} + \mathbf{u}_{Sm}, \quad (4.4)$$

In Eq. (4.4), we expressed the total slip velocity as a superposition of five different components. We describe below the physical meaning of each of these slip velocities. The first term \mathbf{u}_{St} arises due to the balance between buoyancy and drag force and gives a slip velocity equal to the rise velocity of the bubble in liquid, $\mathbf{u}_{St} = f(\varepsilon) \frac{\rho g d_b^2}{18\mu} \hat{\mathbf{z}}$. Here, $f(\varepsilon) = (1 - \varepsilon)^4$ is a hindrance function for a swarm of particles [190, 191]. Note that we used a power 4 in the hindrance function to give expressions similar to [172], while Ref. [190] and Ref. [191] find a slightly higher power of 4.65 and 5, respectively. However, we checked our simulations with these slightly higher powers in the hindrance function and find negligible differences in the numerical results. There have been some other works which suggest that the bubble swarm velocities may be higher than for a single isolated bubble [184, 192, 193].

The exact expression for $f(\varepsilon)$ is, therefore, debatable. Smaller powers of $(1 - \varepsilon)$ in $f(\varepsilon)$ would make the gas plumes more exponential in shape, leading to a better accuracy of our model. The drag force is assumed to be Stokes' drag, which is valid for $\text{Re}_{St} = f(\varepsilon) \frac{\rho^2 g d_b^3}{18\mu^2} \ll 1$. For $\varepsilon \rightarrow 0$, this corresponds to a bubble diameter of approximately 100 μm . However, with higher gas fractions usually observed in electrolyzers, the error becomes smaller for larger bubble diameters.

The second term \mathbf{u}_{Sa} corresponds to the Saffman lift force experienced by the particles translating and rotating in a velocity gradient [194–196]. The Saffman lift acts in a direction perpendicular to the vorticity vector and the slip velocity vector. In a buoyancy driven flow, $\frac{\partial w}{\partial x} \gg \frac{\partial u}{\partial z}$ and the slip velocity due to buoyancy is dominant in the vertical direction. So, as a simplification, we assume that the Saffman lift force is given by $\mathbf{u}_{Sa} = 0.17 w_{St} \sqrt{\frac{d_b^2}{\mu} \left| \frac{\partial w}{\partial x} \right|} \text{sign} \left(\frac{\partial |w|}{\partial x} \right) \hat{\mathbf{x}}$ [194] and acts only in the wall-normal direction. The Saffman lift force tends to push the bubbles from a region of high velocity to a region of low velocity. It should be noted that here we neglected the vertical component of the Saffman lift force because it is expected to be much smaller than w_{St} .

The third term \mathbf{u}_{Hd} is due to collision-like interaction between bubbles, similar to hydrodynamic dispersion of suspended particles [171, 172, 191, 197, 198], given by $\mathbf{u}_{Hd} = -\frac{d_b w_{St}}{2} \frac{\mathcal{D} \cdot \nabla \varepsilon}{\varepsilon}$. Here, $\mathcal{D} = \begin{pmatrix} 1 & 0 \\ 0 & 8 \end{pmatrix}$ is a non-isotropic dimensionless dispersion tensor [191].

Inserting the expression of \mathbf{u}_{Hd} in Eq. (4.3) gives a diffusion term $\nabla \cdot (\mathcal{D}_{\text{Hd}} \cdot \nabla \varepsilon)$ with dispersion coefficient $\mathcal{D}_{\text{Hd}} = \mathcal{D} \frac{d_b u_{\text{St}}(1-\varepsilon)}{2}$. The expression for \mathcal{D}_{Hd} differs from the expression provided by Ref. [173] where the dispersion coefficient is multiplied by an additional factor ε . However, our expression is consistent with the experimentally observed hydrodynamic dispersion [191, 197] where the dispersion coefficient is proportional to $d_b u_{\text{St}}$. The dispersion coefficient used in the expression of \mathbf{u}_{Hd} is a consequence of the random path taken by the liquid in the presence of bubbles similar to hydrodynamic dispersion in a porous medium [199, 200] and is not the same as the turbulent eddy viscosity, which we have neglected in this work.

The fourth and the fifth terms, \mathbf{u}_{Sd} and \mathbf{u}_{Sm} , are results of increased bubble-bubble interactions in a sheared flow. This causes a dispersion of bubbles from regions of high gas fraction regions to low gas fraction region, called shear induced diffusion given by $\mathbf{u}_{\text{Sd}} = -\frac{d_b^2}{4} \left| \frac{\partial w}{\partial x} \right| \frac{\varepsilon(1+0.5e^{8.8\varepsilon})}{3(1-\varepsilon)} \nabla \varepsilon$ [201, 202], and from regions of high shear rate to regions of low shear rate, called shear induced migration given by $\mathbf{u}_{\text{Sm}} = -\text{sign} \frac{d_b^2}{4} \left(\frac{\partial w}{\partial x} \right) \frac{0.6\varepsilon}{1-\varepsilon} \nabla \frac{\partial w}{\partial x}$ [202]. All expressions of slip velocities assume that the liquid flow is primarily in the vertical direction. In regions where the flow is not vertical, the slip velocity expressions should be modified. However, as shown later in Fig. 4.3, we see that for the present configuration, the flow is primarily in the vertical direction. The validity of these expressions for high current density where these bubble-bubble interactions are significant is further established by comparison with four-way coupled DNS simulations for laminar flows in Ref. [203].

For water electrolysis, producing one mole of hydrogen at the cathode involves transfer of two moles of electrons, while producing one mole of oxygen at the anode involves transfer of four moles of electrons. The volumetric flux, or superficial gas velocity U_g of the electrogenerated gas in the x -direction can be directly related to the applied current density using the Faraday's law as:

$$U_{g,c} = \frac{\mathcal{V}_m}{2F} j, \quad \text{and} \quad U_{g,a} = -\frac{\mathcal{V}_m}{4F} j, \quad (4.5)$$

where \mathcal{V}_m is the molar volume of the gas. For an ideal gas, $\mathcal{V}_m = RT/p$ where R is the universal gas constant. For simplicity, we assume a 100% gas evolution efficiency [204]. It should be noted that increasing the pressure of the system, decreases the molar volume of the gas, thereby reducing the gas flux. Moreover, as the pressure increases, the gas evolution efficiency may decrease, further lowering the volumetric flux in Eq. (4.5).

4.3. ANALYTICAL MODEL

In this section, we find an approximate analytical solution for Eq. (4.2) and derive expressions for the velocity profile, average superficial velocity, and pressure drop along the height of the electrode. We will also highlight the assumptions and limits of the analytical solution.

4.3.1. VOLUME FRACTION

We assume that the gas fraction in the interelectrode gap can be written as

$$\varepsilon = \varepsilon_0 \left(e^{-\frac{x}{\delta_g}} + e^{-\frac{l-x}{\delta_g}} \right), \quad (4.6)$$

where ε_0 is the gas fraction at the electrode surface and δ_g is the e-folding plume thickness. Here, we assume equal gas fraction at both electrodes, but treat a more general case of different gas fractions in 4.A. We also assume that the plume thickness is equal on the cathode and the anode side. This is approximately valid as long as the diameter of the oxygen and the hydrogen are similar. We provide a general solution for different plume thicknesses in 4.B. Using Eq. (4.6), the average gas fraction in the electrode gap can be written as

$$\langle \varepsilon \rangle = \frac{2\varepsilon_0\delta_g \left(1 - e^{-\frac{l}{\delta_g}} \right)}{l}, \quad (4.7)$$

which gives $\langle \varepsilon \rangle = \frac{2\varepsilon_0\delta_g}{l}$ for $\delta_g \ll l$ and $\langle \varepsilon \rangle = 2\varepsilon_0$ for $\delta_g \gg l$.

4.3.2. PLUME THICKNESS

We assume that the plume thickness can be written as

$$\delta_g = \frac{\mathcal{A}z^a}{\langle W \rangle^b}, \quad (4.8)$$

where \mathcal{A} is a dimensional constant depending on the current density, electrolyte, and the electrode. Schillings et al. [172] conducted an analytical scaling study for natural recirculation when the bubble diffusion coefficient is much smaller than the liquid kinetic viscosity so that bubble diffusion is smaller than momentum diffusion, to give

$\delta_g \sim \left(\frac{\rho g z d_b^6}{\mu l U_g} \right)^{1/4}$. At high current density, shear-induced diffusion becomes dominant, and the plume thickness is predicted to be given by $\delta_g \sim (d_b^2 z)^{1/3}$ [172]. Schillings et al. [172] also showed analytically that for a forced flow, $b = 1/3$. Reference [205] analyzed the existing experimental data of Refs. [206], [207], and [168] and showed that at low current density and heights, $a \approx 0.5$. Bongenaar-Schlechter et al. [208] found from both theory and experiments that $a \approx 0.3$ and $b \approx 1/3$ under forced flow conditions. Fukunaka et al. [209] found that the bubble layer grows along the vertical height with $a \approx 0.33$ for current densities ranging from 200 A/m² to 1000 A/m², while $a \approx 0.4$ for 100 A/m². Lee et al. [170] experimentally observed in a forced flow that b ranges from 0.3 to 0.7. Pang et al. [165] made use of high speed videography and fitted the plume thickness for the region above the electrode with $a = b = 0.47$.

4.3.3. GOVERNING EQUATION AND BOUNDARY CONDITIONS

We assume that inertial forces are negligible in comparison to the sum of pressure forces and buoyancy. It should be noted that for natural recirculation, this assumption may not hold everywhere, especially in the core region where little or no gas is present. Therefore, in such cases, we expect a deviation from the numerical solution. Neglecting the inertial term in the z -component of the momentum equation from Eq. (4.2), we can write

$$0 = -\frac{\partial P}{\partial z} + \frac{\partial}{\partial x} \left(\mu_m \frac{\partial w}{\partial x} \right) + \varepsilon \rho g, \quad (4.9)$$

where $P = p + \rho g z$ is the reduced pressure and ε is given by Eq. (4.6). We used here the limit $\rho_g \ll \rho$, for which $\rho_m = \rho(1 - \varepsilon)$. We also assumed that $w_s \ll w$ for small bubbles, that allows us to write $W_m = w + \varepsilon w_s \approx w$. We now introduce the following dimensionless and characteristic variables:

$$\bar{\delta} = \frac{\delta_g}{l}, \quad \bar{x} = \frac{x}{l}, \quad w_p = -\frac{\partial P}{\partial z} \frac{l^2}{12\mu} \quad \text{and} \quad w_b = \frac{\rho g l^2}{12\mu}, \quad (4.10)$$

and re-write Eq. (4.9) as

$$0 = 12w_p + \frac{\partial}{\partial \bar{x}} \left(\mu_r \frac{\partial w}{\partial \bar{x}} \right) + 12w_b \varepsilon = 0. \quad (4.11)$$

To solve Eq. (4.11), we need two boundary conditions which can be obtained from the no-slip condition for the liquid electrolyte at the electrode surface so that $w = 0$ at $\bar{x} = 0$ and $\bar{x} = 1$.

4.3.4. ELECTROLYTE VELOCITY

In the below analysis, we assume $\mu_r = \frac{\mu_m}{\mu} = 1$ to obtain more transparent equations, but provide a more generally valid case of $\mu_r = \frac{1}{1-\varepsilon}$ in 4.A.

INTERSTITIAL VELOCITY PROFILE

Solving Eq. 4.11 with Eq. (4.6), no-slip boundary conditions and assuming $\mu_m = \mu$, we get

$$w = 6w_p \bar{x}(1 - \bar{x}) + 12w_b \varepsilon_0 \bar{\delta}^2 \left(1 - e^{-\frac{\bar{x}}{\bar{\delta}}} \right) \left(1 - e^{-\frac{1-\bar{x}}{\bar{\delta}}} \right). \quad (4.12)$$

The first term is the common pressure driven parabolic profile. For large $\bar{\delta} \gg 1$, Eq. (4.12) tends to $(6w_p + 12w_b \varepsilon_0) \bar{x}(1 - \bar{x})$ so that buoyancy assists the pressure gradient in driving the parabolic flow profile. For thin plumes, in the limit of $\bar{\delta} \ll 1$, the second term describes a plug flow with a constant velocity in the center, decreasing to zero in very thin boundary layers near $\bar{x} = 0$ and $\bar{x} = 1$. In this limit, it can be approximated by $12w_b \varepsilon_0 \bar{\delta}^2 \left(1 - \frac{\cosh((2\bar{x}-1)/2\bar{\delta})}{\cosh(1/2\bar{\delta})} \right)$ similar to the analytical solution for Hartmann flow in a magnetic field [210, 211] and the Darcy-Brinkman equation for flow in a porous medium, where δ_g is the square root of the ratio of permeability and porosity [212].

AVERAGE SUPERFICIAL VELOCITY

The average superficial velocity, $\langle W \rangle = \int_0^1 w(1 - \varepsilon) d\bar{x}$ using Eq. (4.12) gives

$$\begin{aligned} \langle W \rangle &= w_p + 12\varepsilon_0 \bar{\delta}^2 (w_b - w_p) \left(1 - 2\bar{\delta} + (1 + 2\bar{\delta}) e^{-\frac{1}{\bar{\delta}}} \right) \\ &\quad - 12\varepsilon_0^2 \bar{\delta}^2 w_b \left(\bar{\delta} - 2e^{-\frac{1}{\bar{\delta}}} - \bar{\delta} e^{-\frac{2}{\bar{\delta}}} \right) \end{aligned} \quad (4.13)$$

For thin plumes ($\varepsilon_0 \bar{\delta} \ll 1$ and $e^{-1/\bar{\delta}} \ll 1$) with respect to interelectrode gap, Eq. (4.13) can be written as

$$\langle W \rangle = w_p + 12 w_b \varepsilon_0 \bar{\delta}^2 (1 - 2\bar{\delta}), \quad \begin{cases} w_b \gg w_p \text{ or} \\ 12 \varepsilon_0 \bar{\delta}^2 \ll 1 \end{cases} \quad (4.14)$$

In the limit of zero gas fraction, $\varepsilon_0 \rightarrow 0$, Eq. (4.14) reduces to the single phase Hagen–Poiseuille relation, $\langle W \rangle = w_p$. For the homogeneous limit ($\bar{\delta} \gg 1$), the gas fraction uniformly becomes $2\varepsilon_0$ and Eq. (4.13) gives

$$\langle u \rangle = \frac{\langle W \rangle}{1 - 2\varepsilon_0} = w_p + 2\varepsilon_0 w_b, \quad (4.15)$$

where $\langle u \rangle$ is the interstitial electrolyte velocity. Equation (4.15) clearly shows buoyancy assisting pressure driven flow and the effect of the liquid fraction through $1 - 2\varepsilon_0$.

4.3.5. ELECTRODE SURFACE GAS FRACTION

The gas fraction at the electrode surface, ε_0 , is hard to measure experimentally but is an important quantity. In this section, we provide an analytical model to estimate it. The average superficial gas velocity $\langle W_{g,c} \rangle$ due to gas generated at the cathode is related to the superficial gas velocity $U_{g,c}$ in the x -direction by the continuity equation as

$$\langle W_{g,c} \rangle = \int_0^z U_{g,c} dz / l = \frac{j V_m z}{2Fl}, \quad (4.16)$$

where in the final expression, we assumed a constant current density j . The interstitial liquid velocity is related to superficial gas velocity $\langle W_{g,c} \rangle$ as

$$\langle W_{g,c} \rangle = \langle \varepsilon_c (w + w_s) \rangle, \quad (4.17)$$

where w_s is the vertical component of the slip velocity. Usually, it can be neglected. However, we provide the expressions for electrode surface gas fraction assuming a constant slip velocity. It should be noted that while the approximate analytical results neglect the slip velocity, the numerical solution includes all the slip velocities mentioned in Eq. (4.4). A similar expression can be derived for the superficial gas velocity $\langle W_{g,a} \rangle$ at the anode. For $\bar{\delta} \gg 1$, we can rewrite Eq. (4.17) as

$$\langle W_{g,c} \rangle = 2 w_b \varepsilon_0^2 + (w_p + w_s) \varepsilon_0, \quad (4.18)$$

which on solving for ε_0 gives

$$\varepsilon_0 = \frac{\varepsilon_h^2}{2\varepsilon_l} \left(\sqrt{1 + \left(\frac{2\varepsilon_l}{\varepsilon_h} \right)^2} - 1 \right), \quad (4.19)$$

with $\varepsilon_l = \frac{\langle W_{g,c} \rangle}{w_p + w_s}$ and $\varepsilon_h = \sqrt{\frac{\langle W_{g,c} \rangle}{2w_b}}$, where ε_l and ε_h are the limiting expressions for ε_0 for low and high values, respectively. Equation (4.19) can also be approximated by $\varepsilon_0 \approx (\varepsilon_l^p + \varepsilon_h^p)^{1/p}$ with a relative maximum error of less than 4% for $p = -1.43$ or about 20% for $p = -1$. This form manifestly shows that it is the smaller one of ε_l and ε_h that primarily

determines ε_0 . Using Eq. (4.12), we can rewrite Eq. (4.17) for thin plumes ($e^{-1/\bar{\delta}} \ll 1$) with respect to interelectrode gap and small reduced pressure gradient as

$$\langle W_{g,c} \rangle = 6\bar{\delta}^3 w_b \varepsilon_0^2 + (6\bar{\delta} w_p (1 - 2\bar{\delta}) + w_s) \bar{\delta} \varepsilon_0, \quad (4.20)$$

and solve Eq. (4.20) using Eq. (4.14) for ε_0 to give Eq. (4.19), now with

$$\varepsilon_l = \frac{\langle W_{g,c} \rangle}{\bar{\delta} (6\bar{\delta} \langle W \rangle (1 - 2\bar{\delta}) + w_s)}, \quad \varepsilon_h = \sqrt{\frac{\langle W_{g,c} \rangle}{6 w_b \bar{\delta}^3 (1 - 12\bar{\delta} (1 - 2\bar{\delta})^2)}}. \quad (4.21)$$

There are very few wall gas fraction measurements. Reference [209] calculated the gas fraction using image analysis and Eq. (4.17) for low current density and low height to give $\varepsilon_0 \propto j^{1/2}$ and $\delta_g \propto j^{0.26}$. At low current densities and low heights, it is expected that ε_l dominates. We note that $\langle W_{g,c} \rangle$ varies linearly with current density as given by Eq. (4.16). Using $\delta_g \propto j^{0.26}$ in the expression for ε_l and neglecting the slip velocity in Eq. (4.21) gives $\varepsilon_0 \propto j^{0.48}$ similar to Ref. [209].

For higher heights, $\varepsilon_0 \approx \varepsilon_h$. Reference [209] measures the average gas fraction in a bubble dispersion layer, proportional to our ε_0 , to scale as $z^{0.26}$ and the plume thickness as $z^{0.31}$ for current densities above 93 A/m². We approximate $(1 - 12\bar{\delta}(1 - 2\bar{\delta})^2) \approx 6.5 \times 10^{-3} \bar{\delta}^{-1.5}$ as a power law in Eq. (4.21) for $0.06 < \bar{\delta} < 0.15$, so that with $\delta_g \propto z^{0.31}$, ε_0 becomes proportional to $z^{0.27}$ very close to the scaling of gas fraction found by Ref. [209].

4.3.6. PRESSURE DROP

As argued at the end of the previous section, often the wall gas fraction tends to be fairly constant beyond a certain height. Assuming a constant ε_0 , we can write the total pressure drop across the electrode height, $\Delta P \equiv P(h) - P(0) = -\frac{12\mu}{l^2} \int_0^h w_p dz$ by inserting w_p from Eq. (4.14) and $\bar{\delta} = \mathcal{A} z^a / \langle W \rangle^b l$ as

$$\Delta P = -\frac{12\mu h \langle W \rangle}{l^2} \left(1 - \left(\frac{\langle W \rangle_{nc}}{\langle W \rangle} \right)^{1+2b} \left(1 - 2\bar{\delta}_h \frac{2a+1}{3a+1} \right) \right), \quad (4.22)$$

where $\bar{\delta}_h = \bar{\delta}|_{z=h}$. In the limit, $\varepsilon_0 \rightarrow 0$, Eq. (4.22) reduces again to the familiar Hagen-Poiseuille relation. The negative sign in front of $\langle W \rangle_{nc}$ shows that buoyancy opposes the pressure drop due to viscous friction. The velocity obtained for $\Delta P = 0$ in the limit $\bar{\delta} \ll 1$ is given by $\langle W \rangle = \langle W \rangle_{nc}$ where

$$\langle W \rangle_{nc} = \left(\frac{12 w_b \varepsilon_0}{1 + 2a} \left(\frac{\mathcal{A} h^a}{l} \right)^2 \right)^{\frac{1}{1+2b}} \quad (4.23)$$

The subscript 'nc' stands for natural convection. Here, $\langle W \rangle_{nc}$ is the expected superficial velocity in case friction can be neglected for the natural convection flow. This may be a good approximation in the case of electrodes immersed in a large container.

Eq. (4.23) gives the upper limit for natural convection velocity because at high velocity, the dynamic pressure losses can not be neglected so that $\Delta P > 0$. Eq. (4.23) gives $\langle W \rangle_{nc} \propto l^{-0.6}$ for $b = 1/3$ as both ε_l and ε_h are proportional to l when velocity slip can be neglected. A similar dependence of recirculation velocity on gap width, $l^{-0.5} - l^{-0.65}$ is reported in Reference [213]. We will use Eq. (4.23) in section 4.5 to calculate the maximum height for a buoyancy driven electrolyzer.

4.3.7. WALL SHEAR STRESS

Assuming a constant ϵ_0 , we can integrate Eq. (4.11) for thin plumes over the interelectrode gap to give the total shear stress at a particular height z as

$$\tau_w = 2\mu \left. \frac{\partial w}{\partial x} \right|_{x=0} = \frac{12\mu}{l} (w_p + 2w_b \epsilon_0 \bar{\delta}). \quad (4.24)$$

For single phase flow, the shear stress is given by $\tau_0 = 12\mu\langle W \rangle/l$. Therefore, we can write the ratio of the multiphase shear stress and single phase shear stress using Eq. (4.14) and Eq. (4.24) as

$$\frac{\tau_w}{\tau_0} = 1 + \frac{w_b \epsilon_0 \bar{\delta} (2 - 12\bar{\delta}(1 - 2\bar{\delta}))}{\langle W \rangle}. \quad (4.25)$$

For thick plumes, integrating Eq. (4.11) gives the ratio $\frac{\tau_w}{\tau_0} = \frac{1}{1-2\epsilon_0}$. Here, $1 - 2\epsilon_0$ is the correction for increased interstitial velocity in the presence of average gas fraction $2\epsilon_0$. Various authors have previously studied the pressure drop or shear stress multiplier, defined as the ratio of multiphase shear stress to single phase shear stress [214–218]. Equation (4.25) shows that for forced flow assisting buoyancy, considered here, the multiphase shear stress is always larger than the single phase shear stress and at constant superficial liquid velocity. The multiphase shear stress increases as the average gas fraction increases, but decreases as the plume thickness increases. It should be noted that the wall shear stress in Eq. (4.24) and Eq. (4.25) varies with height z .

4.4. VALIDATION AND DISCUSSIONS

In the first part of this section, we compare our numerical model with two different experimental measurements: one under forced flow conditions by Pang et al. [165] and another under bubble-induced free convection by Boissonneau [118]. Pang et al. [165] estimated the gas fraction from images in the region above the electrodes, while Boissonneau [118] measured the velocity profiles in the inter-electrode gap of a small electrolyzer using laser doppler velocimetry (LDV). The dimensions and operating conditions for the experiments are listed in Table 4.1. In the second part of this section, we validate our analytical expressions for the surface gas fraction and velocity profile. In the third part, we verify the analytical pressure drop relation of Eq. (4.22) against the numerical simulations.

4.4.1. VALIDATION OF NUMERICAL MODEL

We solved the mixture model formulation in COMSOL v5.6, as described in section 4.2.2. At the top, an outlet boundary condition is used with a pressure of 0 Pa so that both the gas and the liquid can flow out of the domain. A parabolic velocity inlet boundary condition is used at the bottom of the channel with zero gas flux such that the average velocity just below the electrode matches the average velocity measured in the experiments, as shown in Fig. 4.2. This means that the flow enters the electrode as fully developed, which may not be true if the velocity is high. However, for the conditions of Ref. [118], $h_{en} = 40$ mm is approximately equal to the entrance length for a laminar flow [219], $(0.625 + 0.044\text{Re})l \approx 34$ mm, at the maximum velocity $\langle W \rangle = 0.08$ m/s observed at 2000 A/m². Therefore, we can expect the flow to be parabolic at the bottom of the electrode

Table 4.1: Dimensions and operating conditions for validation cases

Properties	Pang et al. [165]	Boissonneau [118]
Electrode	2 nm Ti and 50 nm Pt deposited sequentially on Ti foil substrate	coated Titanium at Cathode and DSA [®] at Anode
Electrolyte	0.5 M H ₂ SO ₄	50 g/l Na ₂ SO ₄ (or 0.35 M)
Inter-electrode gap, l	4 mm	3 mm
Electrode height, h	9 mm	40 mm
Channel height above electrode, h_{exit}	12 mm	40 mm
Channel height below electrode, h_{en}	95 mm	40 mm
Temperature, T	60° C	25° C
Pressure	1 atm	1 atm
Electrolyte density, ρ	1030 kg/m ³	1040 kg/m ³
Electrolyte viscosity, μ	1.1 mPa-s	1.03 mPa-s

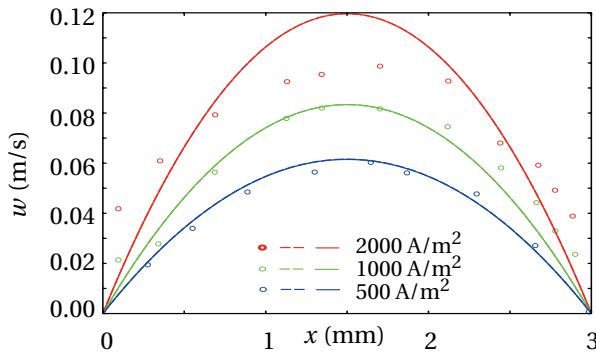


Figure 4.2: Velocity profiles at $z = -5$ mm slightly below the electrode (see Fig. 4.1), for the three current densities: $j = 2000$ A/m² (red), $j = 1000$ A/m² (green) and $j = 500$ A/m² (blue). The circles represent the experimental measurements from Boissonneau [118], the dashed line represents the numerical solution and the almost overlapping solid line represents the approximate analytical solution of Eq. (4.33). The parameters used are listed in Table 4.1, Table 4.2 and Table 4.3 for buoyancy driven conditions. Eq. (4.33) gives a parabola when $\epsilon_0 = 0$.

for the conditions of Ref. [118]. At the electrode wall, we used the mixture inlet boundary condition, where we provided the mixture and the gas velocity to be equal and given by Eq. (4.5). This boundary condition ensures that the gas enters from the electrodes at a superficial velocity given by Eq. (4.5). In our simulations, we use a constant bubble diameter at a given current density, see Table 4.2. Boissonneau [118] measured up to two times larger average hydrogen bubble diameter at the top compared to the bottom of the electrode. We used the average bubble diameter measured at the top of the electrode, as listed in Table 4.2. The bubble diameter is assumed to be the same for both hydrogen

Table 4.2: Average hydrogen bubble diameter measured experimentally at the top of the electrode for different validation cases. The Reynolds number is defined as $Re = \rho u l / \mu$.

Validation Case	d_b [μm]	$\langle W \rangle_{in}$ [m/s]
Forced Flow (Pang et al. [165])		
$j = 2000 \text{ A/m}^2$, $Re = 297$	157	0.08
$j = 2000 \text{ A/m}^2$, $Re = 796$	150	0.214
Natural Recirculation (Boissonneau [118])		
$j = 500 \text{ A/m}^2$	62	0.041
$j = 1000 \text{ A/m}^2$	74	0.056
$j = 2000 \text{ A/m}^2$	87	0.08

and oxygen, as no information about the size of oxygen bubbles was provided in the two references.

Figure 4.3 shows the liquid velocity vector overlaid on the contour plot of gas fraction. We see that the gas moves in a plume near the electrode surface and the gas fraction increases along the height of the electrode. The liquid velocity is initially parabolic at the bottom of the electrode, but changes its shape due to buoyancy of the bubbles.

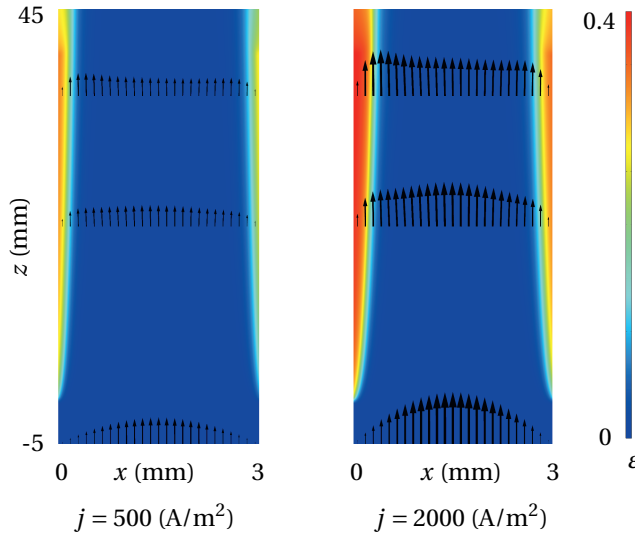
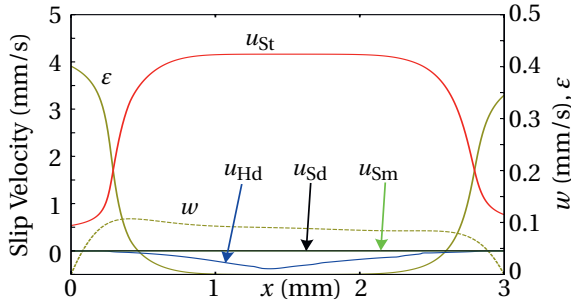


Figure 4.3: Liquid velocity vectors overlaid on contour plots for gas fraction. The size of the arrow vector represents the magnitude of the velocity. The parameters used are listed in Table 4.1, Table 4.2 and Table 4.3 for buoyancy driven conditions. The velocity vectors are shown at $z = -5 \text{ mm}$, $z = 20 \text{ mm}$ and $z = 35 \text{ mm}$. It can be seen that the velocity is initially parabolic as shown in Fig. 4.2, but changes its shape along the vertical coordinate as the gas fraction increases.

Figure 4.4 shows the magnitude of slip velocity near the top of the electrode ($z = 35 \text{ mm}$) for the validation case solved in COMSOL corresponding to the experiments of Boissonneau [118] at 2000 A/m^2 . The properties are listed in Table 4.1 and Table 4.2.

It can be seen that the slip velocity due to hydrodynamic dispersion, Saffman force and shear-induced diffusion are important, while shear migration can be neglected both in horizontal and vertical direction. The hydrodynamic dispersion becomes important in the region where the gas fraction is small. This is because the hindrance factor $f(\varepsilon)$ reduces its magnitude in the region of high gas fraction. The slip velocity due to Saffman force and shear-induced diffusion is significant near the electrodes due to high shear rate in these regions.

(a) Vertical slip velocities at $z = 35$ mm



(b) Horizontal slip velocities at $z = 35$ mm

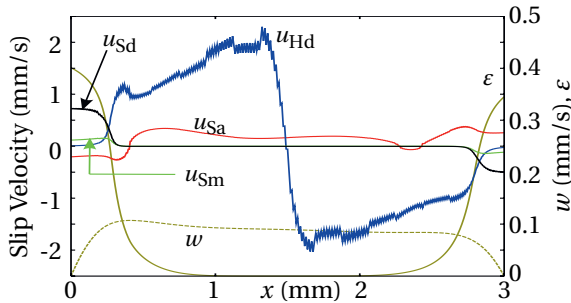


Figure 4.4: Magnitude of slip velocity near the top of the electrode ($z = 35$ mm) for the validation case corresponding to the experiments of Boissonneau [118] at 2000 A/m^2 . The top figure shows the vertical slip velocities. It can be seen that in the vertical direction, the Stokes slip velocity due to buoyancy is dominant, while the shear migration and shear diffusion slip velocities are negligible. In the horizontal direction, the shear migration slip velocity is always negligible compared to other slip velocities. The slip velocities due to Saffman force and shear-induced diffusion are dominant near the wall, while hydrodynamic dispersion becomes important in the bulk region where the gas fraction gradient is large and gas fraction is small.

PLUME THICKNESS

Here, we compare the plume thickness along the height h_{exit} above the electrode with the experimental data from Pang et al. [165]. Figure 4.5 shows the contour lines corresponding to the location where 99% and 60% of the gas is located inside the plume for the two different Reynolds numbers. We see a good agreement between the numerical model and the experimental measurements. The analytical expression of Eq. (4.8) is also shown in Fig. 4.5.

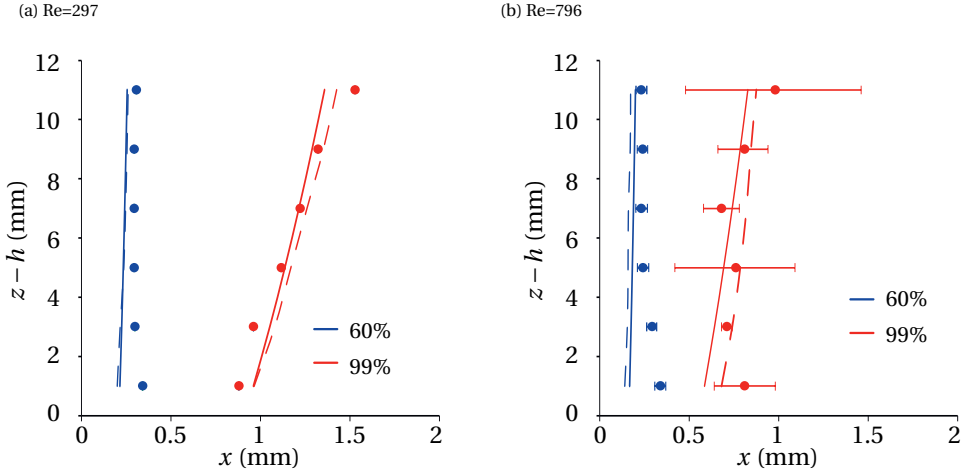


Figure 4.5: Contour lines corresponding to the locations where 60% and 99% of the hydrogen gas is located within the plume. The circles with error bars represent the experimental measurements from Pang et al. [165] and the dashed line represents our numerical solution. The solid line represents the profile using Eq. (4.8) with $a = 0.5$, $b = 0.33$ and $\mathcal{A} = 8.4 \times 10^{-4} \text{ m}^{0.83} / \text{s}^{0.33}$ for the 60% profile. For the 99% profile, we used $\mathcal{A} = 2.1 \times 10^{-3} \text{ m}^{0.83} / \text{s}^{0.33}$.

Table 4.3: Estimated parameters for plume thickness using a least square fit on simulation results for the configuration used by Boissonneau [118]. While the electrolyzer used in Ref. [118] operates using buoyancy driven flow, the forced flow results are obtained by doing multiple numerical simulations with different inlet velocities. The power of $b = 1/3$ is also observed by Schillings et al. [172].

At buoyancy-driven conditions [118]			
j (A/m ²)	a	$\mathcal{A} / \langle W \rangle^b$	
500	0.35	6.6×10^{-4}	
1000	0.39	9.2×10^{-4}	
2000	0.4	1.2×10^{-3}	
Forced flow (simulations)			
j (A/m ²)	a	b	\mathcal{A}
500	0.44	0.33	3.4×10^{-4}
1000	0.45	0.33	5×10^{-4}
2000	0.45	0.32	6.9×10^{-4}

In order to find the most suitable values of \mathcal{A} , a , and b , we did multiple simulations for the configuration used by Boissonneau [118] for current densities of 500 A/m², 1000 A/m² and 2000 A/m² at different forced flow conditions such that $\langle W \rangle$ ranges between 0.06 m/s and 0.33 m/s. Using the data from the simulations, we obtained the e-folding plume thickness δ_g at every 1 mm between $h = 0$ mm and $h = 40$ mm by fitting Eq. (4.6) such that the average gas fraction $\langle \varepsilon \rangle$ and the electrode gas fraction ε_0 are the same as in the numerical solution. Using this plume thickness data, we performed regression using the least squares method to obtain the values of \mathcal{A} , a and b reported in Table 4.3. It can be seen from Fig. 4.7 that the estimated parameter values give a reasonable fit for

the simulated plume thickness. We also note from Table 4.3 that \mathcal{A} varies with current density. Since, in our model, current density is proportional to volumetric flux $U_{g,c}$ from Eq. (4.5), we write, for forced flow

$$\mathcal{A} \approx 4.4 \times 10^{-2} U_{g,c}^{0.5}, \quad (4.26)$$

as shown in Fig. 4.6. Eq. (4.26) should be used with caution, as it is obtained for forced flow conditions and for bubble diameter varying with current density for only three data points. The effect of increased bubble diameter is also included implicitly in Eq. (4.26). Reference [165] also predicted a similar power of $j^{0.47}$ for forced flow conditions, however Ref. [208] predicted a much smaller power of $j^{0.1}$.

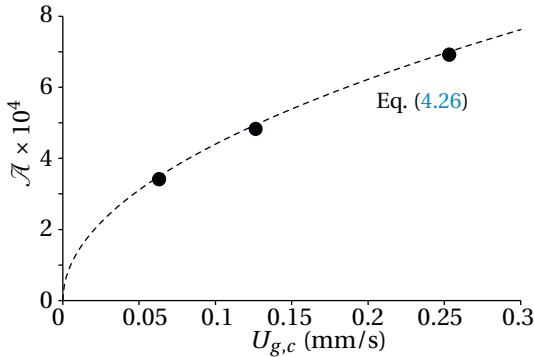


Figure 4.6: Variation of \mathcal{A} with volumetric gas flux in horizontal direction $U_{g,c}$ for forced flow simulations corresponding to the configuration used by Boissonneau [118]. We see that \mathcal{A} , shown as solid circles, varies roughly as the square root of volumetric flux given by Eq. (4.26) for these simulations. It should be noted that the current density is proportional to volumetric flux according to Eq. (4.5).

In our simulations, we used the bubble sizes in Table 4.2, independent of velocity. Higher velocities result in smaller bubbles [165, 220, 221]. In addition to the direct effect of flow on the plume width, this further reduces the plume thickness. This is because a decrease in bubble size results in smaller lateral dispersion of bubbles as the slip velocities in the lateral direction are proportional to d_b , see Eq. (4.4). As such, the numerically obtained value of b may be overestimated. Referring to Fig. 4.9, we note that the plumes are not exactly exponential, especially at higher heights and current densities. Therefore, we expect deviations from our analytical model, particularly for these conditions.

VELOCITY PROFILE

In Fig. 4.10, we compare the velocity profiles from the numerical model against the experiments from Boissonneau [118] at different electrode heights and current densities. The model shows good agreement with the experimental data. The simplification of assuming a constant diameter in the numerical model is the likely reason for small discrepancies. It should be noted that the measured velocities in Fig. 4.10 are always higher than the velocities from the numerical and semi-analytical model. In part, this is because laser doppler velocimetry measures the bubble velocity, which is always slightly

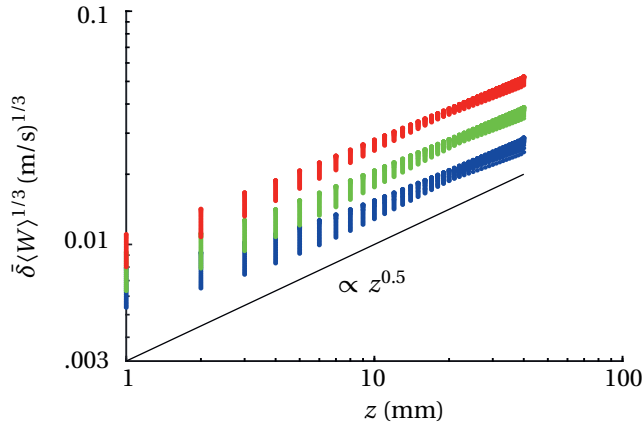


Figure 4.7: Scatter plot for simulated e-folding plume thickness δ_g for different heights, inlet velocities and current densities for the configuration of Boissonneau [118] and corresponding properties listed in Table 4.1. The plot contains data from 40 different heights ranging from 1 mm to 40 mm at different forced flow conditions, such that $\langle W \rangle$ ranges between 0.06 m/s and 0.33 m/s. The blue, green and red dots corresponds to $j = 500$ A/m², $j = 1000$ A/m² and $j = 2000$ A/m², respectively. It can be seen that the plume thickness can be approximated reasonably well with $\frac{\mathcal{A}z^a}{\langle W \rangle^b}$ over this range of parameters where \mathcal{A} , a and b are listed in Table 4.3.

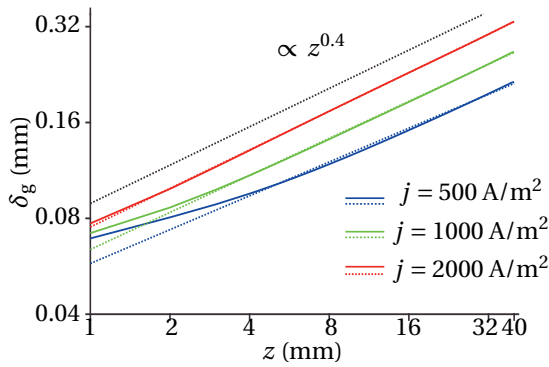


Figure 4.8: Log-log plot for e-folding plume thickness δ_g with height z obtained from our numerical model for the buoyancy driven flow in the configuration used by Boissonneau [118]. The colored dotted lines represent the power law relation fitted using regression with parameters listed in Table 4.3. The black dotted line indicates a slope of 0.4. It can be seen that at low values of δ_g , the power law underestimates the plume thickness.

higher than the liquid velocity due to slip. For a bubble diameter of $88 \mu\text{m}$, we can estimate w_{st} to be approximately 4 mm/s. The oxygen bubbles may be larger, giving larger slip velocities – see 4.D.

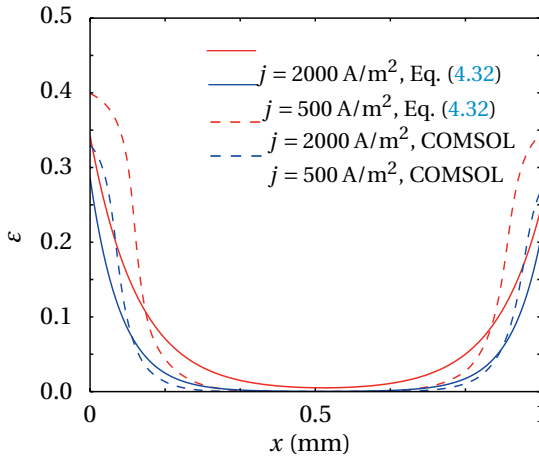


Figure 4.9: Gas fraction profiles for the configuration used by Boissonneau [118]. It can be seen that at low current density, the gas fraction varies approximately exponentially with x while at larger current densities, the gas fraction profiles are not exponential. Due to this, the estimated e-folding plume thickness using the procedure described in section 4.3.2 overestimates the growth of plume thickness with height. This deviation from an exponential profile will result in errors at higher heights and larger current densities.

4.4.2. VALIDATION OF ANALYTICAL MODEL

GAS FRACTION AT THE ELECTRODE

For the experimental values of $\langle W \rangle$ from Boissonneau [118], we solve Eq. (4.35) and Eq. (4.39) numerically to get the gas fraction ε_0 and w_p at a certain height. Since different amount of gas is generated at the cathode and the anode as described by Eq. (4.5), we use $Q = 0.8$. In Fig. 4.11, we compare the analytical approximation for ε_0 with that of the numerical model. We see that the analytical model gives a similar trend for the gas fraction at the electrode surface as the numerical model. Compared to the numerical model, the analytical gas fraction is lower, especially at larger heights. This is because we neglected the effect of inertial terms in our analysis. As such, the analytical profiles have a larger peak velocity (see Fig. 4.10). From Eq. (4.17), this gives a lower gas fraction.

VELOCITY PROFILE

For calculating the velocity profile, we use the just obtained semi-analytical values of ε_0 and w_p at a particular height to plot the velocity profile in Fig. 4.10 using Eq. (4.33). Here, we used the relations from the appendix to reproduce asymmetric profiles due to different wall gas fractions at the two electrodes. We see a reasonable agreement of the semi-analytical model with the numerical model and experimental measurements. The analytical results do not show the small velocity peak in the center of the channel that is visible from simulations at $z = 20$ mm and $j = 1000$ A/m² and $j = 2000$ A/m². The analytical results also show a higher velocity peak near the electrode surface. The discrepancy arises because we neglected the inertial term, which lowers the velocity near the peak and increase the velocity in the bulk. At higher current densities, the deviation

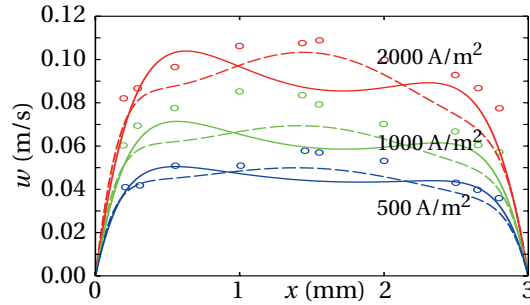
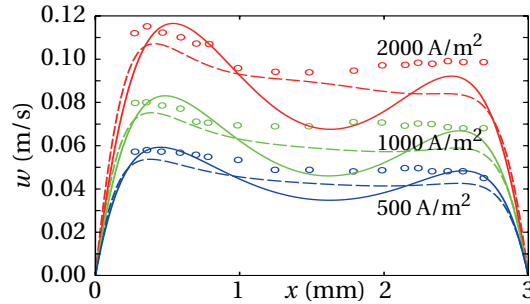
(a) $z = 20$ mm(b) $z = 35$ mm

Figure 4.10: Velocity profiles for the three current densities: $j = 500$ A/m² (blue), $j = 1000$ A/m² (green), and $j = 2000$ A/m² (red). The circles represent the experimental measurements from Boissonneau [118], the dashed line represents the numerical solution and the solid line represents the semi-analytical solution. Here, we used Eq. (4.33) to capture the asymmetry for water electrolysis. For the values of δ_g , we used parameters in Fig. 4.8. It should be noted that the experimental velocity profiles are measured using laser Doppler velocimetry, and hence represent bubble velocities. The liquid velocities are slightly lower than the bubble velocities due to the slip velocity.

from the numerical model is larger because our assumption of thin exponential plumes no longer holds.

PRESSURE DIFFERENCE

Due to lack of experimental data, we rely on our validated numerical simulations to verify Eq. (4.22) for the pressure drop along the electrode height. We used the configuration from Boissonneau [118] and carried out various numerical simulations under forced flow conditions for $j = 1000$ A/m² by varying the inlet velocities. Figure 4.12 shows the variation of the reduced pressure difference, ΔP with the superficial velocity, $\langle W \rangle$. The analytical pressure drop shows a reasonable agreement with the numerical results. At low velocities, the presence of gas makes the reduced pressure drop positive, as the effect of buoyancy becomes larger than that of friction. At high velocity, the plumes become thinner, while the viscous forces are increased due to the modified viscosity $\frac{\mu}{1-\epsilon_0}$. Due to the localized buoyancy force in thin plumes, the total pressure drop is similar to that for a single phase flow. We neglected the inertial term in our model, which results in

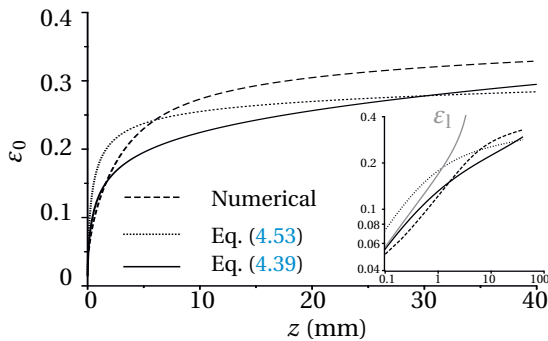
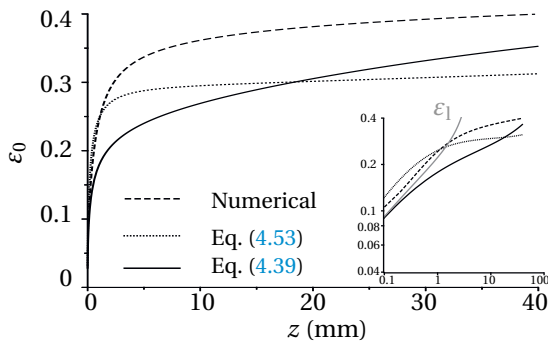
(a) $j = 500 \text{ A/m}^2$ (b) $j = 2000 \text{ A/m}^2$ 

Figure 4.11: Variation of gas fraction at the cathode surface, ε_0 with the vertical z -coordinate, z at different current densities. The solid line represents the semi-analytical solution of Eq. (4.39), the dotted line represents the semi-analytical solution for a constant gas fraction plume given by Eq. (4.53) using the values listed in Table 4.3 for the buoyancy driven conditions, and the dashed line represents the solution from the numerical model. We neglected the inertial term in our semi-analytical solution giving a larger peak velocity than that obtained using COMSOL as shown in Fig. 4.10. Because most of the gas is localized near the electrode surface, the larger velocity results in lower gas fraction according to mass conservation (see Eq. (4.17)). A log-log plot is shown in the inset. The solid gray line represents the solution for small gas fraction given by Eq. (4.40). From Eq. (4.40), $\varepsilon_1 \propto z^{1-2a}$, which gives $z^{0.3}$ for $j = 500 \text{ A/m}^2$ and $z^{0.2}$ for $j = 2000 \text{ A/m}^2$ using the value of 'a' at buoyancy driven conditions in Table 4.3.

large deviation, particularly, at high velocities. At low velocities, buoyancy is dominant and the error due to inertial terms is small. The deviation at low velocities is primarily because the plume thickness becomes large, and our assumption $\bar{\delta} \ll 1$ is only crudely satisfied.

4.5. DESIGN GUIDANCE

We can use our analytical model to guide the design of membraneless parallel plate electrolyzers. To avoid bubble crossover, thick plumes are not desired. Usually, at the top of the electrode, a divider to separate the gases would be present. For safe operation of

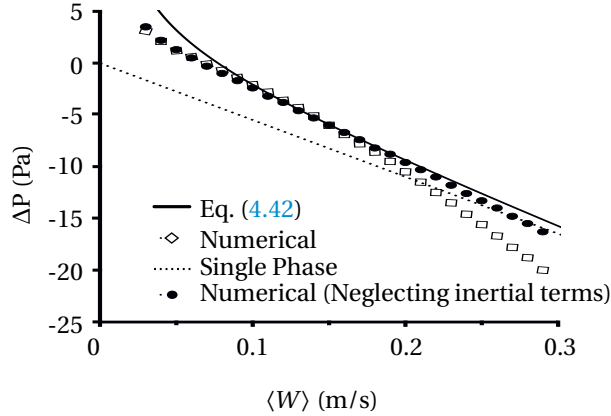


Figure 4.12: The predicted reduced pressure difference between the top and the bottom of the electrode plotted against the superficial velocity for $h = 40$ mm. The configuration used is similar to that used by Boissonneau [118], see Table 4.1. The hollow diamonds represent results from numerical simulations, the black dots represent the numerical solution neglecting the inertial terms, the solid black line represents the result from Eq. (4.42) and the dotted line represents the Hagen-Poiseuille pressure drop.

electrolyzer, the amount of H_2 in oxygen should not exceed the lower explosion limit of 4% in O_2 . Since twice as much hydrogen volume is produced compared to oxygen, this requires the cross-over rate of hydrogen to stay below 2%. We will assume that at least 98% of the gas fraction is contained between $x = 0$ and $x = l/2$,

$$\frac{\int_0^{l/2} \varepsilon_0 e^{-x/\delta_g} dx}{\int_0^l \varepsilon_0 e^{-x/\delta_g} dx} = \frac{1}{e^{-l/2\delta_g} + 1} > 0.98. \quad (4.27)$$

It would be more accurate to multiply the integrands with the gas velocity $u + w_s$. However, to obtain more transparent expressions, we here take this simpler approach. Solving for l gives

$$l \gtrsim 7.8\delta_h = 7.8 \frac{\mathcal{A} h^a}{\langle W \rangle^b}. \quad (4.28)$$

From Eq. (4.28), requiring the gap to be almost an order of magnitude larger than the plume thickness may seem like a very conservative criterion. However, mind that our δ_g is that distance after which the gas fraction has decreased to a fraction $1/e=0.37$ of its value at the electrode. Plume thickness decreases with an increase in vertical velocity of the electrolyte for a laminar flow. However, at large velocities, the flow may become turbulent leading to a thicker plume [165]. Therefore, the maximum velocity is limited by transition to turbulence. We can rearrange Eq. (4.28) using $\langle W \rangle = \frac{\text{Re}\mu}{\rho l}$, to give

$$h \lesssim \left(\frac{\langle W \rangle^b l}{7.8\mathcal{A}} \right)^{1/a} = \left(\frac{l^{1-b}}{7.8\mathcal{A}} \left(\frac{\text{Re}\mu}{\rho} \right)^b \right)^{1/a}. \quad (4.29)$$

Using Eq. (4.26) with properties from Table 4.1 and Table 4.3, corresponding to Ref. [118], we can express Eq. (4.29) as

$$h \lesssim 10.8 \frac{\langle W \rangle^{0.7} l^{2.2}}{U_{g,c}^{1.1}}. \quad (4.30)$$

We again note that the power 0.5 in Eq. (4.26) is obtained using forced flow simulations for the configuration used by Boissonneau [118], and a more detailed analysis of how the plume thickness varies with current density is warranted. Therefore, Eq. (4.30) should only be treated as an illustrative equation. Equation (4.29) and Eq. (4.30) shows that a larger interelectrode gap l allows a larger electrode height without significant gas crossover. However, this also increases the ohmic losses. Therefore, the maximum possible electrode height will be limited by the maximum allowable ohmic losses.

We also note that the maximum height increases with decrease in volumetric flux of the gas in the horizontal direction. In Fig. 4.13, we see that for a lower current density, the maximum height of the electrolyzer increases because a smaller current density corresponds to a lower horizontal volumetric flux of the gas. Similarly, a higher pressure decreases the molar volume of the gas, thereby decreasing the volumetric flux. As such, operation at higher pressure will give a larger maximum height for the electrolyzer.

In order to see whether parallel plate electrolyzers without separators can be a viable alternative to electrolyzers with separators, we provide design estimates so that the ohmic losses are lower than those of zero-gap electrolyzers with modern separators. The most commonly used Zirfon Perl diaphragm has a thickness of only 0.5 mm, but the ohmic losses are usually equivalent to 3.3 mm — 8 mm of KOH in a zero-gap configuration due to geometrical and gas effects [222, 223]. Therefore, we consider a membraneless parallel plate electrolyzer of 3 mm, giving lower ohmic losses than a zero-gap electrolyzer with Zirfon Perl separator. There will also be additional Ohmic loss due to bubble, but the multiplier ($\approx \int_0^1 (1 - \varepsilon)^{-3/2} d\bar{x}$) using Bruggeman's relation [153] will be close to 1 for thin plumes.

We first consider the design of the buoyancy driven electrolyzer used by Boissonneau [118]. Inserting $\langle W \rangle_{nc}$ from Eq. (4.43) in Eq. (4.28) gives

$$h_{\max} \approx \left(\frac{l}{\mathcal{A}} \left(\frac{6w_b \varepsilon_0 (2 - \varepsilon_0 + k_2/2)}{7.8^{\frac{1+2b}{b}} (1+2a) (1 + \frac{6\varepsilon_0 \bar{\delta}_{\max}}{1+a})} \right)^b \right)^{\frac{1}{a}}. \quad (4.31)$$

where $\bar{\delta}_{\max} \approx 1/7.8$ is the maximum allowable dimensionless plume thickness given by Eq. (4.27) and k_2 is defined in 4.A. For equal gas fraction at both electrodes, $k_2 = 0$. Using Eq. (4.31) and values from Table 4.3, we find that $h_{\max} \approx 13.6$ cm for $l = 3$ mm at 1000 A/m², assuming $\varepsilon_0 = 0.3$, and $h_{\max} \approx 7.5$ cm at 2000 A/m², assuming $\varepsilon_0 = 0.35$. These are the upper limits because Eq. (4.43) overpredicts the natural recirculation velocity. Friction in the external hydraulic circuit, including the downcomer is not taken into account. Also, at high velocities dynamic pressure losses will be important, and therefore the actual recirculation velocity will be smaller, giving a smaller height.

We can also increase the liquid velocity to increase the height of the electrolyzer as shown in Fig. 4.13. However, very high velocities can give rise to turbulence that enhances mixing, giving thicker plumes. This has been experimentally observed by Pang

et al. [165] where turbulence starts increasing the plume thickness at a Reynolds number, $Re \gtrsim 1200$. At $Re = 1000$, Eq. 4.29, using the values in Table 4.3 from Boissonneau [118], gives the maximum electrode height h_{\max} without significant crossover as 24.8 cm and 12.4 cm for a current density of 1000 A/m^2 and 2000 A/m^2 , respectively. This shows that using forced flow, the electrode height can be increased by more than two times.

For the electrode used by Pang et al. [165], the fit of Fig. 4.5 gives for $j = 2000 \text{ A/cm}^2$, a slightly larger plume thickness than in the configuration used by Boissonneau [118]. This may be attributed to the larger bubble size in the experiments by Pang et al. [165] ($\sim 150 \mu\text{m}$) compared to those in the experiments of Boissonneau [118] ($\sim 88 \mu\text{m}$). The plume thickness crudely scales with $\delta_g \propto d_b^{2/3}$ observed by Schillings et al. [172] at high current density, for which shear induced diffusion becomes dominant. Equation 4.29, in this case, gives a maximum height of 10.6 cm at $Re = 1000$ for $j = 2000 \text{ A/cm}^2$. It should be noted that the size of the electrode can still be increased by increasing the depth of the electrode to increase the total production rate. However, to further scale-up the height of the electrolyzer, the electrode should be designed such that the bubble size remains small. This can be done, for example, by using surfactants [224, 225], using a more hydrophilic surface [226], engineering the topology of the electrode surface with micro-crevices [227], or using magnetic fields [228].

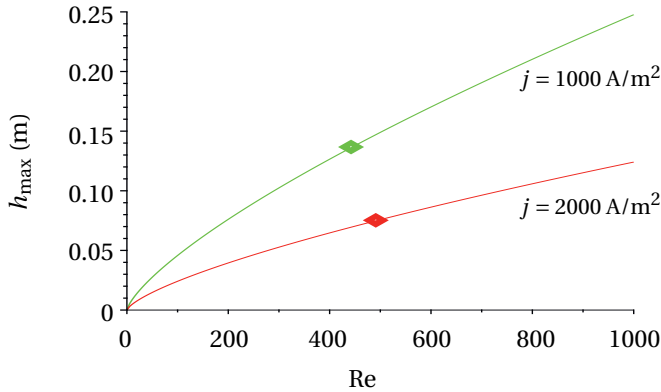


Figure 4.13: Maximum height h_{\max} as a function of Reynolds number for a gap width of 3 mm at atmospheric pressure. The buoyancy driven conditions are represented by the filled diamond. It can be seen that an increase in Reynolds number significantly increases the maximum allowable height of the membraneless parallel plate electrolyzer. The properties used are listed in Table 4.1 and Table 4.3.

4.6. CONCLUSIONS

In this paper, we provided both numerical and analytical modeling approaches to study the multiphase flows in a membraneless parallel plate electrolyzer. Our numerical model is based on a mixture model approach and is used to find the dependence of plume thickness on height, velocity and the current density. Using the momentum equation and neglecting inertial terms, analytical relations for the interstitial velocity (Eq. (4.12)) and superficial velocity (Eq. (4.14)) in the interelectrode gap are derived and verified

$$\mu_M = \frac{\mu}{1-\varepsilon}$$

against the numerical model and existing experimental results. These expressions are valid as long as the plumes remain exponential and thin compared to the gap width. This assumption will not hold above a certain height at high current densities and low velocities. We also derived an expression for the gas fraction at the electrode surface (Eq. (4.20)) using mass conservation and find that the gas fraction at the electrode increases most rapidly in the first few millimeters of electrode height. Furthermore, we derived an analytical expression for the pressure drop along the electrode height (Eq. (4.22)). At small velocities, the increased shear stress due to the bubbles is negated by the increase in buoyancy due to the bubbles.

Finally, analytical expressions for maximum height (Eq. (4.29)) for safe operation of a membraneless parallel plate electrolyzer are provided for a given electrode gap. With the help of analytical results, we calculated this maximum height of the electrolyzer at buoyancy driven and forced flow conditions. We show that the maximum height of the electrode decreases as the current density increases. We find that for an ohmic loss comparable to that of a zero-gap electrolyzer, we can design a membraneless parallel plate electrolyzer operating using natural recirculation with a maximum height of ~ 7 cm at atmospheric pressure and a current density of 2000 A/m^2 and a product purity of 98%. The maximum height of the electrolyzer scales with the electrolyzer gap width l roughly as $l^{1/a} \sim l^{2.2}$. Thus, a larger electrolyzer gap will allow a significantly taller electrolyzer using only the buoyancy driven flow. While the transition to turbulence limits the potential of using the forced flow somewhat, the maximum height of the electrolyzer can be significantly increased by using a forced flow, higher pressure or smaller bubbles.

APPENDICES

4.A. RELATIONS FOR DIFFERENT ANODE AND CATHODE SURFACE GAS FRACTION TO $\mu_M = \frac{\mu}{1-\varepsilon}$

In this section, we generalize the results of main text, valid for $\mu_m = \mu$, to $\mu_m = \frac{\mu}{1-\varepsilon}$ and different electrode surface gas fractions. We define Q as the ratio of the gas fraction at the anode surface and the gas fraction at cathode surface and rewrite Eq. (4.6) for exponential plumes as

$$\varepsilon = \varepsilon_0 \left(e^{-\frac{x}{\delta_g}} + Q e^{-\frac{l-x}{\delta_g}} \right). \quad (4.32)$$

Solving Eq. 4.11 using Eq. (4.32) with no-slip boundary conditions for thin plumes ($e^{-1/\delta} \ll 1$) we get

$$\begin{aligned} w &= 6w_p \bar{x} (k_1 - \bar{x}) + 12(w_p + w_b) \varepsilon_0 \bar{\delta}^2 \left(1 - e^{-\frac{\bar{x}}{\delta}} \right) \left(1 - Q e^{-\frac{l-\bar{x}}{\delta}} \right) \\ &+ 6w_p \varepsilon_0 \bar{\delta} \left(\left(e^{-\frac{\bar{x}}{\delta}} - Q e^{-\frac{l-\bar{x}}{\delta}} \right) (k_1 - 2\bar{x}) - k_1 \right) \\ &- 6w_b \varepsilon_0^2 \bar{\delta}^2 \left(1 - e^{-\frac{2\bar{x}}{\delta}} \right) \left(1 - Q^2 e^{-\frac{2(l-\bar{x})}{\delta}} \right) - 6w_b \varepsilon_0 \bar{\delta}^2 k_2 \left(\varepsilon_0 \bar{\delta} \left(e^{-\frac{\bar{x}}{d}} - Q e^{-\frac{l-\bar{x}}{d}} - 1 \right) + \bar{x} \right), \end{aligned} \quad (4.33)$$

where $k_1 \equiv \frac{1-2\bar{\delta}\varepsilon_0(Q-(Q-1)\bar{\delta})}{1-\bar{\delta}\varepsilon_0(Q+1)}$ and $k_2 = \frac{(Q-1)(2-(Q+1)\varepsilon_0)}{1-\bar{\delta}\varepsilon_0(Q+1)}$. For $Q < 2$, $\varepsilon_0 < 0.5$ and $\bar{\delta} < 0.5$, $k_1 \approx 1$ is a reasonable approximation. The shear rate at the cathode surface is given by

$$\left. \frac{\partial w}{\partial x} \right|_{x=0} = 6(1-\varepsilon_0)(w_p k_1 + w_b \varepsilon_0 \bar{\delta}(2 + \bar{\delta} k_2)) \quad (4.34)$$

The average superficial velocity, $\langle W \rangle = \int_0^1 w(1-\varepsilon)d\bar{x}$ using Eq. (4.33) for $w_b \gg w_p$, can be written as

$$\begin{aligned} \langle W \rangle = w_p (1 - 6\varepsilon_0 \bar{\delta}) + 3w_b \varepsilon_0 \bar{\delta}^2 k_2 (1 - 2\bar{\delta} \varepsilon_0 (Q + 1)) \\ + 3w_b \varepsilon_0 \bar{\delta}^2 (4 - 2\varepsilon_0 - (4(Q + 1) + \varepsilon_0(1 - 3Q^2 + 4Q))\bar{\delta}). \end{aligned} \quad (4.35)$$

For $Q = 1$, Eq. (4.35) reduces to

$$\langle W \rangle = w_p (1 - 6\varepsilon_0 \bar{\delta}) + 12w_b \varepsilon_0 \bar{\delta}^2 \left(1 - 2\bar{\delta} - \frac{\varepsilon_0(1 + \bar{\delta})}{2} \right). \quad (4.36)$$

The differences with Eq. 13 are of the order ε_0 as expected. In the limit $\bar{\delta} \gg 1$, the velocity profile is given by

$$u = 6\bar{x}(1-\bar{x})(w_p + w_b \varepsilon_0(Q+1))(1 - (Q+1)\varepsilon_0). \quad (4.37)$$

The extra $(1 - (Q+1)\varepsilon_0)$ term in Eq. (4.37) is due to $\mu_r = \frac{1}{1-\varepsilon}$, where the gas fraction becomes a constant given by $\varepsilon = (Q+1)\varepsilon_0$. For $\bar{\delta} \gg 1$, the superficial velocity, $\langle W \rangle = \int_0^1 u(1-\varepsilon)d\bar{x}$ can be written as

$$\langle W \rangle = (w_p + (Q+1)w_b \varepsilon_0)(1 - (Q+1)\varepsilon_0)^2. \quad (4.38)$$

Here again, we see the combined effect of modified viscosity and the effect of liquid gas fraction on superficial velocity through the term $(1 - (Q+1)\varepsilon_0)^2$ in a buoyancy assisted pressure driven flow.

Using Eq. (4.33), we can rewrite Eq. (4.17) for $e^{-1/\bar{\delta}} \ll 1$ as

$$\begin{aligned} \langle W_{g,c} \rangle = -(3k_2 \bar{\delta} + 4)\bar{\delta}^3 w_b \varepsilon_0^3 + 3\bar{\delta}^2 (2w_b \bar{\delta}(1 + k_2 \bar{\delta}) - w_p(k_1 - \bar{\delta})) \varepsilon_0^2 \\ + 6w_p \bar{\delta}^2 \varepsilon_0(k_1 - 2\bar{\delta}) + w_s \bar{\delta} \varepsilon_0. \end{aligned} \quad (4.39)$$

Equation (4.39) can be solved for ε_0 to give the electrode surface gas fraction. For low values of $\varepsilon_0 \ll 1$, we get

$$\varepsilon_l = \frac{\langle W_{g,c} \rangle}{\bar{\delta}(6w_p \bar{\delta}(k_1 - 2\bar{\delta}) + w_s)}, \quad \varepsilon_h = \sqrt{\frac{\langle W_{g,c} \rangle}{6w_b \bar{\delta}^3(1 + k_2) - 3w_p(k_1 - \bar{\delta})}}. \quad (4.40)$$

A semi-analytical solution is obtained by solving Eq. (4.36) and Eq. (4.39) for ε_0 and w_p . However, an analytical approximation can also be obtained by using Eq. (4.48) and assuming $\bar{\delta}_c = \bar{\delta}_a = \bar{\delta}$ to give ε_0 and then solving Eq. (4.36) for w_p . The ε_0 obtained using Eq. (4.48) gives slightly lower values for ε_0 than the one obtained by simultaneously solving Eq. (4.36) and Eq. (4.39).

NATURAL RECIRCULATION VELOCITY

For $Q < 2$, $\varepsilon_0 < 0.5$ and $\bar{\delta} < 0.5$, $k_1 \approx 1$, so that we can rewrite Eq. (4.35) for $\varepsilon_0 \bar{\delta} \ll 1$ and $\bar{\delta} \ll 1$ as

$$w_p = (1 + 6\varepsilon_0 \bar{\delta}) \langle W \rangle - 6w_b \varepsilon_0 \bar{\delta}^2 (2 - \varepsilon_0 + k_2/2). \quad (4.41)$$

We can again integrate w_p to get the total pressure drop as

$$\Delta P = -\frac{12\mu h \langle W \rangle}{l^2} \left(1 - \left(\frac{\langle W \rangle_{nc}}{\langle W \rangle} \right)^{1+2b} \right), \quad (4.42)$$

with

$$\langle W \rangle_{nc} \equiv \left(\frac{6w_b \varepsilon_0 (2 - \varepsilon_0 + k_2/2)}{(1 + 2a)(1 + 6\bar{\delta} \varepsilon_0 / (1 + a))} \left(\frac{\mathcal{A} h^a}{l} \right)^2 \right)^{\frac{1}{1+2b}}. \quad (4.43)$$

For $Q = 1$, $k_2 = 0$. We have an addition term, $\frac{6\bar{\delta} \varepsilon_0}{1+a}$, in Eq. (4.43) compared to Eq. (4.23) arising due to the non-constant relative viscosity μ_r . For $\Delta P = 0$, Eq. (4.42) gives the natural recirculation velocity as $\langle W \rangle = \langle W \rangle_{nc}$.

4.B. EXPRESSIONS FOR DIFFERENT ANODE AND CATHODE PLUME THICKNESS

In our model, we have assumed equal plume thickness at the cathode and the anode. However, this assumption does not always hold, and the plume thickness can be different on the two sides, if the bubble diameter or volumetric gas flow rates are significantly different. In this section, we provide generalized expressions for different plume thicknesses $\bar{\delta}_a$ at the anode and $\bar{\delta}_c$ at the cathode, respectively so that Eq. (4.6) can be rewritten as:

$$\varepsilon = \varepsilon_0 \left(e^{-\frac{x}{\bar{\delta}_c}} + Q e^{-\frac{l-x}{\bar{\delta}_a}} \right). \quad (4.44)$$

Assuming $\mu_m \approx \mu$ and solving Eq. 4.11 using Eq. (4.44) with no-slip boundary conditions for thin plumes compared to interelectrode gap ($e^{-1/\bar{\delta}_c} \ll 1$ and $e^{-1/\bar{\delta}_a} \ll 1$), we get

$$w = 6w_p \bar{x}(1 - \bar{x}) + 12w_b \varepsilon_0 \left(\bar{\delta}_c^2 \left(1 - \bar{x} - e^{-\frac{\bar{x}}{\bar{\delta}_c}} \right) + Q \bar{\delta}_a^2 \left(\bar{x} - e^{-\frac{l-\bar{x}}{\bar{\delta}_a}} \right) \right). \quad (4.45)$$

The average superficial velocity, $\langle W \rangle = \int_0^1 w(1 - \varepsilon) d\bar{x}$ using Eq. (4.45) for thin plumes with respect to interelectrode gap ($\bar{\delta}_a^2 \ll 1$, $e^{-1/\bar{\delta}_a} \ll 1$, $\bar{\delta}_c^2 \ll 1$ and $e^{-1/\bar{\delta}_c} \ll 1$), can be written as

$$\langle W \rangle = w_p + 6w_b \varepsilon_0 (\bar{\delta}_c^2 (1 - 2\bar{\delta}_c - \varepsilon_0 \bar{\delta}_c) + Q \bar{\delta}_a^2 (1 - 2\bar{\delta}_a - Q \varepsilon_0 \bar{\delta}_a)). \quad (4.46)$$

where we assumed $w_p \ll w_b$. For $\bar{\delta}_a = \bar{\delta}_c = \bar{\delta}$, $\varepsilon_0 \bar{\delta} \ll 1$ and $Q = 1$, Eq. (4.46) reduces to Eq. (4.14). Using Eq. (4.45), we can rewrite Eq. (4.17) as

$$\langle W_{g,c} \rangle = 6w_b \bar{\delta}_c^2 (\bar{\delta}_c - 2\bar{\delta}_c^2 + 2Q \bar{\delta}_a^2) \varepsilon_0^2 + (6\bar{\delta}_c (1 - 2\bar{\delta}_c) w_p + w_s) \bar{\delta}_c \varepsilon_0. \quad (4.47)$$

Solving Eq. (4.47) for ε_0 , we again obtain Eq. (4.21) with

$$\begin{aligned}\varepsilon_1 &= \frac{\langle W_{g,c} \rangle}{\bar{\delta}_c(6w_p\bar{\delta}_c(1-2\bar{\delta}_c) + w_s)}, \\ \varepsilon_h &= \sqrt{\frac{\langle W_{g,c} \rangle}{6\bar{\delta}_c^2(\bar{\delta}_c - 2\bar{\delta}_c^2 + 2Q\bar{\delta}_a^2)(1 - 12\bar{\delta}_c(1 - 2\bar{\delta}_c)^2)}w_b}}.\end{aligned}\quad (4.48)$$

4.C. EXPRESSIONS FOR A STEP FUNCTION GAS FRACTION PROFILE

In Fig. 4.9, we observed that at high current density, the plume is no longer exponential and attains more of a block-shape. In this appendix, we provide analytical expressions for velocity profiles and surface gas fraction, assuming a step function gas-fraction profile

$$\varepsilon = \begin{cases} \varepsilon_0, & x < \delta_b \\ 0, & \delta_b \leq x \leq l - \delta_b \\ \varepsilon_0, & l - \delta_b < x < l, \end{cases}\quad (4.49)$$

where δ_b is the thickness of the plume. At the interface of the plume, we assume continuity of flow and shear stress. Using no slip conditions at the electrode surface and solving Eq. (4.11) for $\mu_r = \frac{1}{1-\varepsilon}$ using Eq. (4.49) gives

$$\begin{aligned}u &= 6w_p\bar{x}(1-\bar{x}) \\ -6\varepsilon_0 &\begin{cases} [l]w_p\bar{x}(1-2\bar{\delta}_b) + w_b\bar{x}(\bar{x}-2\bar{\delta}_b), & x < \delta_b \\ w_p\bar{\delta}_b(1-2\bar{\delta}_b) - w_b\bar{\delta}_b^2, & \delta_b \leq x \leq l - \delta_b \\ w_p(1-\bar{x})(1-2\bar{\delta}_b) + w_b(1-\bar{x})(1-\bar{x}-2\bar{\delta}_b), & l - \delta_b < x. \end{cases}\end{aligned}\quad (4.50)$$

Riviere and Cartellier [180] took a similar approach for a more general gas fraction profile with an additional gas free layer near the electrode and a low gas fraction in the core with a higher gas fraction region between the two regions. In their analysis, they used a different closure model for shear stress giving $\varepsilon\mu_m$ instead of μ_m in Eq. (4.2).

The average superficial velocity using $\langle W \rangle = \int_0^1 u(1-\varepsilon)d\bar{x}$ and Eq. (4.50) gives

$$\langle W \rangle = (1 - 6\varepsilon_0\bar{\delta}_b)w_p + 6w_b\varepsilon_0\bar{\delta}_b^2\left(1 - \frac{2\bar{\delta}_b}{3}\right).\quad (4.51)$$

The average superficial gas velocity at the cathode $\langle W_{g,c} \rangle = \int_0^{\bar{\delta}_b} u\varepsilon_0 d\bar{x}$ can be written as

$$\langle W_{g,c} \rangle = \varepsilon_0^2\bar{\delta}_b^2(4\bar{\delta}_b w_b - 3w_p(1-2\bar{\delta}_b)) + \varepsilon_0\bar{\delta}_b(w_p\bar{\delta}_b(3-2\bar{\delta}_b) + w_s).\quad (4.52)$$

Equation (4.52) can be solved numerically to give the electrode surface gas fraction ε_0 . For low values of $\varepsilon_0 \ll 1$, we get

$$\varepsilon_1 = \frac{\langle W_{g,c} \rangle}{\bar{\delta}_b(w_p\bar{\delta}_b(3-2\bar{\delta}_b) + w_s)},\quad (4.53)$$

where w_p can be obtained for a given superficial liquid velocity using Eq. (4.51). Note that the expression for ε_1 is equal to that of Eq. (4.39) for $Q = 1$ upon replacing $6\delta_g(1 - 2\delta_g)$ with $3\delta_b(1 - 2\delta_b/3)$. It can be seen from the Fig. 4.11 that for $j = 500 \text{ A/m}^2$, the exponential result of Eq. (4.39) gives satisfactory agreement with the numerical result, while for $j = 2000 \text{ A/m}^2$ Eq. (4.53) gives a slope similar to the numerical solution for the initial height of the electrode.

4.D. EFFECT OF BUBBLE DIAMETER

In Fig. 4.10, we see that velocities from numerical model shows deviation from the experimental results, particularly on the oxygen side because we assumed that oxygen bubbles are of similar size as the hydrogen bubbles. However, Boissonneau [118] suggest in their discussion that the plume on the oxygen side is larger than the plume on the hydrogen side. This may be due to the larger size of the oxygen bubble than the hydrogen bubble. Here, we shortly discuss the results with different bubble size for oxygen and hydrogen. The mixture Model in COMSOL allows only one dispersed phase and one continuous phase. In order to simulate different bubble size for oxygen and hydrogen, we use following distribution of bubble size in the horizontal direction

$$d_{b,\text{new}} = \begin{cases} d_b, & x \leq l/3 \\ d_b + \frac{0.5d_b}{l/3}(x - l/3), & l/3 < x < 2l/3 \\ 1.5d_b, & x \geq 2l/3 \end{cases} \quad (4.54)$$

Equation (4.54) assumes that the oxygen bubbles are 50% bigger than the hydrogen bubbles. In the region $l/3 < x < 2l/3$ it is assumed that the diameter of dispersed phase bubbles increases from hydrogen bubble diameter to that of the oxygen bubble diameter linearly. As the bubble sizes are not reported for the oxygen side, we have used the same bubble size for both hydrogen and oxygen in the main text. Fig. 4.14 shows a comparison between the dispersed phase velocity profiles using this approach to that reported by Boissonneau [118]. We see that accounting for different bubble sizes for hydrogen and oxygen gives a better agreement between the experiments and our numerical simulations. This is because bigger bubbles provide larger buoyancy and terminal rise velocity.

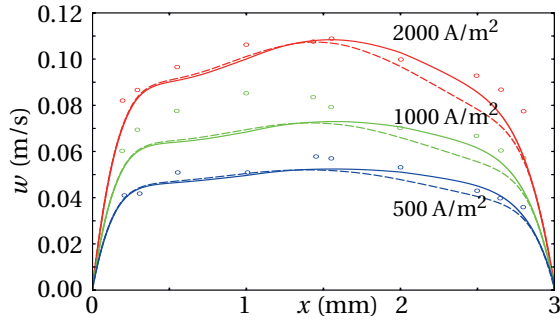
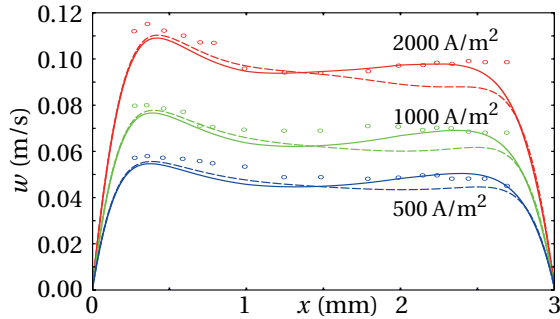
(a) $z = 20$ mm(b) $z = 35$ mm

Figure 4.14: Gas phase velocity profiles for the three current densities: $j = 500 \text{ A/m}^2$ (blue), $j = 1000 \text{ A/m}^2$ (green), and $j = 2000 \text{ A/m}^2$ (red). The circles represent the experimental measurements from Boissonneau [118], the dashed line represents the numerical solution using the bubble diameter from Table 4.2 for both oxygen and hydrogen, and the solid line represents the numerical solution where the bubble diameters are different on the oxygen and the hydrogen side, and given by Eq. (4.54). We clearly see that accounting for different bubble sizes for hydrogen and oxygen gives a better agreement between the experiments and our numerical simulations.

5

AN ANALYTICAL MODEL FOR THE VELOCITY AND GAS FRACTION PROFILES NEAR GAS EVOLVING ELECTRODES

Understanding multiphase flow close to the electrode surface is crucial to the design of electrolyzers, such as alkaline water electrolyzers for the production of green hydrogen. Vertical electrodes develop a narrow gas plume near their surface. We apply the integral method to the mixture model. Considering both exponentially varying and step-function gas fraction profiles, we derive analytical relations for plume thickness, velocity profile, and gas fraction near the electrode as a function of height and current density. We verify these analytical relations with the numerical solutions obtained using COMSOL. We find that for low gas fractions, the plume thickness decreases with an increase in current density for an exponentially varying gas fraction profile. In contrast, the plume thickness increases with increasing current density at high gas fractions for an approximately step-function-shaped gas fraction profile, in agreement with experiments from the literature.

5.1. INTRODUCTION

Many electrochemical reactions produce gaseous products with low solubility in the electrolyte. In this case, bubbles are evolved at the electrode surface, for example, in the production of aluminium [230], sodium chlorate [118], chlorine [231, 232], and hydrogen using water electrolysis [157, 178, 208, 233, 234]. Bubbles add to the resistance of the electrochemical systems by decreasing the effective conductivity of the electrolyte [15, 145, 193, 208, 222, 235] and by taking away the reactive electrode area [225, 236–240]. Bubbles also induce convection in the electrolyte [241–243], increasing the mass transport of reactants and products. The efficiency of the electrochemical cell is, thus, closely related to the two-phase hydrodynamics of bubbles and the electrolyte [244, 245].

Gas-evolving electrodes are usually oriented vertically [167] to avoid bubble accumulation. Once released from the electrode surface, bubbles move primarily in a vertical direction due to their buoyancy and the resulting electrolyte flow. Their drag on the fluid induces natural convection of the electrolyte. Several hydrodynamics forces push the bubbles in the lateral direction, forming a bubble curtain or plume, as shown in Fig. 5.1.

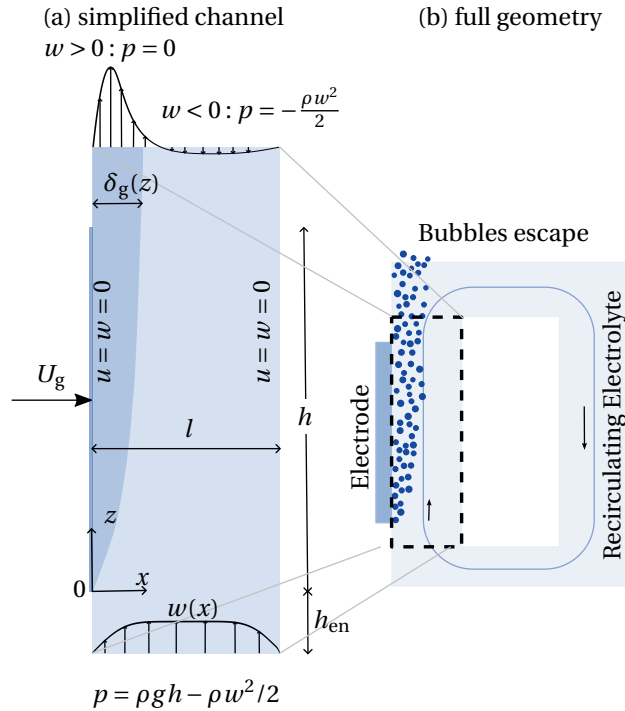


Figure 5.1: A schematic of the gas fraction profile and velocities near a gas-evolving electrode with natural convection electrolyte recirculation. Opposite the electrode may be the membrane in a conventional configuration, or the bipolar plate or back-wall in a zero-gap configuration. The gas bubbles are generated at the electrode surface and escape from the top. The liquid electrolyte recirculates in the cell through a downcomer. We simulate only a channel geometry shown on the left. The gas bubbles are generated at the electrode surface and develop a plume of width δ_g . The liquid electrolyte moves vertically with velocity $w(x, z)$. The boundary conditions used are shown adjacent to each of the boundary.

The study of velocity plumes near a vertical wall has been of interest for a long time, particularly for natural convection effects [246–252]. In electrochemical applications, gas may be evolved at electrodes on two opposing surfaces, for example, in a membrane-less electrolyzer [110, 124, 128, 157, 158, 161, 162, 165] or only one of the two surfaces, for example, in a zero-gap electrolyzer [151, 222, 253, 254] or a conventionally divided electrolyzer in which the second surface is a membrane or a diaphragm [145, 255].

Previously, analytical attempts have been made to study the case of two adjacent gas-evolving electrodes resulting in two plumes on opposite walls [157, 172, 178, 180]. Reference [214] derives a criterion for the occurrence of back-flow. In Refs. [157, 180], the relations for the velocity profile and the wall shear stress are derived assuming a known gas fraction profile. While Ref. [180] used experiments to characterize the gas fraction profile, Ref. [157] performed multiple simulations to relate the plume thickness to the operating parameters. Reference [172] used a thermal analogy and dimensional analysis to predict the scaling of plume thickness with geometric and operating parameters. However, the prefactors for the scaling laws were not established due to the use of simple dimensional analysis.

In this work, we focus on a single plume, relevant for electrochemical cells where the bubbles are produced at only one electrode, when there is a membrane or diaphragm in between the electrodes, or when the two electrodes are placed far apart. We start from an integral method similar to that previously used for studying natural convection due to solutal and thermal effects [247–249, 252, 256]. Our model contains several features somewhat particular to the diffusion of gas bubbles - for example, the use of a constant flux boundary condition, the effect of gas fraction on viscosity and density, and the existence of a maximum gas fraction. Such a maximum gas fraction is a feature typical to the diffusion of electrolytic bubbles, owing to the volume they take up, and does not arise in the case of diffusion of heat or species. To model this, we consider a step-function gas fraction profile, in addition to the widely used exponential profile, in the integral method. Using an assumed velocity profile, modified here to take into account the effect of a finite domain, we provide analytical relations for the gas plume thickness, liquid velocity profile, and liquid flow rate as a function of the height and current density of the electrolyzer.

5.2. MODEL EQUATIONS

We use the laminar mixture model formulation [171, 172, 181] to describe the two-phase hydrodynamics in the electrochemical cell.

The liquid velocities in the x and z direction are denoted by u and w , respectively and we will use a subscript ‘g’ to denote the gas quantities. The volume fraction of gas bubbles is denoted by ε and capital letters are used to denote superficial velocities: $\mathbf{U} = (1-\varepsilon)\mathbf{u}$. We will use U_g here, only to denote the positive horizontal superficial gas velocity at the electrode surface. The continuity equation for the gaseous phase at steady state is given by $\nabla \cdot (\varepsilon \mathbf{u}_g) = 0$, which can be integrated over a Gaussian pillbox bordering the electrode at $x = 0$ to give

$$U_g = \frac{d}{dz} \int_0^l \varepsilon w dx, \quad (5.1)$$

where we assumed that the slip velocity in the vertical direction $w_s \equiv w_g - w$ is negligible compared to the liquid velocity, so $w_s \ll w$. The superficial gas velocity at the electrode in the x -direction is given by Faraday's law

$$U_g = \frac{V_m}{nF} j, \quad (5.2)$$

where V_m is the molar volume of the gas and n is the number of electrons required to produce one gas molecule. Here we assumed that the gas evolution efficiency [204, 257] is 100% so all of the produced gas is evolved as bubbles. At the surface of the electrode, $x = 0$, we can write

$$U_g = \varepsilon u_g|_{x=0} = \varepsilon u_s|_{x=0}. \quad (5.3)$$

For a gas density much lower than that of the liquid, $\rho_g \ll \rho$, the vertical z -component of the steady state momentum conservation equation for the gas-liquid mixture can be approximated [157] by

$$\frac{\partial(1-\varepsilon)w^2}{\partial z} + \frac{\partial(1-\varepsilon)uw}{\partial x} = -\frac{1}{\rho} \frac{\partial P}{\partial z} + \frac{\partial}{\partial x} \left(\nu_m \frac{\partial w}{\partial x} \right) + \varepsilon g, \quad (5.4)$$

where $P = p + \rho g z$ is the reduced pressure and p is the absolute pressure. Note that in Eq. (5.4), we neglected the slip velocity in the vertical direction for the typically small electrochemical bubbles. This allows us to approximate the mixture velocity with the liquid velocity. The mixture kinematic viscosity ν_m can be expressed empirically using the liquid viscosity ν and gas fraction ε as $\frac{\nu_m}{\nu} = \frac{1}{1-\varepsilon} \geq 1$ [186, 188, 214].

The model is completed by using empirical relations describing the relative velocity between the bubbles and the electrolyte. While it has been observed that the bubble size increases along the height of the electrode [118, 205], we assume here a constant bubble diameter d_b for simplicity. The bubble diameter may also increase with increasing current density [118], which can be easily included in the analytical model by inserting the dependence of d_b on current density. The relative velocity of a bubble is mainly Stokes' rise velocity in the vertical direction, given by $\mathbf{u}_{St} = \frac{g d_b^2}{18\nu} \mathbf{e}_z$, where \mathbf{e}_z is the unit vector in the vertical direction. For $d_b \gtrsim 100 \mu\text{m}$, Stokes's velocity should be corrected for the bubble Reynolds number as this becomes greater than 1 [258–260]. In this paper, we neglect the effect of hindrance on the freely rising bubbles. For small gas fractions, the lateral slip velocity of the bubbles is primarily due to hydrodynamic dispersion $\mathbf{u}_{Hd} = -\frac{g d_b^3}{36\nu} \frac{\mathbf{D}\nabla\varepsilon}{\varepsilon(1-\varepsilon)}$ [171, 172]. The non-isotropic dimensionless dispersion tensor is given by $\mathbf{D} = \begin{pmatrix} 1 & 0 \\ 0 & 8 \end{pmatrix}$ [157, 171, 172, 191] so the bubble dispersion coefficient¹ becomes

$$D_b = \frac{g d_b^3}{36\nu}, \quad (5.5)$$

¹From the gas conservation equation [157], if only hydrodynamic dispersion is present:

$$\mathbf{U}_m \cdot \nabla \varepsilon = \nabla \cdot (\varepsilon(1-\varepsilon)\mathbf{u}_s) = \nabla \cdot \left(g d_b^3 \mathbf{D} \nabla \varepsilon / 36\nu \right) = \nabla \cdot (D_b \mathbf{D} \nabla \varepsilon),$$

so the effective dispersion coefficient in the horizontal direction can be written as $D_b = d_b w_{St} / 2 = \frac{g d_b^3}{36\nu}$. Here \mathbf{U}_m is the superficial mixture velocity.

in the horizontal direction. In the case of turbulent flow, a turbulent contribution may be added. However, this will not be a constant and it will vanish at the electrode. Also, the viscosity will be impacted by turbulence. Therefore, we limit our study to laminar conditions with a spatially constant bubble dispersion coefficient.

Mono-sized spheres have a maximum theoretical packing density of $\pi/\sqrt{18} \approx 0.74$ (Kepler's Conjecture) [261], while a maximum packing density of 0.6 has been reported for loosely packed particles [262] and decreases as the particle size decreases [263]. As the gas flux from the electrode is increased, the gas fraction tends to a maximum value [184, 264–267]. In electrolytes, still smaller maximum values of $\varepsilon_{\max} = 0.2 - 0.5$ have been found and were attributed to the observed coalescence barrier [184, 268]. Electrolytic bubbles have a surface charge, leading to electrostatic repulsion between bubbles [184]. The resulting interaction force due to this coalesce inhibition may be described using the granular/frictional/solid pressure [269–272]. The additional transverse dispersion and vertical rise velocity can be used to describe maximum gas fraction in plumes. Additionally, there may be other transverse bubble interaction forces causing an *apparent* maximum gas fraction. For example, shear-induced diffusion has been shown to lead to an approximately step-function-shaped gas fraction profile [157, 171, 273] as well. While the exact expression will depend on the underlying mechanisms, we propose a heuristic relationship to simulate the maximum gas fraction by writing the slip velocity as

$$\mathbf{u}_s = \mathbf{u}_{\text{St}} + \frac{\mathbf{u}_{\text{Hd}}}{1 - \varepsilon/\varepsilon_{\max}}. \quad (5.6)$$

In this expression, the slip velocity will increase primarily in the horizontal direction, in which the gas fraction gradients are largest, as the gas fraction approaches a maximum. So, the maximum gas fraction is heuristically attributed here to the additional dispersion of the bubbles. This additional slip velocity will push the bubbles away from the region of maximum gas fraction. The overall slip velocity, however, will typically remain small because as the gas fraction approaches its maximum, $\frac{1}{1 - \varepsilon/\varepsilon_{\max}}$ increases, but $\nabla \varepsilon$ also reduces sufficiently fast.

5.3. ANALYTICAL MODEL

We consider a vertical rectangular channel with width l and height h as shown in Fig. 5.1. The gas flows in a thin plume with a thickness $\delta_g(z)$ and the gas fraction at the electrode surface is denoted by $\varepsilon_0(z)$, where z is the vertical coordinate. We use the integral method [247–249, 252, 256] to find analytical relations for gas plume thickness δ_g , wall gas fraction ε_0 , flow boundary layer thickness δ_f and characteristic velocity \mathcal{W} as a function of height z , and the superficial gas flux U_g entering through the electrode. Educated guesses for the gas fraction and velocity profiles that satisfy the boundary conditions as a function of these parameters are inserted into the governing differential eqns. (5.1), (5.3) and (5.4), which we subsequently integrate from $x = 0$ to $x = l$. The resulting algebraic equations can then be solved exactly. In section 5.3.2, we will consider a step-function shaped gas fraction, relevant for high current densities and heights giving gas fractions close to the maximum, but first we assume an exponential variation in the gas fraction.

5.3.1. EXPONENTIAL GAS FRACTION PROFILE

For relatively low electrode height and low gas flux at low current density or elevated pressure, we assume that the gas fraction decreases approximately exponentially with x as

$$\varepsilon = \varepsilon_0 e^{-x/\delta_g}, \quad (5.7)$$

where δ_g is the gas fraction e-folding plume thickness, whose development with z is yet unknown. For the velocity profile, we take

$$w = \begin{cases} W \left(1 - \frac{x}{\delta_f}\right) \left(1 - e^{-x/\delta_g}\right), & x < \delta_f \\ 0, & x \geq \delta_f. \end{cases} \quad (5.8)$$

Here δ_g primarily determines the velocity gradient at the wall and the flow boundary layer thickness δ_f determines the distance over which the velocity goes to zero. Since the velocity is driven by buoyancy, it will always hold that $q \equiv \delta_f/\delta_g > 1$. For thermal convection in a semi-infinite medium, often e^{-x/δ_f} is used instead of $1 - x/\delta_f$, so no separate case $w = 0$ has to be introduced to avoid negative values. A polynomial decrease beyond the maximum is also used in literature [247–249]. In our case of finite channel width, we find from the simulations that back-flow precludes an exponential-like shape of the velocity profile. Instead, we chose a linear decrease of velocity profile for simplicity. Negative vertical velocities arise far away from the electrode as a consequence of the adverse pressure gradient in the boundary conditions shown in Fig. 1. The boundary conditions model the unavoidable pressure drops associated with fluid deceleration and give rise to this backflow. In the analytical derivation, however, we neglect the responsible $\partial P/\partial z$ term [249]. Eq. (5.8) does not capture negative velocities away from the electrode in case of an adverse pressure gradient. This downflow has to be considered when estimating the total liquid flow rate. We define the ratio of the flow boundary layer thickness to the gas plume thickness as

$$q \equiv \frac{\delta_f}{\delta_g}. \quad (5.9)$$

Using Eq. (5.7) and Eq. (5.8) for $\partial P/\partial z = 0$ and neglecting the effect of the gas fraction on viscosity, slip velocity, and inertial terms on the left-hand side of Eq. (5.4) for small ε , we derive the following expressions (see 5.A):

$$\delta_g = \left(\frac{\nu D_b^2 z}{g U_g} \frac{q+2}{q H(q)} \right)^{1/5}, \quad (5.10)$$

$$W = \left(\frac{D_b g^2 U_g^2 z^3}{\nu^2} \frac{q^2}{(q+2)^2 H(q)^3} \right)^{1/5}, \quad (5.11)$$

$$\varepsilon_0 = \left(\frac{\nu U_g^4 z}{g D_b^3} \frac{(q+2)}{q H(q)} \right)^{1/5}, \quad \text{and} \quad (5.12)$$

$$w' \equiv \frac{\partial w}{\partial x} \Big|_{x=0} = \frac{W}{\delta_g} = \left(\frac{g^3 U_g^3 z^2}{\nu^3} \frac{q^3}{D_b q(q+2)^3 H(q)^3} \right)^{1/5}, \quad (5.13)$$

where $H(q) \equiv \frac{4e^{-q} - e^{-2q} + 2q - 3}{4q}$. The value of q can be explicitly calculated by

$$q \approx \sqrt{\frac{50\text{Pr}_b}{7} \frac{1 + \sqrt{0.3\text{Pr}_b}}{1 + \sqrt{\text{Pr}_b}}}. \quad (5.14)$$

where the bubble Prandtl number $\text{Pr}_b = \frac{\nu}{D_b}$ and D_b is given by Eq. (5.5). Electrolytically generated bubbles typically have $d_b < 150 \mu\text{m}$, so $D_b < \nu$ and $\text{Pr}_b > 1$ or $q > 2$. Note that U_g can be replaced by the current density j using Eq. (5.2). The above analytical results have a different prefactor but the same scalings with z and U_g as those previously reported for thermal and solutal natural convection with constant flux (Neumann) boundary conditions [246–250], shown in Eq. (5.44). We see that the plume widens very slowly with height, proportional to $z^{1/5}$, but much strongly with the bubble diameter. From Eq. (5.5), $D_b \propto d_b^3$, so that Eq. (5.10) gives $\delta_g \propto d_b^{6/5}$. From Eq. (5.10), we predict that the gas plume thickness decreases with increasing U_g or current density j . This is because the velocity near the electrode increases with current density, increasing the convective effect, which decreases the plume thickness. The same is predicted in Ref. [172]. In Ref. [274], the hydrogen bubble plume thickness decreased in an alkaline electrolyte under normal gravity. However, the bubble size was found to decrease with increasing current density in this experiment, which could possibly by itself also explain this result. However, sometimes this decreasing plume thickness is not observed experimentally. Reference [209] shows an increase in gas plume thickness with increasing current density. A likely reason is that $D_b^2 \sim d_b^{6/5}$ increases more than linearly with j .

Note that the liquid flow rate, proportional to $W\delta_g$, increases with z . In the finite domain used in the simulations, this increase has to be compensated by a downflow away from the electrode that increases in magnitude with increasing height. We will discuss in more detail how to do this in 5.D.

The scaling $\delta_g \propto z^{1/5}$ is commonly obtained for constant flux while $z^{1/4}$ is found using a constant gas fraction, or temperature in case of thermal natural convection. As expected for simulations with constant current density, our scaling $\delta_g \propto z^{1/5}$ is actually a better fit to the simulations of Ref. [172] than the $z^{1/4}$ scaling derived there.

5.3.2. STEP-FUNCTION GAS FRACTION PROFILE

The exponential-shaped gas fraction profile is relevant at high pressure, low current density and small heights or for very large bubble dispersion coefficients D_b due to a large bubble size. Often above a certain height the gas fraction no longer decreases approximately exponentially as a maximum gas fraction is approached. From our simulations, shown later, we see that the distribution of gas fraction near the maximum gas fraction is approximately like a step-function profile:

$$\varepsilon = \begin{cases} \varepsilon_0, & x < \delta_g \\ 0, & x \geq \delta_g. \end{cases} \quad (5.15)$$

Note that we use the same symbol δ_g here to refer to a related but slightly different quantity as before (see Fig. 5.2). We restrict our analysis to a constant $\varepsilon_0 = \varepsilon_{\text{max}}$. This means

that we consider a constant gas fraction with a constant flux at the electrode surface. This boundary condition does not have an analogy in thermal or solutal natural convection. Since in our simulations, the shape of the velocity profile does not change significantly when the gas fraction reaches a maximum, we use the same velocity profile as before. The assumed profiles of Eq. (5.8) and Eq. (5.15) are schematically shown in Fig. 5.2.

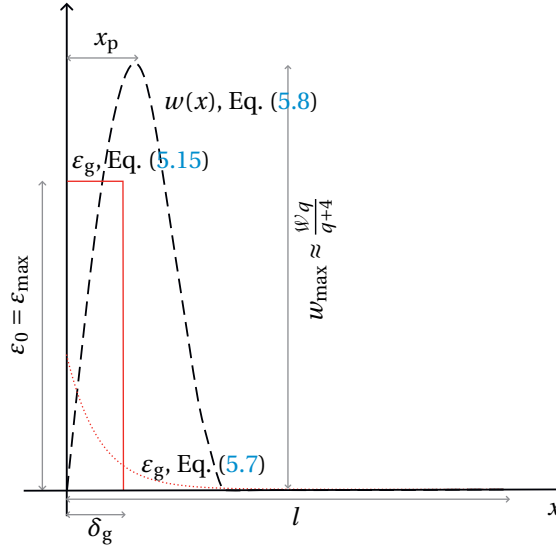


Figure 5.2: The assumed gas fraction profile (Dotted: exponentially varying, Solid: step-function) and the assumed velocity profile (dashed: Eq. (5.8)). The peak velocity $w_{\max} \approx \frac{Wq}{q+4}$ occurs at $x_p = \delta_g(q+1 - \text{LambertW}(e^{q+1}))$, where $\text{LambertW}(x)e^{\text{LambertW}(x)} = x$. The approximation of w_{\max} is obtained from the asymptotic matching of the exact expression $w(x_p)$ and has a maximum error of only 3%.

Rewriting Eq. (5.4) using the no-slip condition $w(x=0) = 0$, $\frac{\partial P}{\partial z} = 0$, and Eq. (5.15), we get

$$W = \frac{g\epsilon_0\delta_g^2}{v_m} \frac{q}{q+2}, \quad (5.16)$$

where $v_m = \frac{v}{1-\epsilon_{\max}}$ is a constant. Substituting Eq. (5.8) and Eq. (5.15) in Eq. (5.4), integrating between $y=0$ and $y=l$ for $\delta_g < \delta_f < l$, and using Eq. (5.16) gives

$$0 = \frac{2v_m W}{q\delta_g} - \frac{d}{dz}(f(q)\delta_g W^2), \quad (5.17)$$

where $f(q) \approx \frac{-0.5e^{-2q} + 8e^{-q} + 0.67(q-2.05)((q-1.22)^2 + 3.98)}{2q^2} - 0.34\epsilon_0 \frac{(q-0.71)^2 + 0.04}{2q^2}$. Note that we round off the coefficients in $f(q)$, and also subsequent expressions, to two significant digits. The dependence on ϵ_0 derives from the gas fraction dependence of inertial terms in Eq. (5.4). Finally, Eq. (5.1) can be rewritten as

$$U_g z = h(q)\delta_g\epsilon_0 W, \quad (5.18)$$

where $h(q) = \frac{1+(2q-4)e^{-1}}{2q}$. We wish to find the scalings of the relevant quantities with a power of z , similar to Eqs. (5.10)-(5.13). Therefore, we express Eqs. (5.16)-(5.18) as power law expressions in q so

$$\mathcal{W} = q^a \frac{g\varepsilon_0\delta_g^2}{3\nu_m}, \quad (5.19)$$

$$0 = \frac{2\nu_m\mathcal{W}}{q\delta_g} - f(1)\frac{d}{dz}(q^{b+1}\delta_g\mathcal{W}^2), \quad (5.20)$$

$$U_g z = h(1)q^c\delta_g\varepsilon_0\mathcal{W}, \quad (5.21)$$

where $a \equiv \frac{\ln\left(\frac{3q}{q+2}\right)}{\ln(q)}$, $b \equiv \frac{\ln\left(\frac{f(q)}{qf(1)}\right)}{\ln(q)}$ and $c \equiv \frac{\ln\left(\frac{h(q)}{h(1)}\right)}{\ln(q)}$. Assuming that q , δ_g , \mathcal{W} are proportional to some power of z , Eqs. (5.19)-(5.21) give $q \propto z^m$, $\mathcal{W} \propto z^{\frac{2}{3}+m\frac{a-2c}{3}}$ and $\delta_g \propto z^{\frac{1}{3}-m\frac{a+c}{3}}$ with

$$m = -\frac{1}{6+3b-4c-a} = \frac{\ln(q)}{\ln\left(\frac{3f(1)^3h(q)^4}{q^2(q+2)f(q)^3h(1)^4}\right)}, \quad (5.22)$$

where we used the definitions of a , b , and c in the final expression. Since a , b and c vanish as $q \rightarrow \infty$, $m = -1/6$ in this limit. Inserting the scalings for q , \mathcal{W} , and δ_g , Eq. (5.20) can be rewritten as

$$q^{b+2}\delta_g^2\mathcal{W} = \frac{2\nu_m}{kf(1)}z. \quad (5.23)$$

Here $k = (b+1)m + \frac{1}{3} - \frac{m}{3}(a+c) + \frac{4}{3} + \frac{2m}{3}(a-2c)$ and lies between 1.43-1.73, using Eq. (5.22). Therefore, we choose a constant value, $k = 1.54$, with a maximum relative error of 12% to simplify Eq. (5.23). Eliminating \mathcal{W} and δ_g , we can solve Eq. (5.19), Eq. (5.21), and Eq. (5.23) for q to give

$$q = \left(\frac{\bar{z}}{\bar{z}_c}\right)^m, \quad (5.24)$$

where

$$\bar{z} \equiv \frac{zU_g^4}{g\varepsilon_0^5\nu_m^2}, \quad \text{and} \quad \bar{z}_c \equiv \frac{0.73h(1)^4}{f(1)^3} \approx \frac{24}{(1-\varepsilon_0)^3}. \quad (5.25)$$

Equation (5.24) is implicit since m itself is a function of q , as given by Eq. (5.22). Combining Eqs. (5.22) and Eq. (5.24) gives

$$\frac{2.2h(q)^4}{q^2(q+2)f(q)^3} = \bar{z}. \quad (5.26)$$

A good approximation, obtained by trial-and-error, to the solution of Eq. (5.26) is given by

$$q \approx \begin{cases} \bar{z}^{-1/6}, & \bar{z} \leq 10^{-9} \\ 1.65\bar{z}^{-1/7}, & 10^{-9} < \bar{z} \leq 10^{-4} \\ (\bar{z}/\bar{z}_c)^{-\frac{(1-\varepsilon_0)^{1/4}}{7}}, & 10^{-4} < \bar{z} \leq \bar{z}_c \end{cases}. \quad (5.27)$$

The power $m = -(1-\varepsilon_0)^{1/4}/7$ in the last approximation depends weakly on ε_0 and varies between -0.11 and -0.14 for $\varepsilon_0 = 0.7$ and $\varepsilon_0 = 0$, respectively. Eq. (5.26) or (5.27) can be

used to obtain the value of q . As $\bar{z} \rightarrow \bar{z}_c$, $q \rightarrow 1$. The first two approximations in Eq. (5.27) have a maximum error of 5% for the respective ranges of \bar{z} , while the last expression has a maximum error of 12% for the given range of \bar{z} . Finally, δ_g solving Eq. (5.19) and Eq. (5.21) gives

$$\delta_g = \left(\frac{v_m U_g z (q+2)}{g \varepsilon_0^2 q h(q)} \right)^{1/3}, \quad (5.28)$$

$$W = \left(\frac{g U_g^2 z^2 q}{v_m \varepsilon_0 (q+2) h(q)^2} \right)^{1/3}. \quad (5.29)$$

where q is given by Eq. (5.26). We can write in the limit $q \gg 1$:

$$\delta_g = \left(\frac{e v_m U_g z}{\varepsilon_0^2 g} \right)^{1/3} \quad \text{and} \quad W = \left(\frac{e^2 g U_g^2 z^2}{v_m \varepsilon_0} \right)^{1/3}. \quad (5.30)$$

and for the limit $q \rightarrow 1$, derived in 5.C:

$$\delta_g = \frac{2.83 v_m^{0.13} U_g^{0.73} z^{0.43}}{g^{0.43} \varepsilon_0^{1.17} z_c^{0.10}} \quad \text{and} \quad W = \frac{2.67 g^{0.21} U_g^{1.15} z^{0.79}}{v_m^{0.55} \varepsilon_0^{0.93} z_c^{0.12}}. \quad (5.31)$$

where we used the last approximation in Eq. (5.27), evaluated at $\varepsilon_0 = 0.4$.

For δ_g , the scaling with height changes from $z^{1/5}$ for an exponential plume, at small heights, to $z^{1/3} - z^{0.43}$ for a step-function gas fraction profile, at large heights. The plume thickness, thus, increases much faster with z as the height increases. The plumes are exponential for very low current densities and $\delta_g \propto U_g^{-1/5}$, see Eq. (5.10). As the current density increases and a maximum wall gas fraction is approached, the step-function gas fraction profile results in the scaling of δ_g between $U_g^{1/3} - U_g^{0.73}$, see Eqs. (5.30) and (5.31).

The dependence of velocity W on height increases from $z^{3/5}$ for an exponential plume to $z^{2/3} - z^{0.79}$ for a step-function gas fraction profile. The scaling for W with current density changes from $U_g^{2/5}$ at low current densities to $U_g^{2/3}$ at higher current densities when the gas fraction approaches a maximum. For the higher current densities, this dependence becomes approximately linear, $U_g^{1.15}$, according to Eq. (5.31). The velocity thus also increases much faster with increasing current density.

In electrolyzers, the wall strain rate is often a quantity of interest, for example, to estimate heat and mass transfer to the electrode. The wall strain rate also has an effect on the removal of bubbles attached to the surface. From Eq. (5.29) and (5.28), we can estimate the wall strain rate $w' \equiv \left. \frac{\partial w}{\partial x} \right|_{x=0}$ as

$$w' = \frac{W}{\delta_g} = \left(\frac{g^2 U_g z \varepsilon_0 q^2}{v_m^2 (q+2)^2 h(q)} \right)^{1/3}. \quad (5.32)$$

which gives, as shown in 5.C:

$$w' = \begin{cases} 6.4 (\varepsilon_0 U_g z v_m^{-1})^{1/3}, & q \gg 1 \\ 3.9 (1 - \varepsilon_0)^{0.06} \varepsilon_0^{0.24} U_g^{0.41} z^{0.35} v_m^{-0.70}, & q \rightarrow 1 \end{cases}. \quad (5.33)$$

Interestingly, the expression for w' has a minimum power of U_g and z near $q \sim 5$. This is because even though the powers of U_g and z in the expression of δ_g and \mathcal{W} increase as the height and the current density increase, the powers in δ_g increase faster than the powers in \mathcal{W} for $q < 5$. For $q > 5$, the powers of U_g and z in δ_g increases slower than in \mathcal{W} . For $q \sim 5$, we find in 5.C

$$w' = 4.8(1 - \varepsilon_0)^{0.05} \varepsilon_0^{0.42} U_g^{0.27} z^{0.31} v_m^{-0.63}. \quad (5.34)$$

From Eqs. (5.32), (5.33) and (5.34), we find that the scaling for w' changes from $U_g^{3/5}$ for an exponential gas fraction profile to $U_g^{0.27} - U_g^{0.41}$ for a step-function gas fraction profile.

Another important quantity for electrolyzers is the liquid flow rate. We can calculate the average superficial liquid velocity, $\langle W \rangle = \frac{1}{l} \int_0^l w(1 - \varepsilon) dx$, to be

$$\langle W \rangle = \frac{U_g z \frac{1 + (q - 1)^2 - 2e^{-q} - 2e^{-1} \varepsilon_0 (q - 0.64)}{\varepsilon_0 l}}{2qh(q)}, \quad (5.35)$$

where q is calculated at an effective height z_{eff} for which the actual average velocity between δ_f and l is negligible. Since we assumed $\partial P / \partial z = 0$ and did not consider any boundary condition for large x we effectively considered a semi-infinite domain in our analysis. In our simulations and in practice, there will usually be an opposing wall and a slight adverse pressure gradient $\partial P / \partial z$, causing some backflow $w < 0$ beyond the plume region, which is neglected in Eq. (5.35). In 5.D, simulations show that a good approximation for the superficial velocity is obtained by evaluating Eq. (5.35) at $z = z_{\text{eff}} \sim h/3$ may be used as a rough approximation for relatively wide channels.

It should be noted that while deriving the results for the step-function gas fraction profile, the diffusion equation is not used. As such, these relations will be valid as long as we have an approximately step-function gas fraction profile with constant ε_0 , irrespective of the mechanism of transverse bubble transport.

5.4. VERIFICATION USING NUMERICAL SOLUTIONS

We solve the mixture model formulation for multiphase flow [157, 171, 172, 181] using COMSOL Multiphysics v5.6, update 2 [182]. The physical properties of the electrolyzer used for the simulations are listed in Table 5.1. We consider an electrolyzer setup as shown in Fig 5.1. The gas is generated at the electrode on the left and escapes from the top boundary. The liquid electrolyte is recirculated back into the electrode channel through a downcomer section. We simulate only the electrode channel as shown in Fig. 5.1. This requires proper boundary conditions at the top and the bottom of the channel.

BOUNDARY CONDITIONS

The mixture model allows only the mixture and gas boundary conditions. At the electrode surface, we want to prescribe a no-slip condition for liquid and the gas flux. In the horizontal direction at the electrode surface, we use an inlet boundary condition such that the gas flux is equal to U_g . In the vertical direction, we impose a zero mixture velocity with zero slip velocity at the boundary nodes. This ensures that a no-slip boundary

Table 5.1: Dimensions and operating conditions used in numerical simulations for verification cases

Properties	Value
Channel Width, l	10 mm
Entrance height, h_{en}	50 mm
Exit height, h_{exit}	50 mm
Electrode height, h	900 mm
Electrolyte density, ρ	1000 kg/m ³
Kinematic viscosity, ν	10 ⁻⁶ m ² /s
Bubble Diameter, d_b	75 μm
Maximum gas fraction, ε_{max}	0.4

condition is imposed for the liquid phase. At the opposite boundary, we use a no-slip condition at the boundary nodes with zero mixture velocity. When the flow at the top is in the positive z -direction, a pressure boundary condition ($p = 0$) is used with gas escaping from the top boundary. When the flow at the top is in the negative z -direction, we specify a local Bernoulli condition $p = -\frac{\rho w^2}{2}$ with no gas recirculating back into the channel. At the bottom, we specify a local Bernoulli condition $p = \rho gh - \frac{\rho w^2}{2}$ with no gas flux. The boundary conditions are also shown in Fig. 5.1. Similar boundary conditions have been previously used for modeling natural thermal convection [275–277]. We compared the results obtained using these boundary conditions with the simulation of the full configuration of Fig. 5.1 in 5.B. Using these boundary conditions, we get the results almost indistinguishable from those in the full configuration, and we could achieve faster and easier convergence of numerical results at larger heights.

VERIFICATION OF STEP-FUNCTION GAS FRACTION PROFILE RELATIONS

We verify our analytical expressions by comparing them with various numerical results obtained using COMSOL. The numerical plume thickness is calculated by $\delta_{g,n} = \int_0^l \varepsilon dx / \varepsilon_0$ and the numerical value of the characteristic velocity \mathcal{W}_n is calculated by $\mathcal{W}_n = w_n' \delta_{g,n}$. We consider different cases involving different current densities, electrode heights, maximum gas fractions, and bubble diameters. All these simulation results are obtained using the properties listed in Table 5.1.

Figure 5.3 and Fig. 5.4 show the development of the gas fraction profile and the velocity profile as a function of height for $U_g = 1$ mm/s with a maximum gas fraction $\varepsilon_{\text{max}} = 0.4$. This corresponds to a current density of 8 kA/m² at atmospheric conditions for hydrogen evolution and is a representative case for the step-function gas function profile. Under some simulated conditions, a degree of turbulence can arise in actuality, which is not included in the simulations. Therefore, these results should be used with caution. We see an increasing plume thickness and peak velocity as the height increases. We also see that the gas fraction remains close to the maximum gas fraction and drops quickly to 0 near the edge of the plume, justifying our assumption of a step-function gas fraction profile. Interestingly, Fig. 5.4 shows that the velocity profiles all cross in the same point around $x \approx 3$ mm, indicating that δ_f should be approximately independent of U_g in this range. This implies that while δ_g increases with increasing U_g , q decreases, so

that $\delta_f = q\delta_g$ does not change. This is also indeed predicted by our analytical solution, as shown in Fig. 5.5.

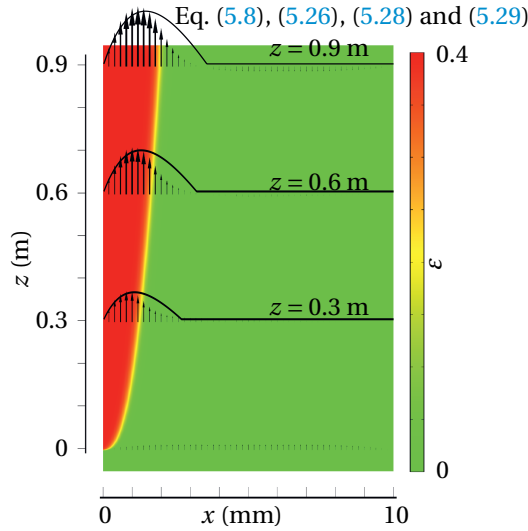


Figure 5.3: The development of gas fraction profile and the velocity profile for the step-function gas fraction profile at $U_g = 1$ mm/s for the properties used in Table 5.1. The gas fraction profile is shown in color, and the numerical velocity profile is overlaid as an arrow plot at $z = 0.3$ m, $z = 0.6$ m and $z = 0.9$ m. The solid lines show the analytical velocity profile given by Eq. (5.8) at the same heights. We used Eqs. (5.28) and (5.29) to determine $\delta_f = q\delta_g$ and \mathcal{W} , after solving Eq. (5.26) numerically for q .

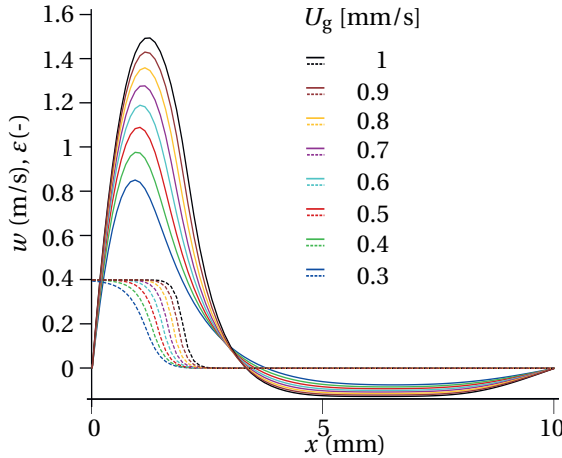


Figure 5.4: Numerical results for gas fraction profiles (dashed) and the velocity profiles (solid) at different current densities at $z = 0.9$ m for the properties listed in Table 5.1. Here, the gas fraction at the electrode surface approaches a maximum value, and we see that the plume thickness, peak velocity and strain rate increase with increasing current density.

The characteristic velocity \mathcal{W} , gas plume thickness δ_g , and strain rate w' as a function of height are shown in Figure 5.6. We see that the analytical results obtained using

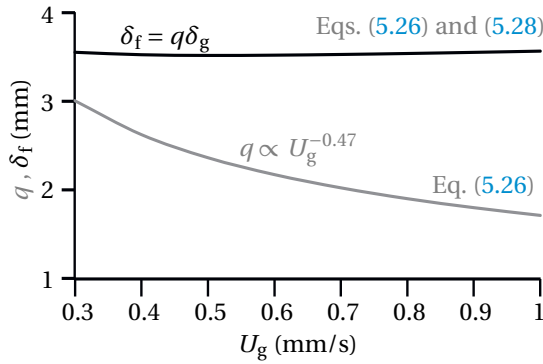


Figure 5.5: Plot showing in our analytical model, the variation of q and δ_f with U_g at $z = 0.9$ m and a relatively high current density at which a step-function can approximate the gas fraction profile. While q decreases, δ_f remains relatively constant. This causes all velocity profiles to cross the same point around $x = 3$ mm in Fig. 5.4. The power $q \propto U_g^{-0.47}$ is obtained using the least squares fit on the analytical results of Eq. (5.26). It is close to the power of $U_g^{-4(1-\epsilon_0)^{1/4}/7}$ predicted by the last approximation in Eq. (5.27), which gives $U_g^{-0.5}$ for $\epsilon_0 = 0.4$.

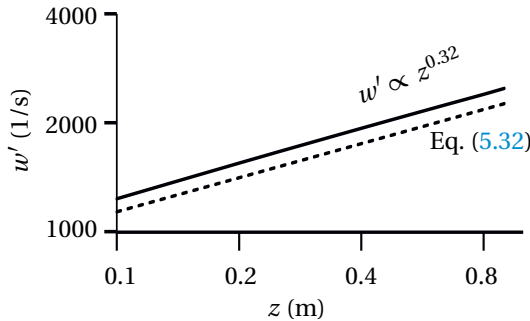
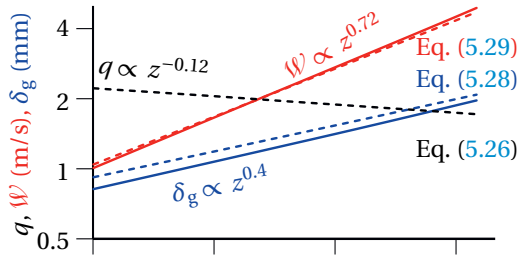


Figure 5.6: Log-log plot of W , plume thickness δ_g , and wall shear rate w' as a function of height z for $U_g = 1$ mm/s using the properties listed in Table 5.1. It can be seen that the analytical results (dashed line) have a reasonably good agreement with the numerical results (solid line). There are small differences in the magnitude, possibly due to the discrepancy in the assumed velocity and gas fraction profiles. We used Eq. (5.26) to numerically solve for q and found that it decreases as the height increases, highlighted explicitly in Eq. (5.27).

Eq. (5.29)-(5.32) show a reasonably good agreement with the numerical results obtained using COMSOL. The dotted lines show the analytical results when q is calculated using Eq. (5.26).

In Figure 5.7, we show \mathcal{W} , δ_g and w' as a function of U_g at a height of 0.9 m for the properties listed in Tab. 5.1. Due to the large range of U_g , we see a transition in scalings for all quantities. At small values of U_g , the results for the exponential-shaped gas fraction profile are valid, so $\mathcal{W} \propto U_g^{2/5}$, $\delta_g \propto U_g^{-1/5}$ and $w' \propto U_g^{3/5}$. In contrast, the results for step-function gas fraction profiles are valid at large values of U_g and we find, from a least squares fit of the numerical results, that $\mathcal{W} \propto U_g^{0.68}$, $\delta_g \propto U_g^{0.42}$ and $w' \propto U_g^{0.26}$. To obtain these scaling analytically, we first calculate q by using Eq. (5.14) for the exponential profile or by numerically solving Eq. (5.26) for the step-function profile. Once the value of q is known, we use Eqs. (5.10), (5.11) and (5.13) for the exponential profile, while Eqs. (5.28), (5.29) and (5.32) are used for the step-function gas fraction profile. We see a good agreement with the numerical results and that the analytical results capture the transition very well. The small offset in the predicted values may be due to the discrepancy in the assumed and actual profiles, also seen in Fig. 5.3.

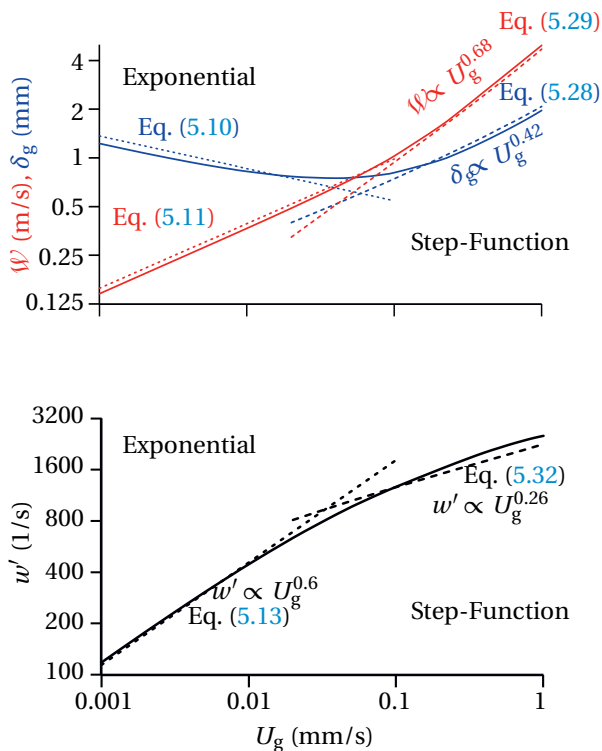


Figure 5.7: Log-log plot of \mathcal{W} , plume thickness δ_g , and shear rate w' with U_g at $z = 0.9$ m using the properties in Table 5.1. The solid line represents the numerical solution using COMSOL while the dashed lines correspond to our analytical solution. Here, we used Eq. (5.26) to solve for q numerically. We see a transition from an exponential gas fraction profile to a step-function gas fraction profile, evident from the change of slope. For a hydrogen evolution reaction, $U_g = 1$ mm/s corresponds to a current density of 8 kA/m² at atmospheric conditions.

Reference [278] observes that $w' \propto U_g^{0.64}$ for oxygen bubbles and $w' \propto U_g^{0.43}$ for hydrogen bubbles for a current density range of 0.005-0.11 A/cm². In alkaline electrolytes, oxygen bubbles are substantially larger than hydrogen bubbles [274]. Therefore, it is plausible that the oxygen gas fraction profile was approximately exponential, while the hydrogen gas fraction profile was more similar to a step function. The scaling $w' \propto U_g^{0.64}$, observed for oxygen bubbles in Ref. [278] is in agreement with $U_g^{3/5}$ derived for the exponential gas fraction profile, while the scaling $w' \propto U_g^{0.43}$ for hydrogen bubbles lies close to the range $U_g^{1/3} - U_g^{0.41}$ derived in Eq. (5.33) for the step-function gas fraction profile.

In Fig. 5.7, we observe a transition from a higher power ($w' \propto U_g^{3/5}$) to a lower power ($w' \propto U_g^{0.26}$) around $U_g \approx 0.08$ mm/s or 800 A/m², see Eq. (5.41). A similar transition from a higher power at current densities around 50 A/m² to the mentioned $w' \propto U_g^{0.43}$ was observed for hydrogen. The transition from an exponential to step-function gas fraction profile could therefore be an explanation of the increasing slope of w' with U_g observed in Ref. [278], particularly for hydrogen bubbles, even though there is a lot of scatter in the experimental data at low current density. The step-function gas fraction profile analysis will be relevant for many experimental results with small bubbles. For bigger bubbles, the exponential gas profile analysis may be more appropriate.

In Fig. 5.8, we show the natural convection electrolyte flow rate as a function of the superficial gas flux. We see that the flow rate increases as the gas flux is increased due to the presence of a larger amount of bubbles, resulting in increased buoyancy. We also see that Eq. (5.35) predicts the numerical results with good accuracy using $z = 0.4h$, in agreement with Fig. 5.11 for $l = 10$ mm.

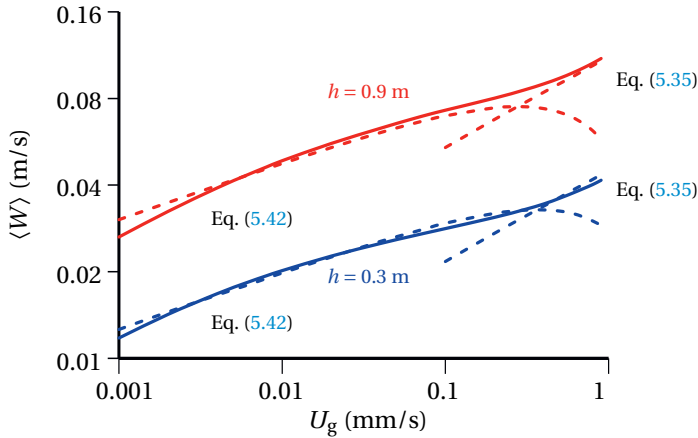


Figure 5.8: Log-log plot of the flow rate $\langle W \rangle$ with U_g for the properties listed in Table 5.1. For the step-function gas fraction profile, Eq. (5.35) valid at high U_g , we used $z_{\text{eff}} = 0.4h$ for $l = 10$ mm as indicated by Fig. 5.11(a). For the exponential gas fraction profile, Eq. (5.42) valid at small U_g , we used $z_{\text{eff}} = 0.75h$ for $l = 10$ mm as indicated by Fig. 5.11(b). It can be seen that the analytical results (dashed line) predict the flow rate with good accuracy.

For the verification of our step-function gas fraction profile results in Figs. 5.3-5.8, we used a fixed bubble diameter of 75 μm and a maximum gas fraction of 0.4. We also verified our results at a smaller bubble diameter of 50 μm and different maximum gas

fractions of 0.3, 0.4, and 0.5. We used a smaller $U_g = 0.2$ mm/s, as the maximum gas fraction is reached earlier for smaller bubble diameters due to the associated lower bubble dispersion coefficient. We summarize these results in Table 5.2 for $z = 0.9$ m. We see again a good agreement of analytical results with the numerical results obtained using COMSOL.

Table 5.2: Comparison of analytical results with numerical results obtained using COMSOL for $U_g = 0.2$ mm/s at $z = 900$ mm for a bubble diameter of 50 μ m and properties used in Table 5.1.

ϵ_0	Numerical			Analytical			Difference		
	W (m/s)	δ_g (mm)	w' (1/s)	W (mm)	δ_g (mm)	w' (1/s)	W	δ_g	w'
0.3	1.88	1.11	1693.8	1.73	1.3	1324.5	-8%	17%	-22%
0.4	1.61	0.92	1744.9	1.48	1.06	1393.6	-8%	15%	-20%
0.5	1.39	0.82	1696.1	1.29	0.93	1389.9	-8%	13%	-18%

5.5. CONCLUSIONS

In this paper, we provide analytical relations for the velocity and gas fraction profile near a gas-evolving electrode. We derived analytical expressions for quantities like flow rate and wall shear rate for natural convection conditions. These relations are derived using the integral method, assuming first an exponentially shaped gas fraction profile and then a step-function gas fraction profile with constant electrode surface gas fraction and gas flux.

As we did not use any horizontal gas transport equation in our derivation, our analytical expressions for the step-function gas fraction profile are generally valid, for any type of horizontal transport mechanism.

We found that the characteristic liquid velocity W and the gas plume thickness δ_g increase as a function of height z for both exponential ($\delta_g \propto z^{1/5}$, $W \propto z^{3/5}$) and step-function ($\delta_g \propto z^{1/3} - z^{0.43}$, $W \propto z^{2/3} - z^{0.79}$) gas fraction profiles. The exact power depends on the value of $q = \delta_f/\delta_g$, which in case of a step-function gas fraction profile depends on the gas flux and maximum gas fraction through Eq. (5.26). The characteristic liquid velocity also increases with an increase in gas flux U_g . However, with an increase in gas flux, the gas plume thickness decreases for an exponential gas fraction profile as $U_g^{-1/5}$, while it increases for a step-function gas fraction profile as $U_g^{1/3} - U_g^{0.73}$ according to Eq. (5.28). We also observed that at a given height, the velocity profiles all cross at the same point for different high current densities. This is because while the plume thickness increases, q decreases, so δ_f is almost a constant. Finally, we derived an analytical expression for the average superficial liquid velocity due to natural convection, Eq. (5.35), and validated it numerically for large current densities.

Both the exponential and step-function gas fraction profiles are relevant for water electrolyzers. Small bubbles at atmospheric pressure reach their maximum gas fraction quickly and develop a step-function gas fraction profile, while at high pressures, small heights, and/or relatively large bubbles, the gas fraction profile will be approximately exponential in shape.

APPENDICES

5.A. EXPONENTIAL GAS FRACTION PROFILE

In section 5.3.1, we provided analytical relations for an exponential-shaped gas fraction profile of Eq. (5.7). Here we provide the derivation of the provided analytical expressions. At $x = 0$, the no-slip condition gives $u = w = 0$. In our derivation, we will neglect $\varepsilon \ll 1$ in comparison to unity, so $v_m = v$ and $\frac{u_{\text{Hd}}}{1-\varepsilon/\varepsilon_{\text{max}}} \approx u_{\text{Hd}}$. Using this, we can integrate Eq. (5.4) from $x = 0$ to l with an exponential plume for $\delta_g \ll l$ to give

$$\mathcal{W} = \frac{\varepsilon_0 g \delta_g^2 q}{v(q+2)}. \quad (5.36)$$

The conservation of gas volume in Eq. (5.1) can be rewritten as

$$U_g z = H(q) \delta_g \varepsilon_0 \mathcal{W}. \quad (5.37)$$

Eq. (5.6) gives $\mathbf{u}_s \approx \mathbf{u}_{\text{St}} + \mathbf{u}_{\text{Hd}}$, so $u|_{x=0} \approx u_{\text{Hd}} \approx D_b/\delta_g$. For $\varepsilon_0 \ll 1$, we can rewrite Eq. (5.3) as

$$\frac{D_b \varepsilon_0}{\delta_g} = U_g. \quad (5.38)$$

Substituting Eq. (5.7), Eq. (5.8) and Eq. (5.36) in Eq. (5.4) and integrating between $x = 0$ and $x = l$ for $\delta_g \ll l$ gives

$$\frac{2v\mathcal{W}}{\delta_g q} = \frac{d(F(q)\delta_g \mathcal{W}^2)}{dz}, \quad (5.39)$$

where $F(q) \equiv \frac{432e^{-q} - 27e^{-2q} + 36q^3 - 162q^2 + 378q - 405}{108q^2}$. Eqs. (5.36)-(5.39) allow solutions in terms of powers of z . Eliminating ε_0 from Eqs. (5.36) and (5.37) using (5.38) gives

$$\mathcal{W} = \frac{U_g g \delta_g^3 q}{v D_b (q+2)} \quad \text{and} \quad D_b z = H(q) \delta_g^2 \mathcal{W}. \quad (5.40)$$

Eliminating \mathcal{W} from Eq. (5.40), δ_g can be calculated by Eq. (5.10). Using (5.10) in Eqs. (5.40) and (5.38), we can find \mathcal{W} and ε_0 using Eq. (5.11) and (5.12), respectively.

The exponential gas fraction profile will be relevant when the inlet gas flux U_g is small. The transition to step-function profile occurs when $\varepsilon_0 \sim \varepsilon_{\text{max}}$. We can calculate the approximate condition for the transition in terms of gas flux using Eq. (5.12) as

$$U_g \approx \left(\frac{D_b^3 \varepsilon_{\text{max}}^5 g q H(q)}{v z (q+2)} \right)^{1/4}, \quad (5.41)$$

which gives $U_g \approx 0.08$ mm/s for the properties listed in Table 5.1. We see in Fig. 5.7 that the transition to block plume indeed starts around this value.

We can estimate the superficial liquid velocity or the liquid flow rate per unit flow area, $\langle W \rangle = \frac{1}{l} \int_0^l w(1-\varepsilon) dx$, using Eqs. (5.7) and (5.8) to be

$$\langle W \rangle = \frac{\mathcal{W} \delta_g (1 - q + 0.5q^2 - e^{-q})}{ql}. \quad (5.42)$$

This expression should be evaluated at an effective height $z = z_{\text{eff}}$ for which the average liquid flow rate beyond $x = \delta_f$ is zero, which is further analyzed in 5.D.

In thermal and solutal natural convection, Eq. (5.8) is often replaced by [249, 279]:

$$w = \mathcal{W} e^{-\frac{x}{\delta_f}} \left(1 - e^{-x/\delta_g}\right), \quad (5.43)$$

which gives

$$\begin{aligned} \delta_g &= \left(\frac{\nu D_b^2 z}{g U_g} \frac{(q+1)(q+2)(2q+1)}{q^3} \right)^{1/5}, \\ \varepsilon_0 &= \left(\frac{\nu U_g^4 z}{g D_b^3} \frac{(q+1)(q+2)(2q+1)}{q^3} \right)^{1/5}, \\ \mathcal{W} &= \left(\frac{D_b g^2 U_g^2 z^3}{\nu^2} \frac{(q+1)^2 (2q+1)^2}{q^4} \right)^{1/5}, \end{aligned} \quad (5.44)$$

These expressions have the same powers of z and U_g as Eqs. (5.10)-(5.12), but depend differently on q . q , in this case, is given by

$$q \approx \sqrt{\frac{40 \text{Pr}_b}{7} \frac{1 + \sqrt{\text{Pr}_b}}{1 + 2\sqrt{\text{Pr}_b}}}. \quad (5.45)$$

BUBBLE PRANDTL NUMBER

The analytical relations derived for the exponential-shaped gas fraction profile require an estimate for q . Assuming that functions of q can be expressed as some power of q and comparing powers, we find from Eqs. (5.36)-(5.39) that $q \propto z^0$. Eq. (5.39) can be written as

$$F(q) \frac{d(\delta_g \mathcal{W}^2)}{dz} = \frac{2\nu \mathcal{W}}{q \delta_g}. \quad (5.46)$$

Differentiating Eq. (5.37) with respect to z and using the expression in Eq. (5.1) gives

$$H(q) \frac{d(\delta_g \varepsilon_0 \mathcal{W})}{dz} = U_g. \quad (5.47)$$

Dividing Eq. (5.46) by Eq. (5.47) using Eq. (5.38), we get

$$\frac{F(q)}{H(q)} \frac{\frac{d}{dz}(\delta_g \mathcal{W}^2)}{\frac{d}{dz}(\delta_g \varepsilon_0 \mathcal{W})} = \frac{2\nu \mathcal{W}}{q D_b \varepsilon_0}. \quad (5.48)$$

Using the scalings $\mathcal{W} \propto z^{3/5}$, $\delta \propto z^{1/5}$ and $\varepsilon_0 \propto z^{1/5}$ in Eq. (5.48) gives

$$\text{Pr}_b = \frac{\nu}{D_b} = \frac{7}{10} \frac{q F(q)}{H(q)}. \quad (5.49)$$

Equation (5.49) can be solved for q for a given bubble Prandtl number. An excellent approximation for all values of q with a relative error < 5% is given by Eq. (5.14).

5.B. VERIFICATION OF BOUNDARY CONDITIONS

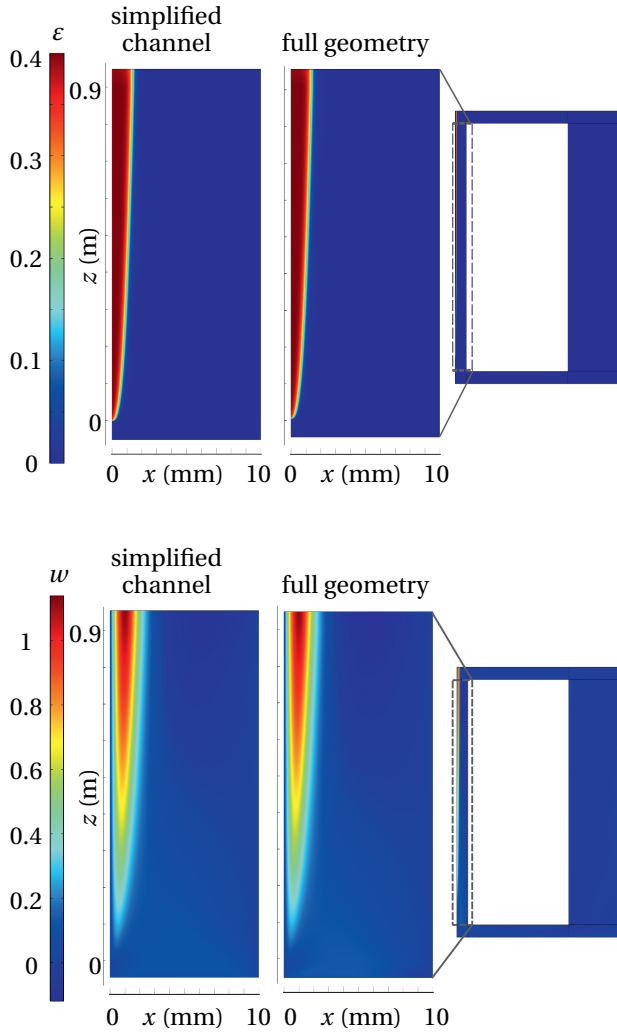


Figure 5.9: Comparison of the numerical results for (left) simplified channel geometry used in the main text and (right) the full recirculating channel geometry. The results are shown for the properties listed in Table 5.1 at a superficial gas flux of $U_g = 0.5$ mm/s. We see that both (top) the gas fraction and (bottom) the vertical velocity are similar in both cases. This shows that the boundary conditions of Fig. 5.1 are appropriate to model the natural recirculation due to the gas produced at the vertical electrode. We have resized the recirculating geometry and the boxed region is zoomed to show the comparison with the simplified channel geometry.

In this section, we verify the boundary conditions discussed in the main text and shown in the left part of Fig. 5.1 using a simulation of a full recirculation geometry including the downcomer section shown on the right of Fig. 5.1. For the full recirculation

geometry, we use the same inlet boundary condition for the electrode, such that the gas flux is equal to U_g . At the top, we use a dispersed phase outlet boundary condition, so the gas escapes from the top boundary. For the electrolyte, a slip boundary condition is used at the top boundary. At other walls, a no-slip boundary condition is imposed. From Fig. 5.9, we see that the results for the channel geometry used in the main text are similar to the full recirculating channel results, both for the gas fraction and the velocity profile with very minute differences near the top and the bottom of the channel, due to the boundary conditions. Owing to the better convergence and reduced simulation time, we used the channel geometry with the boundary conditions highlighted in Fig. 5.1.

5.C. EXPRESSIONS IN THE LIMIT $q \rightarrow 1$

In this section, we derive Eqs. (5.31), (5.33) and (5.34). For the limit $q \rightarrow 1$, the last approximation of Eq. (5.27) is given as

$$q = \left(\frac{g \varepsilon_0 v_m^2 \bar{z}_c}{z U_g^4} \right)^{(1-\varepsilon_0)^4/7} \quad (5.50)$$

where the power 0.12 correspond to $\varepsilon_0 = 0.4$ and may vary slightly between 0.11-0.14 for a different ε_0 .

To derive the scaling in the limit $q \rightarrow 1$ for δ_g , U_g and w' , we first need to locally write $\frac{q+2}{qh(q)}$, $\frac{q}{(q+2)h(q)^2}$ and $\frac{q^2}{(q+2)^2 h(q)}$ appearing in Eqs. (5.28), (5.29) and (5.32) as powers of q as

$$\left(\frac{q+2}{qh(q)} \right)^{1/3} = 2.83q^{a_1}, \quad \left(\frac{q}{(q+2)h(q)^2} \right)^{1/3} = 2.67q^{a_2}, \quad \text{and} \quad \left(\frac{q^2}{(q+2)^2 h(q)} \right)^{1/3} = 0.94q^{a_3} \quad (5.51)$$

$$\text{where } a_1 = \frac{\ln\left(\frac{q+2}{2.83^3 q h(q)}\right)}{3 \ln(q)}, \quad a_2 = \frac{\ln\left(\frac{q}{2.67^3 (q+2) h(q)^2}\right)}{3 \ln(q)} \quad \text{and} \quad a_3 = \frac{\ln\left(\frac{q^2}{0.94^3 (q+2)^2 h(q)}\right)}{3 \ln(q)}.$$

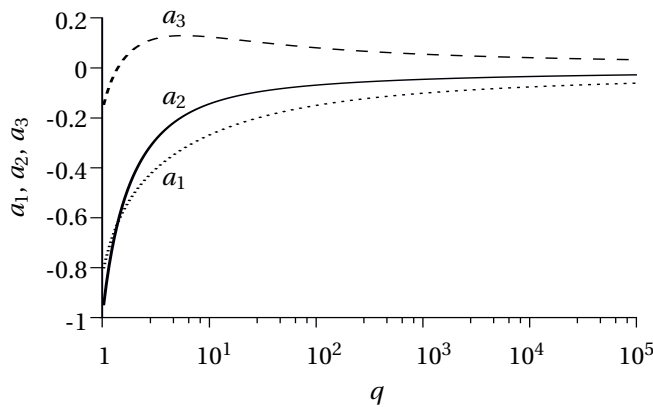


Figure 5.10: Semi-log plot showing the variation of powers a_1 , a_2 , and a_3 with q . We observe that a_1 and a_2 change monotonously with q , while a_3 has a maxima near $q \sim 5$.

In Fig. 5.10, we plot the powers a_1 , a_2 and a_3 as a function of q . We observe that a_1 and a_2 show a monotonous behavior with a finite negative value at $q = 1$ decreasing to nearly 0 at large q . In this case, both δ_g and \mathcal{W} increase as \bar{z} increases. Interestingly, a_3 increases from -0.1 to 0.13 for $q = 1 - 5$ and then decreases to 0 as q approaches infinity. In this case, we would have a local minimum in the power of U_g and z in the expression of w' . This minimum occurs when $q \sim 5$.

We can, using $a_1 = -0.8$, $a_2 = -0.95$ and $a_3 = -0.15$ and Eqs. (5.50) and (5.51), write for the limit $q \rightarrow 1$:

$$\begin{aligned} \delta_g &= 2.83 \left(\frac{zU_g^4}{g\varepsilon_0^5 v_m^2 \bar{z}_c} \right)^{0.114(1-\varepsilon_0)^{1/4}} \left(\frac{v_m U_g z}{g\varepsilon_0^2} \right)^{1/3}, \\ \mathcal{W} &= 2.67 \left(\frac{zU_g^4}{g\varepsilon_0^5 v_m^2 \bar{z}_c} \right)^{0.136(1-\varepsilon_0)^{1/4}} \left(\frac{gU_g^2 z^2}{v_m \varepsilon_0} \right)^{1/3}, \quad \text{and} \\ w' &= 0.94 \left(\frac{zU_g^4}{g\varepsilon_0^5 v_m^2 \bar{z}_c} \right)^{0.021(1-\varepsilon_0)^{1/4}} \left(\frac{g^2 U_g z \varepsilon_0}{v_m^2} \right)^{1/3}. \end{aligned} \quad (5.52)$$

which on simplification gives Eqs. (5.31) and (5.33). Similarly, the local minima in the powers of U_g and z in the expression of w' is obtained by using $a_3 = 0.13$ near $q \rightarrow 5$ in Eq. (5.50) and (5.51) to give

$$w' = 0.94 \left(\frac{g\varepsilon_0 v_m^2 \bar{z}_c}{zU_g^4} \right)^{0.019(1-\varepsilon_0)^{1/4}} \left(\frac{g^2 U_g z \varepsilon_0}{v_m^2} \right)^{1/3}. \quad (5.53)$$

resulting in Eq. (5.34) upon simplification and using $\varepsilon_0 = 0.4$.

5.D. z_{EFF}

In the main text, we used an effective height z_{eff} for which the average velocity between $\delta_f < x < l$ is negligible in simulations. In this section, we will try to quantify this height with the help of our simulations. To do this, we performed various simulations varying the current density, electrode height, channel width, and bubble diameter. In Fig. 5.11, we show the results of various simulations varying different parameters and find that the z_{eff} becomes approximately independent of the channel width for wide channels of a few cm in case of a step-function plume and a bit more in case of an exponential plume. There is some variation with bubble size, height in case of an exponential plume, and maximum gas fraction in case of a step-function plume. Except for thin channels, as a rough approximation one may take $z_{\text{eff}} \sim h/3$ for a step-function plume and $h/2$ for an exponential plume.

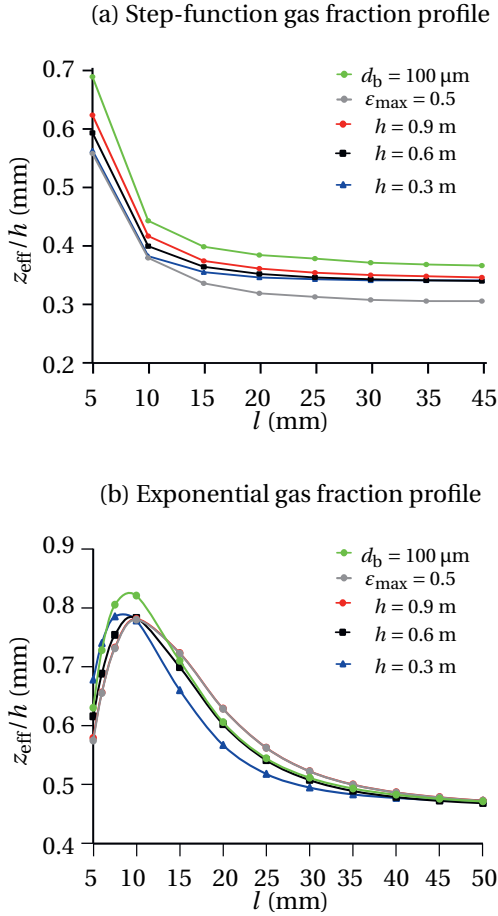


Figure 5.11: Plot showing z_{eff}/h as a function of gap width for different electrolyzer heights, maximum gas fraction, and bubble diameter. Here z_{eff} is the height for which the average superficial velocities for the analytical and numerical results are the same. Unless otherwise mentioned, the properties listed in Table 5.1 are used. These results for a step-function gas fraction profile ($U_g = 1 \text{ mm/s}$) show that z_{eff}/h becomes independent of gap width l , but depends somewhat on d_b and ε_{max} . The results for the exponential gas fraction profile ($U_g = 0.01 \text{ mm/s}$) seem to indicate that a large variation in z_{eff}/h becomes independent of l for a bit larger values. For the exponential case, the red and gray lines overlap as the gas fraction remains small, and the maximum gas fraction has no effect on the hydrodynamics.

6

SUMMARY, DISCUSSION, AND OUTLOOK

6.1. SUMMARY

This thesis attempts to improve understanding of multiphase flow in various electrochemical systems by developing new analytical models. This research focuses on four different electrochemical cell configurations, viz. :- porous gas diffusion layers in a membrane-electrode assembly; porous flow-through electrodes for membraneless operations; gas-evolving membraneless parallel plate electrolyzers; and vertical gas-evolving electrodes where the gas is produced at only one of the two parallel walls. The analytical models for each of these configurations are developed to answer the research questions outlined in section 1.3. Here we provide quick concluding remarks pertaining to the posed research questions:

"How is the limiting current in a gas diffusion layer influenced by the structure of a porous diffusion layer?": CHAPTER 2

We solved a simplified set of visco-capillary equations for the gas and liquid saturation profiles inside a porous diffusion layer when the wetting and non-wetting phases move in the opposite direction. Using the saturation profile, we derived explicit analytical expressions for effective diffusivity (Eq. (2.34)) and diffusion-limited current density (Eqs. (2.37) and (2.39)) in a porous diffusion layer. These expressions are provided in terms of geometrical parameters such as pore size distribution and thickness of the diffusion layer. These expressions show that the presence of the non-wetting phase (water in the case of fuel cells) decreases the effective diffusivity of the reacting species in the wetting phase (oxygen in the case of fuel cells) and the corresponding diffusion-limited current density.

We show through some example calculations that in modern diffusion layers, the concentration of diffusing non-wetting phase reactant remains high so that the diffusion-limited current density is well above the operating current density. As such, the performance of the membrane-electrode assembly is only marginally impacted by the porous diffusion layers, and they are well-designed for their intended operating current densities.

"What is the minimum velocity required to operate a membraneless flow-through electrolyzer effectively?": CHAPTER 3

We proposed a simple multiphase flow-through electrode model based on the visco-capillary equations introduced in chapter 2. For a membraneless operation, however, we considered the case where the gas and the liquid move in the same direction. We use the multiphase flow model to find a minimum required flow-through velocity to effectively push the gas bubbles out of the inter-electrode gap and minimize the ohmic losses. This velocity is expressed in terms of pore size distribution and thickness of the electrode (Eq. (3.5)). We show that this minimum velocity increases proportional to the square root of current density for thin electrodes and linearly with current density for thick electrodes.

"What is the maximum height of a parallel plate electrolyzer without a separator at a given operating condition using only buoyancy-driven flow?": CHAPTER 4

We used a mixture model neglecting inertia to derive approximate analytical relations for the velocity profile and the pressure drop in a parallel plate electrolyzer. We verified

these results with existing velocity profile data in the literature and our computational model.

Under the assumption that there are no external pressure losses in the system, we derived an expression for the maximum allowable height of the electrolyzer under natural convection conditions (Eq. (4.31)). We show that the buoyancy-driven flow allows a safe and efficient operation for parallel plate membraneless electrolyzers of height 5-10 cm under atmospheric conditions. We can use forced flow to make these electrolyzers taller by another 5-10 cm before turbulent mixing starts.

"How does the plume thickness, electrode surface gas fraction, and liquid velocity scale with the height and current density of the electrolyzer?": CHAPTER 5

We considered a vertical gas-evolving electrode under buoyancy-driven conditions with no gas evolution on the opposite wall. The gas fraction near the electrode keeps on increasing until it approaches a maximum value. We provide a mathematical model to simulate the multiphase flow near this maximum value. We also provide analytical relations for the gas plume thickness (Eqs. (5.10) and (5.28)), velocity profile (Eqs. (5.11) and (5.29)), and shear strain (Eqs. (5.13) and (5.32)) using the integral method and verify them using our numerical simulations. We provide these results for a gas fraction that decreases exponentially with distance from the electrode, relevant at small heights and current densities, and a step-function gas fraction profile suitable for larger heights and current densities.

We found that the plume thickness and the strain rate always increase with height. We found that the plume thickness decreases with increasing current density at small heights and current densities when the gas plume is exponential in shape. As the current density or the height increases and the gas fraction approaches its maximum value, the gas plume transitions to a step-function profile. In this case, the plume thickness increases with increasing current density.

Both these profiles are relevant for water electrolyzers. The exponential profile results are more appropriate for larger bubbles, low gas production rates, and smaller heights. Small bubbles at atmospheric pressure develop the step-function gas fraction profile quickly at high current density and height as the gas fraction approaches its maximum value.

6.2. DISCUSSIONS AND OUTLOOK

This thesis aims to create analytical models to answer important research questions about electrochemical cells, particularly water electrolyzers and fuel cells. This required us to make various simplifications and assumptions.

CHAPTER 2

The fundamental assumption in this chapter is that the gas and liquid phases individually follow Darcy's law, without mutual friction between them. This holds in a wide range of practical applications, including fuel cells and electrolyzers, in which reactants and products exist in both gaseous and liquid phases. The gas and liquid phases encounter varying degrees of transport resistance in the porous medium depending on several factors, such as the hydrophobicity of the material, pore size, and tortuosity. As a result,

gases and liquids form distinct continuous pathways in various regions of the porous diffusion layers. For example, hydrophobic diffusion layers in fuel cells allow liquids to localize in larger pores with lower threshold pressure, while the gas phase occupies smaller pores.

In this study, we assume that the phase change between the gaseous and liquid phases is neglected. Since electrochemical cells usually operate above room temperature, any evaporation leads to lower liquid saturation. Consequently, fuel cells have less liquid in the porous transport layers, leading to an underestimation of the performance of the diffusion layer. Conversely, the performance is overestimated for electrolyzers due to significant evaporation at high temperatures. Therefore, it is prudent to include phase change in future analytical models to improve their accuracy at high temperatures and predict the effect of the relative humidity of the feed gas.

We neglected the effect of Knudsen diffusivity D_k on the limiting current in our model. For very small pore sizes ($< 0.1 \mu\text{m}$) or high saturation, found in catalyst layers and some microporous layers, Knudsen diffusion also becomes important. This usually results in reduced effective diffusivity of the gas, decreasing the performance of the gas diffusion layer. This can be taken into account by writing the single phase diffusivity D_0 as $(D_m^{-1} + D_k^{-1})^{-1}$, where D_m is the molecular diffusivity.

Finally, using our analytical model, or a similar numerical model, inevitably requires information on the pore structure of the gas diffusion layers or the capillary pressure-saturation relationship in the form of Brooks-Corey relation. Although there have been many experiments to characterize diffusion layers, the data is scattered among several papers. An instrumental contribution would be creating a dynamic central database of gas diffusion layer properties that would allow researchers and industries to select the most appropriate gas diffusion layer. Only the most important properties should be included, such as porosity, permeability, electrical conductivity, thermal conductivity, contact angle, and wettability. Capillary pressure-saturation curves in the form of Brooks-Corey/Van-Genuchten relations are important for understanding the water-management behavior and should also be included in the database. This database should be searchable and allow for filtering and sorting of the data based on various parameters. The database should also include metadata such as experimental techniques used, authors and publication details. This information is critical in searching and retrieving the relevant information from the database. While creating this database is not trivial, it would help reduce the time and effort required to locate and gather relevant data from a wide range of data.

CHAPTER 3

We used the same set of visco-capillary equations as in chapter 2, so the discussion regarding phase change remains the same. Furthermore, we have introduced a free parameter in the form of the liquid saturation s_0 at the gap-electrode interface. This is influenced by flow impacting bubble nucleation and release, through drag and transport of dissolved reactants, and allowable voltage losses. For example, Ref. [15] found that s_0 could be reduced by adding a nylon spacer. The hydrophilic nature and relatively small aperture size likely give it some of the characteristics of a separator, albeit of much lower thickness and cost. The higher flow rate reduces s_0 and the corresponding overpoten-

tials as seen in Ref.[15]. It would be interesting to see the effect of electrode shape and roughness on s_0 , which should be evident from measured overpotentials.

CHAPTER 4

While deriving the analytical expressions in chapter 4, we neglected the inertial terms compared to the sum of external pressure forces and buoyancy. The velocity in our analytical model will be overestimated near the electrodes while it is underestimated in the core region of the interelectrode gap, where no or little gas is present.

There may also be some concerns regarding the slip velocity closure models used in the numerical model in chapter 4. The empirical models used in this chapter are derived from experiments conducted on rigid sedimenting particles. However, it is worth noting that these empirical relations may require additional validation, especially when used for bubbles. In particular, the expression for shear-diffusion is based on a limited dataset consisting of only three data points from a single experiment [191]. There could be some deviations in the case of charged electrochemical bubbles. In the case of electrochemical bubbles, for example, the repulsion force between bubbles is largely due to electrostatic interactions between the charges on their surfaces. This can lead to different types of behavior compared to particle collisions where the repulsion force is mostly due to collision. Furthermore, some coalescence may also occur in the case of bubbles.

The validation needed for shear diffusion or other bubble-bubble interactions could be done either numerically using direct numerical simulations or experimentally. Schillings et al. [203] attempted the direct numerical simulations and arrived at similar results as obtained using the empirical models. Similar studies can also be conducted for bubbles that may experience electrostatic repulsion or coalescence to test the validity of these empirical models for bubbles. Experimental techniques such as high-speed photography and PIV could be used to analyze the motion of bubbles and surrounding fluid and may allow the determination of bubble slip velocity.

CHAPTER 5

In our derivation of the scaling, we have assumed a velocity profile that is non-negative everywhere. As shown from our simulation, there is a negative velocity away from the electrodes. The results for flow rate will become more accurate if the same analysis can be extended to a more general velocity profile that allows negative velocities.

We have also postulated a heuristic relationship for the additional dispersion to simulate the maximum gas fraction in water electrolyzers. Such a maximum gas fraction is seen with a high concentration of the electrolyte. It would be interesting to investigate the additional dispersion mechanisms near the maximum gas fraction in more detail using techniques such as PIV and compare it with our heuristic expression.

REFERENCES

- [1] Intergovernmental Panel on Climate Change. *Global warming of 1.5° C: an IPCC special report on the impacts of global warming of 1.5° C above pre-industrial levels and related global greenhouse gas emission pathways, in the context of strengthening the global response to the threat of climate change, sustainable development, and efforts to eradicate poverty*. Intergovernmental Panel on Climate Change, 2018.
- [2] Communication from the commission to the European Parliament, The council, The European economic and social committee and the committee of the regions. *A hydrogen strategy for a climate-neutral Europe*. European Commission, 2020. URL https://ec.europa.eu/energy/sites/ener/files/hydrogen_strategy.pdf.
- [3] A. Kosturjak, T. Dey, M. Young, and S. Whetton. Advancing hydrogen: Learning from 19 plans to advance hydrogen from across the globe. *Future Fuels CRC*, 2019.
- [4] D. Gielen, E. Taibi, and R. Miranda. Hydrogen: A renewable energy perspective. *International Renewable Energy Agency (IRENA): Abu Dhabi, UAE*, 2019.
- [5] J. Rissman, C. Bataille, E. Masanet, N. Aden, W. R. Morrow III, N. Zhou, N. Elliott, R. Dell, N. Heeren, B. Huckestein, et al. Technologies and policies to decarbonize global industry: Review and assessment of mitigation drivers through 2070. *Applied Energy*, 266:114848, 2020.
- [6] S. G. Nnabuiife, J. Ugbeh-Johnson, N. E. Okeke, and C. Ogbonnaya. Present and projected developments in hydrogen production: A technological review. *Carbon Capture Science & Technology*, page 100042, 2022.
- [7] A. Körner, C. Tam, S. Bennett, and J. Gagné. Technology roadmap-hydrogen and fuel cells. *International Energy Agency (IEA): Paris, France*, 2015.
- [8] IEA (2020). Energy technology perspectives, 2020. URL <https://www.iea.org/reports/energy-technology-perspectives-2020>.
- [9] Z. Y. Yu, Y. Duan, X. Y. Feng, X. Yu, M. R. Gao, and S. H. Yu. Clean and affordable hydrogen fuel from alkaline water splitting: past, recent progress, and future prospects. *Advanced Materials*, 33(31):2007100, 2021.
- [10] L. Yu, Fand Yu, I. K. Mishra, Y. Yu, Z. F. Ren, and H. Q. Zhou. Recent developments in earth-abundant and non-noble electrocatalysts for water electrolysis. *Materials Today Physics*, 7:121–138, 2018.
- [11] I. K. Mishra, H. Zhou, J. Sun, F. Qin, K. Dahal, J. Bao, S. Chen, and Z. Ren. Hierarchical cop/ni 5 p 4/cop microsheet arrays as a robust ph-universal electrocatalyst for efficient hydrogen generation. *Energy & Environmental Science*, 11(8):2246–2252, 2018.
- [12] J. Zhang, T. Wang, P. Liu, S. Liao, Z. and Liu, Xi. Zhuang, M. Chen, E. Zschech, and X. Feng. Efficient hydrogen production on moni4 electrocatalysts with fast water dissociation kinetics. *Nature communications*, 8(1):1–8, 2017.
- [13] M. Gong, W. Zhou, M. C. Tsai, J. Zhou, M. Guan, M. C. Lin, B. Zhang, Y. Hu, D. Y. Wang, J. Yang, et al. Nanoscale nickel oxide/nickel heterostructures for active hydrogen evolution electrocatalysis. *Nature communications*, 5(1):1–6, 2014.
- [14] S. H. Ahn, S. J. Hwang, S. J. Yoo, I. Choi, H. J. Kim, J. H. Jang, S. W. Nam, T. H. Lim, T. Lim, S. K. Kim, et al. Electrodeposited ni dendrites with high activity and durability for hydrogen evolution reaction in alkaline water electrolysis. *Journal of Materials Chemistry*, 22(30):15153–15159, 2012.
- [15] H. Rajaei, A. Rajora, and J. W. Haverkort. Design of membraneless gas-evolving flow-through porous electrodes. *Journal of Power Sources*, 491:229364, 2021.
- [16] A. Rajora and J. W. Haverkort. An analytical model for liquid and gas diffusion layers in electrolyzers and fuel cells. *Journal of The Electrochemical Society*, 168(3):034506, 2021.
- [17] J. D. Fonseca, M. Camargo, J. M. Commenge, L. Falk, and I. D. Gil. Trends in design of distributed energy systems using hydrogen as energy vector: a systematic literature review. *International journal of hydrogen energy*, 44(19):9486–9504, 2019.
- [18] A. Scipioni, A. Manzardo, and J. Ren. *Hydrogen economy: supply chain, life cycle analysis and energy transition for sustainability*. Academic Press, 2017.
- [19] T. Wilberforce, Z. El-Hassan, F. N. Khatib, A. Al Makky, A. Baroutaji, J. G. Carton, J. Thompson, and A. G.

- Olabi. Modelling and simulation of proton exchange membrane fuel cell with serpentine bipolar plate using matlab. *international journal of hydrogen energy*, 42(40):25639–25662, 2017.
- [20] J. Shin, W. S. Hwang, and H. Choi. Can hydrogen fuel vehicles be a sustainable alternative on vehicle market?: Comparison of electric and hydrogen fuel cell vehicles. *Technological Forecasting and Social Change*, 143:239–248, 2019.
- [21] P. Tiwari, G. Tsekouras, K. Wagner, G. F. Swiegers, and G. G. Wallace. A new class of bubble-free water electrolyzer that is intrinsically highly efficient. *International Journal of Hydrogen Energy*, 44(42):23568–23579, 2019.
- [22] D. L. Fritz, J. Mergel, and D. Stolten. PEM electrolysis simulation and validation. *Ecs Transactions*, 58(19):1–9, 2014.
- [23] E. T. Ojong, J. T. H. Kwan, A. N. Khorasani, A. Bonakdarpour, D. P. Wilkinson, and T. Smolinka. Development of an experimentally validated semi-empirical fully-coupled performance model of a PEM electrolysis cell with a 3-d structured porous transport layer. *International journal of hydrogen energy*, 42(41):25831–25847, 2017.
- [24] C. H. Lee, R. Banerjee, F. Arbabi, J. Hinebaugh, and A. Bazylak. Porous transport layer related mass transport losses in polymer electrolyte membrane electrolysis: a review. In *International Conference on Nanochannels, Microchannels, and Minichannels*, volume 50343, page V001T07A003. American Society of Mechanical Engineers, 2016.
- [25] M. Zlobinski, T. Schuler, F. N. Büchi, T. J. Schmidt, and P. Boilat. Transient and steady state two-phase flow in anodic porous transport layer of proton exchange membrane water electrolyzer. *Journal of The Electrochemical Society*, 167(8):084509, 2020.
- [26] J. Garcia-Navarro, M. Schulze, and K. A. Friedrich. Understanding the role of water flow and the porous transport layer on the performance of proton exchange membrane water electrolyzers. *ACS Sustainable Chemistry & Engineering*, 7(1):1600–1610, 2018.
- [27] P. Trinke, G. P. Keeley, M. Carmo, B. Benschmann, and R. Hanke-Rauschenbach. Elucidating the effect of mass transport resistances on hydrogen crossover and cell performance in pem water electrolyzers by varying the cathode ionomer content. *Journal of The Electrochemical Society*, 166(8):F465, 2019.
- [28] B. A. Braz, V. B. Oliveira, and A. M. F. R. Pinto. Experimental studies of the effect of cathode diffusion layer properties on a passive direct methanol fuel cell power output. *International Journal of Hydrogen Energy*, 2019.
- [29] G. Zhang and K. Jiao. Multi-phase models for water and thermal management of proton exchange membrane fuel cell: a review. *Journal of Power Sources*, 391:120–133, 2018.
- [30] X. Liu, F. Peng, G. Lou, and Z. Wen. Liquid water transport characteristics of porous diffusion media in polymer electrolyte membrane fuel cells: A review. *Journal of Power Sources*, 299:85–96, 2015.
- [31] A. H. A. Rahim, A. S. Tijani, S. K. Kamarudin, and S. Hanapi. An overview of polymer electrolyte membrane electrolyzer for hydrogen production: Modeling and mass transport. *Journal of Power Sources*, 309:56–65, 2016.
- [32] A. Zinser, G. Papakonstantinou, and K. Sundmacher. Analysis of mass transport processes in the anodic porous transport layer in PEM water electrolyzers. *International Journal of Hydrogen Energy*, 44(52):28077–28087, 2019.
- [33] G. Schmidt, M. Suermann, B. Benschmann, R. Hanke-Rauschenbach, and I. Neuweiler. Modeling overpotentials related to mass transport through porous transport layers of pem water electrolysis cells. *Journal of the Electrochemical Society*, 2020.
- [34] T. E. Lipman and A. Z. Weber. *Fuel cells and hydrogen production: A volume in the Encyclopedia of sustainability science and technology*. Springer, 2019.
- [35] A. Z. Weber and J. Newman. Effects of microporous layers in polymer electrolyte fuel cells. *Journal of the Electrochemical Society*, 152(4):A677–A688, 2005.
- [36] A. G. Stern. A new sustainable hydrogen clean energy paradigm. *International Journal of Hydrogen Energy*, 43(9):4244–4255, 2018.
- [37] T. Shinagawa and K. Takanabe. Towards versatile and sustainable hydrogen production through electrocatalytic water splitting: electrolyte engineering. *ChemSusChem*, 10(7):1318–1336, 2017.
- [38] T. J. Jacobsson, V. Fjällström, M. Edoff, and T. Edvinsson. Sustainable solar hydrogen production: from photoelectrochemical cells to pv-electrolyzers and back again. *Energy & Environmental Science*, 7(7):2056–2070, 2014.
- [39] H. R. Corti and E. R. Gonzalez. Direct alcohol fuel cells. *Materials, Performance, Durability and Applications Introduction to Direct Alcohol Fuel Cells ed Horacio R. Corti and Ernesto R. Gonzalez (New York: Springer) p*, 1, 2014.

- [40] G. Deng, L. Liang, C. Li, J. Ge, C. Liu, Z. Jin, and W. Xing. Mass transport in anode gas diffusion layer of direct methanol fuel cell derived from compression effect. *Journal of Power Sources*, 427:120–128, 2019.
- [41] P. Joghee, J. N. Malik, S. Pilypenko, and R. O'Hayre. A review on direct methanol fuel cells—in the perspective of energy and sustainability. *MRS Energy & Sustainability*, 2:E3, 2015.
- [42] W. W. Yang, M. Y. Lu, and Y. L. He. Performance study of an alkaline direct ethanol fuel cell with a reduced two-dimensional mass transport model. *Int. J. Hydrogen Energy*, 41(45):20693–20708, 2016.
- [43] S. P. S. Badwal, S. Giddey, A. Kulkarni, J. Goel, and S. Basu. Direct ethanol fuel cells for transport and stationary applications—a comprehensive review. *Applied Energy*, 145:80–103, 2015.
- [44] S. Huo and K. Jiao. Mathematical modeling of alkaline anion exchange membrane fuel cells. In *Anion Exchange Membrane Fuel Cells*, pages 169–215. Springer, 2018.
- [45] F. Kubannek, T. Turek, and U. Krewer. Modeling oxygen gas diffusion electrodes for various technical applications. *Chemie Ingenieur Technik*, 91(6):720–733, 2019.
- [46] B. De Mot, J. Hereijgers, M. Duarte, and T. Breugelmans. Influence of flow and pressure distribution inside a gas diffusion electrode on the performance of a flow-by CO₂ electrolyzer. *Chemical Engineering Journal*, 378:122224, 2019.
- [47] L. C. Weng, A. T. Bell, and A. Z. Weber. Modeling gas-diffusion electrodes for CO₂ reduction. *Physical Chemistry Chemical Physics*, 20(25):16973–16984, 2018.
- [48] T. Burdyny and W. A. Smith. CO₂ reduction on gas-diffusion electrodes and why catalytic performance must be assessed at commercially-relevant conditions. *Energy & Environmental Science*, 12(5):1442–1453, 2019.
- [49] U. Pasaogullari and C. Y. Wang. Two-phase transport and the role of micro-porous layer in polymer electrolyte fuel cells. *Electrochimica Acta*, 49(25):4359–4369, 2004.
- [50] S. Litster and N. Djilali. Two-phase transport in porous gas diffusion electrodes. *Developments in Heat Transfer*, 19:175, 2005.
- [51] Y. S. Wu. *Multiphase fluid flow in porous and fractured reservoirs*. Gulf professional publishing, 2015.
- [52] G. F. Pinder and W. G. Gray. *Essentials of multiphase flow and transport in porous media*. John Wiley & Sons, 2008.
- [53] S. Huo, K. Jiao, and J. W. Park. On the water transport behavior and phase transition mechanisms in cold start operation of PEM fuel cell. *Applied energy*, 233:776–788, 2019.
- [54] M. T. Van Genuchten. A closed-form equation for predicting the hydraulic conductivity of unsaturated soils 1. *Soil science society of America journal*, 44(5):892–898, 1980.
- [55] R. H. Brooks and A. T. Corey. Hydraulic properties of porous media. *Hydrology papers (Colorado State University); no. 3*, 1964.
- [56] B. Xiao, W. Wang, X. Zhang, G. Long, H. Chen, H. Cai, and L. Deng. a novel fractal model for relative permeability of gas diffusion layer in proton exchange membrane fuel cell with capillary pressure effect. *Fractals*, 27, 2019.
- [57] Y. Shi, S. Cheng, and S. Quan. Fractal-based theoretical model on saturation and relative permeability in the gas diffusion layer of polymer electrolyte membrane fuel cells. *Journal of Power Sources*, 209:130–140, 2012.
- [58] J. Kim, G. Luo, and C. Y. Wang. Modeling liquid water re-distributions in bi-porous layer flow-fields of proton exchange membrane fuel cells. *Journal of Power Sources*, 400:284–295, 2018.
- [59] V. Gurau and J. A. Mann Jr. Effect of interfacial phenomena at the gas diffusion layer-channel interface on the water evolution in a PEMFC. *Journal of The Electrochemical Society*, 157(4):B512, 2010.
- [60] J. Roth. *Water transport in gas diffusion media for PEM fuel cells: experimental and numerical investigation*. PhD thesis, Duisburg-Essen University, 2010.
- [61] Y. Cengel. *Heat and mass transfer: fundamentals and applications*. McGraw-Hill Higher Education, 2014.
- [62] W. G. Bessler. Gas concentration impedance of solid oxide fuel cell anodes: I. stagnation point flow geometry. *Journal of The Electrochemical Society*, 153(8):A1492, 2006.
- [63] N. W. Lee, Y. S. Kim, M. Kim, and M. S. Kim. Numerical analysis on the effect of voltage change on removing condensed water inside the gdl of a pem fuel cell. *Journal of Mechanical Science and Technology*, 30(9):4383–4390, 2016.
- [64] M. R. J. Wyllie and M. B. Spangler. Application of electrical resistivity measurements to problem of fluid flow in porous media. *AAPG Bulletin*, 36(2):359–403, 1952.
- [65] K. Nakornthap, R. D. Evans, et al. Temperature-dependent relative permeability and its effect on oil displacement by thermal methods. *SPE Reservoir Engineering*, 1(03):230–242, 1986.
- [66] C. C. Huet. *Semi-analytical estimates of permeability obtained from capillary pressure*. PhD thesis, Texas

- A&M University, 2006.
- [67] J. Kozeny. Über kapillare leitung der wasser in boden. *Royal Academy of Science, Vienna, Proc. Class I*, 136:271–306, 1927.
- [68] D. Muirhead, R. Banerjee, M. G. George, N. Ge, P. Shrestha, H. Liu, J. Lee, and A. Bazylak. Liquid water saturation and oxygen transport resistance in polymer electrolyte membrane fuel cell gas diffusion layers. *Electrochimica Acta*, 274:250–265, 2018.
- [69] J. Lee, R. Yip, P. Antonacci, N. Ge, T. Kotaka, Y. Tabuchi, and A. Bazylak. Synchrotron investigation of microporous layer thickness on liquid water distribution in a pem fuel cell. *Journal of The Electrochemical Society*, 162(7):F669, 2015.
- [70] L. An, T. S. Zhao, Z. H. Chai, P. Tan, and L. Zeng. Mathematical modeling of an anion-exchange membrane water electrolyzer for hydrogen production. *international journal of hydrogen energy*, 39(35):19869–19876, 2014.
- [71] B. Han, J. Mo, Z. Kang, G. Yang, W. Barnhill, and F. Y. Zhang. Modeling of two-phase transport in proton exchange membrane electrolyzer cells for hydrogen energy. *International Journal of Hydrogen Energy*, 42(7):4478–4489, 2017.
- [72] X. Wang and T. V. Nguyen. Modeling the effects of capillary property of porous media on the performance of the cathode of a PEMFC. *Journal of The Electrochemical Society*, 155(11):B1085–B1092, 2008.
- [73] J. H. Nam, K. J. Lee, G. S. Hwang, C. J. Kim, and M. Kaviany. Microporous layer for water morphology control in PEMFC. *International Journal of Heat and Mass Transfer*, 52(11-12):2779–2791, 2009.
- [74] S. A. Grigoriev, A. A. Kalinnikov, P. Millet, V. I. Porembsky, and V. N. Fateev. Mathematical modeling of high-pressure PEM water electrolysis. *Journal of applied electrochemistry*, 40(5):921–932, 2010.
- [75] J. W. Haverkort. A theoretical analysis of the optimal electrode thickness and porosity. *Electrochimica Acta*, 295:846–860, 2019.
- [76] J. Herranz, J. Durst, E. Fabbri, A. Patru, X. Cheng, A. A. Permyakova, and T. J. Schmidt. Interfacial effects on the catalysis of the hydrogen evolution, oxygen evolution and CO₂-reduction reactions for (co-) electrolyzer development. *Nano Energy*, 29:4–28, 2016.
- [77] F. Marangio, M. Santarelli, and M. Cali. Theoretical model and experimental analysis of a high pressure pem water electrolyser for hydrogen production. *International journal of hydrogen energy*, 34(3):1143–1158, 2009.
- [78] Z. Kang, S. M. Alia, J. L. Young, and G. Bender. Effects of various parameters of different porous transport layers in proton exchange membrane water electrolysis. *Electrochimica Acta*, page 136641, 2020.
- [79] F. Ahmadi and R. Roshandel. Effects of microhydrophobic porous layer on water distribution in polymer electrolyte membrane fuel cells. *Journal of Fuel Cell Science and Technology*, 11(1), 2014.
- [80] R. Wu, Q. Liao, X. Zhu, and H. Wang. Liquid and oxygen transport through bilayer gas diffusion materials of proton exchange membrane fuel cells. *International journal of heat and mass transfer*, 55(23-24):6363–6373, 2012.
- [81] A. Z. Weber. Improved modeling and understanding of diffusion-media wettability on polymer-electrolyte-fuel-cell performance. *Journal of Power Sources*, 195(16):5292–5304, 2010.
- [82] A. Z. Weber and J. Newman. Modeling transport in polymer-electrolyte fuel cells. *Chemical reviews*, 104(10):4679–4726, 2004.
- [83] J. H. Nam and M. Kaviany. Effective diffusivity and water-saturation distribution in single-and two-layer PEMFC diffusion medium. *International Journal of Heat and Mass Transfer*, 46(24):4595–4611, 2003.
- [84] Y. Wang and S. Wang. Evaluation and modeling of PEM fuel cells with the bruggeman correlation under various tortuosity factors. *International Journal of Heat and Mass Transfer*, 105:18–23, 2017.
- [85] G. S. Hwang and A. Z. Weber. Effective-diffusivity measurement of partially-saturated fuel-cell gas-diffusion layers. *Journal of The Electrochemical Society*, 159(11):F683–F692, 2012.
- [86] T.G. Tranter, P. Boillat, A. Mularczyk, V. Manzi-Orezzoli, P. R. Shearing, D. Brett, J. Eller, J. Gostick, and A. Forner-Cuenca. Pore network modelling of capillary transport and relative diffusivity in gas diffusion layers with patterned wettability. *Journal of the Electrochemical Society*, 2020.
- [87] J. T. Gostick, M. W. Fowler, M. A. Ioannidis, M. D. Pritzker, Y. M. Volfkovich, and A. Sakars. Capillary pressure and hydrophilic porosity in gas diffusion layers for polymer electrolyte fuel cells. *Journal of power sources*, 156(2):375–387, 2006.
- [88] A. El-Kharouf, T. J. Mason, D. J. L. Brett, and B. G. Pollet. Ex-situ characterisation of gas diffusion layers for proton exchange membrane fuel cells. *Journal of Power Sources*, 218:393–404, 2012.
- [89] S. A. Grigoriev, P. Millet, S. A. Volobuev, and V. N. Fateev. Optimization of porous current collectors for PEM water electrolyzers. *International journal of hydrogen energy*, 34(11):4968–4973, 2009.
- [90] J. Becker, C. Wieser, S. Fell, and K. Steiner. A multi-scale approach to material modeling of fuel cell

- diffusion media. *International Journal of Heat and Mass Transfer*, 54(7-8):1360–1368, 2011.
- [91] X. Zhang, Y. Gao, H. Ostadi, K. Jiang, and R. Chen. Modelling water intrusion and oxygen diffusion in a reconstructed microporous layer of pem fuel cells. *International journal of hydrogen energy*, 39(30): 17222–17230, 2014.
- [92] D. Qiu, H. Janßen, L. Peng, P. Irmscher, X. Lai, and W. Lehnert. Electrical resistance and microstructure of typical gas diffusion layers for proton exchange membrane fuel cell under compression. *Applied Energy*, 231:127–137, 2018.
- [93] A. B. D. Cassie and S. Baxter. Wettability of porous surfaces. *Transactions of the Faraday society*, 40: 546–551, 1944.
- [94] J. Fishman, H. Leung, and A. Bazylak. Droplet pinning by pem fuel cell gdl surfaces. *International journal of hydrogen energy*, 35(17):9144–9150, 2010.
- [95] H. Vogt. The actual current density of gas-evolving electrodes—notes on the bubble coverage. *Electrochimica acta*, 78:183–187, 2012.
- [96] Y. M. Volkovich, E. I. Shkolnikov, V. S. Dubasova, and V. A. Ponomarev. Development of methods for the investigation of porous structures and establishment of the nature of their influence on the macrokinetics of processes in gas-diffusion electrodes. *Soviet Electrochemistry*, 19(6):681–688, 1983.
- [97] J Newman and W Tiedman. by h. gerischer, c. w. tobias. *Advances in Electrochemistry and Electrochemical Engineering*, ed. by H. Gerischer, CW Tobias, Wiley, New York, 11:352–438, 1978.
- [98] D. Pletcher, N. A. Hampson, and A. J. S. McNeil. The electrochemistry of porous electrodes: Flow-through and three-phase electrodes. In *Electrochemistry*, pages 1–65. 1984.
- [99] C. Oloman. Trickle bed electrochemical reactors. *Journal of the Electrochemical Society*, 126(11):1885–1892, 1979.
- [100] C. L. K. Tennakoon, R. C. Bhardwaji, and J. Bockris. Electrochemical treatment of human wastes in a packed bed reactor. *Journal of applied electrochemistry*, 26(1):18–29, 1996.
- [101] K. Kinoshita and S. C. Leach. Mass-transfer study of carbon felt, flow-through electrode. *Journal of The Electrochemical Society*, 129(9):1993–1997, 1982.
- [102] X. Ke, J. M. Prah, J. I. D. Alexander, J. S. Wainright, T. A. Zawodzinski, and R. F. Savinell. Rechargeable redox flow batteries: flow fields, stacks and design considerations. *Chemical Society Reviews*, 47(23): 8721–8743, 2018.
- [103] M. E. Suss, K. Conforti, L. Gilson, C. R. Buie, and M. Z. Bazant. Membraneless flow battery leveraging flow-through heterogeneous porous media for improved power density and reduced crossover. *RSC Advances*, 6(102):100209–100213, 2016.
- [104] J. Wang and H. D. Dewald. Deposition of metals at a flow-through reticulated vitreous carbon electrode coupled with on-line monitoring of the effluent. *Journal of The Electrochemical Society*, 130(9):1814–1818, 1983.
- [105] J. M. Bisang. Theoretical and experimental studies of the effect of side reactions in copper deposition from dilute solutions on packed-bed electrodes. *Journal of applied electrochemistry*, 26(2):135–142, 1996.
- [106] A. K. P. Chu, M. Fleischmann, and G. J. Hills. Packed bed electrodes. i. the electrochemical extraction of copper ions from dilute aqueous solutions. *Journal of Applied Electrochemistry*, 4(4):323–330, 1974.
- [107] C. S. Hofseth and T. W. Chapman. Electrochemical destruction of dilute cyanide by copper-catalyzed oxidation in a flow-through porous electrode. *Journal of The Electrochemical Society*, 146(1):199–207, 1999.
- [108] S. P. Ho, Y. Y. Wang, and C. C. Wan. Electrolytic decomposition of cyanide effluent with an electrochemical reactor packed with stainless steel fiber. *Water Research*, 24(11):1317–1321, 1990.
- [109] B. G. Ateya and E. S. Arafat. Applications of porous flow-through electrodes: I. an experimental study on the hydrogen evolution reaction on packed bed electrodes. *Journal of the Electrochemical Society*, 130(2):380, 1983.
- [110] M. I. Gillespie, F. Van der Merwe, and R. J. Kriek. Performance evaluation of a membraneless divergent electrode-flow-through (deft) alkaline electrolyser based on optimisation of electrolytic flow and electrode gap. *Journal of Power Sources*, 293:228–235, 2015.
- [111] M. I. Gillespie and R. J. Kriek. Hydrogen production from a rectangular horizontal filter press divergent electrode-flow-through (deft) alkaline electrolysis stack. *Journal of Power Sources*, 372:252–259, 2017.
- [112] M. I. Gillespie and R. J. Kriek. Scalable hydrogen production from a mono-circular filter press divergent electrode-flow-through alkaline electrolysis stack. *Journal of Power Sources*, 397:204–213, 2018.
- [113] F. Yang, M. J. Kim, M. Brown, and B. J. Wiley. Alkaline water electrolysis at 25 a cm⁻² with a microfibrous flow-through electrode. *Advanced Energy Materials*, 10(25):2001174, 2020.

- [114] L. F. Arenas, C. P. de León, and F. C. Walsh. Critical review—the versatile plane parallel electrode geometry: an illustrated review. *Journal of The Electrochemical Society*, 167(2):023504, 2020.
- [115] J. A. Trainham and J. Newman. A comparison between flow-through and flow-by porous electrodes for redox energy storage. *Electrochimica Acta*, 26(4):455–469, 1981.
- [116] P. S. Fedkiw. Ohmic potential drop in flow-through and flow-by porous electrodes. *Journal of the Electrochemical Society*, 128(4):831–838, 1981.
- [117] L. Joerissen, J. Garche, C. Fabjan, and G. Tomazic. Possible use of vanadium redox-flow batteries for energy storage in small grids and stand-alone photovoltaic systems. *Journal of power sources*, 127(1-2): 98–104, 2004.
- [118] P. Boissonneau, Pand Byrne. An experimental investigation of bubble-induced free convection in a small electrochemical cell. *Journal of Applied Electrochemistry*, 30(7):767–775, 2000.
- [119] J. S. Hur, C. B. Shin, H. Kim, and Y. S. Kwon. Modeling of the trajectories of the hydrogen bubbles in a fluorine production cell. *Journal of the Electrochemical Society*, 150(3):D70, 2003.
- [120] Y. Chen, N. S. Lewis, and C. Xiang. Modeling the performance of a flow-through gas diffusion electrode for electrochemical reduction of co or co₂. *Journal of The Electrochemical Society*, 167(11):114503, 2020.
- [121] P. Haug, M. Koj, and T. Turek. Influence of process conditions on gas purity in alkaline water electrolysis. *International Journal of Hydrogen Energy*, 42(15):9406–9418, 2017.
- [122] P. Trinke, P. Haug, J. Brauns, B. Bensmann, R. Hanke-Rauschenbach, and T. Turek. Hydrogen crossover in pem and alkaline water electrolysis: mechanisms, direct comparison and mitigation strategies. *Journal of The Electrochemical Society*, 165(7):F502, 2018.
- [123] J. W. Haverkort and H. Rajaei. Electro-osmotic flow and the limiting current in alkaline water electrolysis. *Journal of Power Sources Advances*, 6:100034, 2020.
- [124] J. T. Davis, J. Qi, X. Fan, J. C. Bui, and D. V. Esposito. Floating membraneless pv-electrolyzer based on buoyancy-driven product separation. *International Journal of Hydrogen Energy*, 43(3):1224–1238, 2018.
- [125] S. M. H. Hashemi, P. Karnakov, P. Hadikhani, E. Chinello, S. Litvinov, C. Moser, P. Koumoutsakos, and D. Psaltis. A versatile and membrane-less electrochemical reactor for the electrolysis of water and brine. *Energy & Environmental Science*, 2019.
- [126] B. E. El-Anadouli, M. M. Khader, M. M. Saleh, and B. G. Ateya. Application of porous flow through electrodes: Iv. hydrogen evolution on packed bed electrodes of iron spheres in flowing alkaline solutions. *Journal of applied electrochemistry*, 21(2):166–169, 1991.
- [127] M. M. Saleh. Simulation of oxygen evolution reaction at porous anode from flowing electrolytes. *Journal of Solid State Electrochemistry*, 11(6):811–820, 2007.
- [128] D. V. Esposito. Membraneless electrolyzers for low-cost hydrogen production in a renewable energy future. *Joule*, 1(4):651–658, 2017.
- [129] G. D. O’Neil, C. D. Christian, D. E. Brown, and D. V. Esposito. Hydrogen production with a simple and scalable membraneless electrolyzer. *Journal of The Electrochemical Society*, 163(11):F3012, 2016.
- [130] R. M. Perskaya and I. A. Zaidenman. On liquid diffusion electrodes. In *Doklady Akademii Nauk*, volume 115, pages 548–551. Russian Academy of Sciences, 1957.
- [131] M. Paulin, D. Hutin, and F. Coeuret. Theoretical and experimental study of flow-through porous electrodes. *Journal of the Electrochemical Society*, 124(2):180, 1977.
- [132] M. M. Saleh. On the effectiveness factor of flow-through porous electrodes. *The Journal of Physical Chemistry B*, 108(35):13419–13426, 2004.
- [133] M. M. Saleh. Mathematical modeling of gas evolving flow-through porous electrodes. *Electrochimica acta*, 45(6):959–967, 1999.
- [134] B. G. Ateya and B. E. El-Anadouli. Effects of gas bubbles on the polarization behavior of porous flow through electrodes. *Journal of The Electrochemical Society*, 138(5):1331–1336, 1991.
- [135] B. E. El-Anadouli and B. G. Ateya. Effects of gas bubbles on the current and potential profiles within porous flow-through electrodes. *Journal of applied electrochemistry*, 22(3):277–284, 1992.
- [136] M. M. Saleh, J. W. Weidner, and B. G. Ateya. Electrowinning of non-noble metals with simultaneous hydrogen evolution at flow-through porous electrodes i. theoretical. *Journal of The Electrochemical Society*, 142(12):4113–4121, 1995.
- [137] M. S. El-Deab, M. E. El-Shakre, B. E. El-Anadouli, and B. G. Ateya. Electrolytic generation of hydrogen on pt-loaded porous graphite electrodes from flowing alkaline solutions. *Journal of applied electrochemistry*, 26(11):1133–1137, 1996.
- [138] P. Bumroongsakulsawat and G. H. Kelsall. Tinned graphite felt cathodes for scale-up of electrochemical reduction of aqueous co₂. *Electrochimica Acta*, 159:242–251, 2015.
- [139] M. Ahmadlouydarab, Z. S. S. Liu, and J. J. Feng. Relative permeability for two-phase flow through corru-

- gated tubes as model porous media. *International journal of multiphase flow*, 47:85–93, 2012.
- [140] R. Alkire and B. Gracon. Flow-through porous electrodes. *Journal of the Electrochemical Society*, 122(12):1594, 1975.
- [141] T. Risch and J. Newman. A theoretical comparison of flow-through and flow-by porous electrodes at the limiting current. *Journal of the Electrochemical Society*, 131(11):2551, 1984.
- [142] S. Shibata. The concentration of molecular hydrogen on the platinum cathode. *Bulletin of the Chemical Society of Japan*, 36(1):53–57, 1963.
- [143] H. Vogt. The concentration overpotential of gas evolving electrodes as a multiple problem of mass transfer. *Journal of The Electrochemical Society*, 137(4):1179, 1990.
- [144] J. A. Leistra and P. J. Sides. Hyperpolarization at gas evolving electrodes—ii. hall/heroult electrolysis. *Electrochimica acta*, 33(12):1761–1766, 1988.
- [145] M. M. Bakker and D. A. Vermaas. Gas bubble removal in alkaline water electrolysis with utilization of pressure swings. *Electrochimica Acta*, 319:148–157, 2019.
- [146] J. Y. Moon and B. J. Chung. Simulation of pool boiling regimes for a sphere using a hydrogen evolving system. *International Journal of Heat and Mass Transfer*, 151:119441, 2020.
- [147] J. W. Haverkort. Modeling and experiments of binary electrolytes in the presence of diffusion, migration, and electro-osmotic flow. *Physical Review Applied*, 14(4):044047, 2020.
- [148] A. E. Saez and R. G. Carbonell. hydrodynamic parameters for gas-liquid cocurrent flow in packed beds. *AIChE Journal*, 31(1):52–62, 1985.
- [149] J. Tosoni, J. C. Baudez, and R. Girault. Effect of operating parameters on the dewatering performance of press filters: A sensitivity analysis. *Drying technology*, 33(11):1327–1338, 2015.
- [150] A. D. Stickland, E. H. Irvin, S. J. Skinner, P. J. Scales, A.w Hawkey, and F. Kaswalder. Filter press performance for fast-filtering compressible suspensions. *Chemical Engineering & Technology*, 39(3):409–416, 2016.
- [151] R. Phillips and C. W. Dunnill. Zero gap alkaline electrolysis cell design for renewable energy storage as hydrogen gas. *RSC Advances*, 6(102):100643–100651, 2016.
- [152] D. Le Bideau, P. Mandin, M. Benbouzid, M. Kim, and M. Sellier. Review of necessary thermophysical properties and their sensitivities with temperature and electrolyte mass fractions for alkaline water electrolysis multiphysics modelling. *International Journal of Hydrogen Energy*, 44(10):4553–4569, 2019.
- [153] D. A. G. Bruggeman. The calculation of various physical constants of heterogeneous substances. i. the dielectric constants and conductivities of mixtures composed of isotropic substances. *Annals of Physics*, 416:636–791, 1935.
- [154] Y. Wang, S. Wang, S. Liu, H. Li, and K. Zhu. Three-dimensional simulation of a pem fuel cell with experimentally measured through-plane gas effective diffusivity considering knudsen diffusion and the liquid water effect in porous electrodes. *Electrochimica Acta*, 318:770–782, 2019.
- [155] L. G. Austin. Tafel slopes for flooded diffusion electrodes. *Transactions of the Faraday Society*, 60:1319–1324, 1964.
- [156] K. Scott. Short communication the effectiveness of particulate bed electrodes under activation control. *Electrochimica Acta*, 27(3):447–451, 1982.
- [157] A. Rajora and J. W. Haverkort. An analytical multiphase flow model for parallel plate electrolyzers. *Chemical Engineering Science*, 260:117823, 2022.
- [158] G. D. O’Neil, C. D. Christian, D. E. Brown, and D. V. Esposito. Hydrogen production with a simple and scalable membraneless electrolyzer. *Journal of The Electrochemical Society*, 163(11):F3012, 2016.
- [159] P. Millet, R. Ngameni, S. A. Grigoriev, and V. N. Fateev. Scientific and engineering issues related to pem technology: Water electrolyzers, fuel cells and unitized regenerative systems. *International journal of hydrogen energy*, 36(6):4156–4163, 2011.
- [160] W. Tong, M. Forster, F. Dionigi, S. Dresp, R. S. Erami, P. Strasser, A. J. Cowan, and P. Farràs. Electrolysis of low-grade and saline surface water. *Nature Energy*, 5(5):367–377, 2020.
- [161] K. Obata, A. Mokeddem, and F. F. Abdi. Multiphase fluid dynamics simulations of product crossover in solar-driven, membrane-less water splitting. *Cell Reports Physical Science*, page 100358, 2021.
- [162] S. M. H. Hashemi, M. A. Modestino, and D. Psaltis. A membrane-less electrolyzer for hydrogen production across the ph scale. *Energy & Environmental Science*, 8(7):2003–2009, 2015.
- [163] P. Hadikhani, S. M. H. Hashemi, S. A. Schenk, and D. Psaltis. A membrane-less electrolyzer with porous walls for high throughput and pure hydrogen production. *Sustainable energy & fuels*, 5(9):2419–2432, 2021.
- [164] I. Holmes-Gentle, F. Hoffmann, C. A. Mesa, and K. Hellgardt. Membrane-less photoelectrochemical cells: product separation by hydrodynamic control. *Sustainable Energy & Fuels*, 1(5):1184–1198, 2017.

- [165] X. Pang, J. T. Davis, A. D. Harvey, and D. V. Esposito. Framework for evaluating the performance limits of membraneless electrolyzers. *Energy & Environmental Science*, 13(10):3663–3678, 2020.
- [166] I. Kuroda, A. Sakakibara, T. Sasaki, Y. Murai, N. Nagai, and F. Yamamoto. Piv study on buoyant bubble flows in a small electrolytic cell. *Japanese Journal of Multiphase Flow*, 22(2):161–174, 2008.
- [167] R. Hreiz, L. Abdelouahed, D.s Fuenfschilling, and F. Lapique. Electrogenerated bubbles induced convection in narrow vertical cells: Piv measurements and euler–lagrange cfd simulation. *Chemical Engineering Science*, 134:138–152, 2015.
- [168] K. Aldas, N. Pehlivanoglu, and M. D. Mat. Numerical and experimental investigation of two-phase flow in an electrochemical cell. *International journal of hydrogen energy*, 33(14):3668–3675, 2008.
- [169] H. Riegel, J. Mitrovic, and K. Stephan. Role of mass transfer on hydrogen evolution in aqueous media. *Journal of applied electrochemistry*, 28(1):10–17, 1998.
- [170] J. W. Lee, D. K.e Sohn, and H. S. Ko. Study on bubble visualization of gas-evolving electrolysis in forced convective electrolyte. *Experiments in Fluids*, 60(10):1–11, 2019.
- [171] R. Wedin and A. A. Dahlkild. On the transport of small bubbles under developing channel flow in a buoyant gas-evolving electrochemical cell. *Industrial & engineering chemistry research*, 40(23):5228–5233, 2001.
- [172] J. Schillings, O. Doche, and J. Deseure. Modeling of electrochemically generated bubbly flow under buoyancy-driven and forced convection. *International Journal of Heat and Mass Transfer*, 85:292–299, 2015.
- [173] D. Le Bideau, P. Mandin, M. Benbouzid, M. Kim, M. Sellier, F. Ganci, and R. a Inguanta. Eulerian two-fluid model of alkaline water electrolysis for hydrogen production. *Energies*, 13(13):3394, 2020.
- [174] A. Zarghami, N. G. Deen, and A. W. Vreman. Cfd modeling of multiphase flow in an alkaline water electrolyzer. *Chemical Engineering Science*, 227:115926, 2020.
- [175] J. Rodríguez and E. Amores. Cfd modeling and experimental validation of an alkaline water electrolysis cell for hydrogen production. *Processes*, 8(12):1634, 2020.
- [176] M. D. Mat and K. Aldas. Application of a two-phase flow model for natural convection in an electrochemical cell. *International journal of hydrogen energy*, 30(4):411–420, 2005.
- [177] A. B. Gol'dberg. Experimental verification of models for the bubble layer formed during gas evolution in vertical flow-through membrane cells. *Russian journal of electrochemistry*, 38(9):1025–1031, 2002.
- [178] H. Vogt. Instability of the two-phase flow in vertical interelectrode gaps. *Journal of applied electrochemistry*, 29(10):1155–1159, 1999.
- [179] L. R. Czarnetzki. *Aspects of electrochemical production of hypochlorite and chlorate*. PhD thesis, Chemical Engineering and Chemistry, 1989.
- [180] N. Riviere and A. Cartellier. Wall shear stress and void fraction in poiseuille bubbly flows: Part i: simple analytic predictions. *European Journal of Mechanics-B/Fluids*, 18(5):823–846, 1999.
- [181] M. Ishii. Thermo-fluid dynamic theory of two-phase flow. *NASA Sti/recon Technical Report A*, 75:29657, 1975.
- [182] *CFD Module User's guide v5.6*. COMSOL, 2020.
- [183] S. Orvalho, P. Stanovsky, and M. C. Ruzicka. Bubble coalescence in electrolytes: effect of bubble approach velocity. *Chemical Engineering Journal*, 406:125926, 2021.
- [184] G. Kreysa and M. Kuhn. Modelling of gas evolving electrolysis cells. i. the gas voidage problem. *Journal of applied electrochemistry*, 15(4):517–526, 1985.
- [185] R. R. Lessard and S. A. Zieminski. Bubble coalescence and gas transfer in aqueous electrolytic solutions. *Industrial & Engineering Chemistry Fundamentals*, 10(2):260–269, 1971.
- [186] M. Ishii and N. Zuber. Drag coefficient and relative velocity in bubbly, droplet or particulate flows. *AIChE journal*, 25(5):843–855, 1979.
- [187] I. M. Krieger and T. J. Dougherty. A mechanism for non-newtonian flow in suspensions of rigid spheres. *Transactions of the Society of Rheology*, 3(1):137–152, 1959.
- [188] R. Jamshidi, P. Angeli, and L. Mazzei. On the closure problem of the effective stress in the eulerian-eulerian and mixture modeling approaches for the simulation of liquid-particle suspensions. *Physics of Fluids*, 31(1):013302, 2019.
- [189] Y. Li, J.n Fu, Z. Geng, and H. Dong. Cfd simulations of shear induced migration in pressure-driven flow with non-brownian suspensions. *International Journal of Multiphase Flow*, 147:103918, 2022.
- [190] J. F. Richardson and W. N. Zaki. The sedimentation of a suspension of uniform spheres under conditions of viscous flow. *Chemical Engineering Science*, 3(2):65–73, 1954.
- [191] H. Nicolai, B. Herzhaft, E. J. Hinch, L. Oger, and E. Guazzelli. Particle velocity fluctuations and hydrodynamic self-diffusion of sedimenting non-brownian spheres. *Physics of Fluids*, 7(1):12–23, 1995.

- [192] H. Kellermann, G. Kreysa, et al. Dynamic modelling of gas hold-up in different electrolyte systems. *Journal of applied electrochemistry*, 28(3):311–319, 1998.
- [193] L. Sigrist, O. Dossenbach, and N. Ibl. On the conductivity and void fraction of gas dispersions in electrolyte solutions. *Journal of applied electrochemistry*, 10(2):223–228, 1980.
- [194] P. G. T. Saffman. The lift on a small sphere in a slow shear flow. *Journal of fluid mechanics*, 22(2):385–400, 1965.
- [195] J. B. McLaughlin. Inertial migration of a small sphere in linear shear flows. *Journal of fluid Mechanics*, 224:261–274, 1991.
- [196] R. Mei. An approximate expression for the shear lift force on a spherical particle at finite reynolds number. *International Journal of Multiphase Flow*, 18(1):145–147, 1992.
- [197] J. M. Ham and G. M. Homsy. Hindered settling and hydrodynamic dispersion in quiescent sedimenting suspensions. *International journal of multiphase flow*, 14(5):533–546, 1988.
- [198] S. Harada and R. Otomo. Diffusive behavior of a thin particle layer in fluid by hydrodynamic interaction. *Physical Review E*, 80(6):066311, 2009.
- [199] T. K. Perkins and O. C. Johnston. A review of diffusion and dispersion in porous media. *Society of Petroleum Engineers Journal*, 3(01):70–84, 1963.
- [200] V. Nguyen and D. V. Papavassiliou. Hydrodynamic dispersion in porous media and the significance of lagrangian time and space scales. *Fluids*, 5(2):79, 2020.
- [201] D. Leighton and A. Acrivos. Measurement of shear-induced self-diffusion in concentrated suspensions of spheres. *Journal of Fluid Mechanics*, 177:109–131, 1987.
- [202] D. Leighton and A. Acrivos. The shear-induced migration of particles in concentrated suspensions. *Journal of Fluid Mechanics*, 181:415–439, 1987.
- [203] J. Schillings, O. Doche, M. T. Retamales, F. Bauer, J. Deseure, and S. Tardu. Four-way coupled eulerian–lagrangian direct numerical simulations in a vertical laminar channel flow. *International Journal of Multiphase Flow*, 89:92–107, 2017.
- [204] H. Vogt. On the gas-evolution efficiency of electrodes. ii–numerical analysis. *Electrochimica Acta*, 56(5):2404–2410, 2011.
- [205] I. R. C. Krikke. Modeling the effect of dissolved gas on the bubble layer along a vertical gas evolving electrode. Master’s thesis, Delft University of Technology, The Netherlands, 2021.
- [206] T. Weier and S. Landgraf. The two-phase flow at gas-evolving electrodes: bubble-driven and lorentz-force-driven convection. *The European Physical Journal Special Topics*, 220(1):313–322, 2013.
- [207] D. Baczymalski, T. Weier, C. J. Kähler, and C. Cierpka. Near-wall measurements of the bubble-and lorentz-force-driven convection at gas-evolving electrodes. *Experiments in Fluids*, 56(8):1–13, 2015.
- [208] B. E. Bongenaar-Schlechter, L. J. J. Janssen, S. J. D. Van Stralen, and E. Barendrecht. The effect of the gas void distribution on the ohmic resistance during water electrolytes. *Journal of applied electrochemistry*, 15(4):537–548, 1985.
- [209] Y. Fukunaka, K. Suzuki, A. Ueda, and Y. Kondo. Mass-transfer rate on a plane vertical cathode with hydrogen gas evolution. *Journal of The Electrochemical Society*, 136(4):1002, 1989.
- [210] J. Hartmann. Hg-dynamics in a homogeneous magnetic field, part i. *Math. Phys. J., Copenhagen*, 15:6, 1934.
- [211] U. Müller and L. Bühler. Analytical solutions for mhd channel flow. In *Magneto-fluid dynamics in Channels and Containers*, pages 37–55. Springer, 2001.
- [212] K. Vafai, S. J. Kim, et al. Forced convection in a channel filled with a porous medium: an exact solution. *ASME J. Heat Transfer*, 111(4):1103–1106, 1989.
- [213] F. Hine and K. Murakami. Bubble effects on the solution ir drop in a vertical electrolyzer under free and forced convection. *Journal of the Electrochemical Society*, 127(2):292, 1980.
- [214] H. Vogt. Proposed prediction method for the frictional pressure drop of bubble-filled electrolytes. *Journal of Applied Electrochemistry*, 12(3):261–266, 1982.
- [215] J. F. Thorpe, J. E. Funk, and T. Y. Bong. Void fraction and pressure drop in a water electrolysis cell. *Journal of Basic Engineering*, 92(1):173–182, 1970.
- [216] F. Hine, M. Yasuda, Y. Ogata, and K. Hara. Hydrodynamic studies on a vertical electrolyzer with gas evolution under forced circulation. *Journal of the Electrochemical Society*, 131(1), 1984.
- [217] N. N. Clark and R. L. C. Flemmer. Two-phase pressure loss in terms of mixing length theory. 1. derivation for the general case of dispersed flow. *Industrial & engineering chemistry fundamentals*, 24(4):412–418, 1985.
- [218] V. E. Nakoryakov, O. N. Kashinsky, A. P. Burdukov, and V. P. Odnoral. Local characteristics of upward gas-liquid flows. *International Journal of Multiphase Flow*, 7(1):63–81, 1981.

- [219] B. Atkinson, M. P. Brocklebank, C. C. H. Card, and J. M. Smith. Low reynolds number developing flows. *AIChE Journal*, 15(4):548–553, 1969.
- [220] J. Eigeldinger and H.t Vogt. The bubble coverage of gas-evolving electrodes in a flowing electrolyte. *Electrochimica Acta*, 45(27):4449–4456, 2000.
- [221] D. Landolt, R. Acosta, R. H. Muller, and C. W. Tobias. An optical study of cathodic hydrogen evolution in high-rate electrolysis. *Journal of the Electrochemical Society*, 117(6):839, 1970.
- [222] J. W. Haverkort and H. Rajaei. Voltage losses in zero-gap alkaline water electrolysis. *Journal of Power Sources*, 497:229864, 2021.
- [223] M. T. de Groot and A. W. Vreman. Ohmic resistance in zero gap alkaline electrolysis with a zirfon diaphragm. *Electrochimica Acta*, 369:137684, 2021.
- [224] D. V. Esposito, Y. Lee, H. Yoon, P. M. Haney, N. Y. Labrador, T. P. Moffat, A. A. Talin, and V. A. Szalai. Deconvoluting the influences of 3d structure on the performance of photoelectrodes for solar-driven water splitting. *Sustainable Energy & Fuels*, 1(1):154–173, 2017.
- [225] A. Angulo, P. van der Linde, H. Gardeniers, M. Modestino, and D. F. Rivas. Influence of bubbles on the energy conversion efficiency of electrochemical reactors. *Joule*, 4(3):555–579, 2020.
- [226] B. K. Kim, M. J. Kim, and J. J. Kim. Impact of surface hydrophilicity on electrochemical water splitting. *ACS applied materials & interfaces*, 13(10):11940–11947, 2021.
- [227] T. F. Groß, J. Bauer, G. Ludwig, D. F. Rivas, and P. F. Pelz. Bubble nucleation from micro-crevices in a shear flow. *Experiments in fluids*, 59(1):1–10, 2018.
- [228] J. A. Koza, S. Mühlhoff, P. Żabiński, P. A. Nikrityuk, K. Eckert, M. Uhlemann, A. Gebert, T. Weier, L. Schultz, and S. Odenbach. Hydrogen evolution under the influence of a magnetic field. *Electrochimica Acta*, 56(6):2665–2675, 2011.
- [229] A. Rajora and JW Haverkort. An analytical model for the velocity and gas fraction profiles near gas-evolving electrodes. *International Journal of Hydrogen Energy*, 2023.
- [230] A. L. Perron, L. I. Kiss, and S. Poncsák. Mathematical model to evaluate the ohmic resistance caused by the presence of a large number of bubbles in hall-héroult cells. *Journal of applied electrochemistry*, 37(3):303–310, 2007.
- [231] R. K. B. Karlsson and A. Cornell. Selectivity between oxygen and chlorine evolution in the chlor-alkali and chlorate processes. *Chemical reviews*, 116(5):2982–3028, 2016.
- [232] P. Byrne, P. Bosander, O. Parhammar, and E. Fontes. A primary, secondary and pseudo-tertiary mathematical model of a chlor-alkali membrane cell. *Journal of applied electrochemistry*, 30(12):1361–1367, 2000.
- [233] K. Zeng and D. Zhang. Recent progress in alkaline water electrolysis for hydrogen production and applications. *Progress in Energy and Combustion Science*, 36(3):307–326, 2010.
- [234] M. Schalenbach, W. Lueke, and D. Stolten. Hydrogen diffusivity and electrolyte permeability of the zirfon perl separator for alkaline water electrolysis. *Journal of The Electrochemical Society*, 163(14):F1480–F1488, 2016.
- [235] L. J. J. Janssen. Effective solution resistivity in beds containing one monolayer or multilayers of uniform spherical glass beads. *Journal of Applied Electrochemistry*, 30(4):507–509, 2000.
- [236] C. Gabrielli, F. Huet, M. Keddam, A. Macias, and A. Sahar. Potential drops due to an attached bubble on a gas-evolving electrode. *Journal of applied electrochemistry*, 19(5):617–629, 1989.
- [237] R. Iwata, L. Zhang, K. L. Wilke, S. Gong, M. He, B. M. Gallant, and E. N. Wang. Bubble growth and departure modes on wettable/non-wettable porous foams in alkaline water splitting. *Joule*, 5(4):887–900, 2021.
- [238] H. Vogt. The incremental ohmic resistance caused by bubbles adhering to an electrode. *Journal of Applied Electrochemistry*, 13(1):87–88, 1983.
- [239] J. Dukovic and C. W. Tobias. The influence of attached bubbles on potential drop and current distribution at gas-evolving electrodes. *Journal of the Electrochemical Society*, 134(2):331, 1987.
- [240] J. K. Lee and A. Bazylak. Bubbles: the good, the bad, and the ugly. *Joule*, 5(1):19–21, 2021.
- [241] H. Vogt. Superposition of microconvective and macroconvective mass transfer at gas-evolving electrodes—a theoretical attempt. *Electrochimica acta*, 32(4):633–636, 1987.
- [242] K. Obata and F. Abdi. Bubble-induced convection stabilizes local ph during solar water splitting in neutral ph electrolytes. *Sustainable Energy & Fuels*, 2021.
- [243] R. Babu and Malay K. Das. Experimental studies of natural convective mass transfer in a water-splitting system. *International Journal of Hydrogen Energy*, 44(29):14467–14480, 2019.
- [244] P. Mandin, R. Wüthrich, and H. Roustan. Electrochemical engineering modelling of the electrodes kinetic properties during two-phase sustainable electrolysis. In *Computer Aided Chemical Engineering*,

- volume 27, pages 435–440. Elsevier, 2009.
- [245] M. Wang, Z. Wang, X. Gong, and Z. Guo. The intensification technologies to water electrolysis for hydrogen production—a review. *Renewable and Sustainable Energy Reviews*, 29:573–588, 2014.
- [246] C. W. Tobias, M. Eisenberg, and C. R. Wilke. Fiftieth anniversary: diffusion and convection in electrolysis—a theoretical review. *Journal of the Electrochemical Society*, 99(12):359C, 1952.
- [247] R. H. Müller and N. Ibl. Studies of natural convection at vertical electrodes. *Journal of the electrochemical society*, 105(6):346, 1958.
- [248] L. J. J. Janssen. Mass transfer at gas-evolving vertical electrodes. *Journal of applied electrochemistry*, 17(6):1177–1189, 1987.
- [249] A. Bejan. *Convection heat transfer*. John Wiley & sons, 2013.
- [250] E. M. Sparrow and J. L. Gregg. Laminar free convection from a vertical plate with uniform surface heat flux. *Transactions of the American Society of Mechanical Engineers*, 78(2):435–440, 1956.
- [251] M. Capobianchi and A. Aziz. A scale analysis for natural convective flows over vertical surfaces. *International journal of thermal sciences*, 54:82–88, 2012.
- [252] A. Guha and K. Pradhan. A unified integral theory of laminar natural convection over surfaces at arbitrary inclination from horizontal to vertical. *International Journal of Thermal Sciences*, 111:475–490, 2017.
- [253] R. S. Jupudi, Ho. Zhang, G. Zappi, and R. Bourgeois. Modeling bubble flow and current density distribution in an alkaline electrolysis cell. *The Journal of Computational Multiphase Flows*, 1(4):341–347, 2009.
- [254] X. Y. Wong, Y. Zhuo, and Y. Shen. Numerical analysis of hydrogen bubble behavior in a zero-gap alkaline water electrolyzer flow channel. *Industrial & Engineering Chemistry Research*, 60(33):12429–12446, 2021.
- [255] G. F. Swiegers, R. N. L. Terrett, G. Tsekouras, T. Tsuzuki, R. J. Pace, and R. Stranger. The prospects of developing a highly energy-efficient water electrolyser by eliminating or mitigating bubble effects. *Sustainable Energy & Fuels*, 5(5):1280–1310, 2021.
- [256] B. Gebhart, Y. Jaluria, R. L. Mahajan, and B. Sammakia. *Buoyancy-induced flows and transport*. New York, NY (USA); Hemisphere Publishing, 1988.
- [257] A. Raman, P. Peñas, D. v. d. Meer, D. Lohse, H. Gardeniers, and D. Fernández Rivas. Potential response of single successive constant-current-driven electrolytic hydrogen bubbles spatially separated from the electrode. *Electrochimica Acta*, 425:140691, 2022. ISSN 0013-4686.
- [258] L. Schiller. Über die grundlegenden berechnungen bei der schwerkraftaufbereitung. *Z. Vereines Deutscher Inge.*, 77:318–321, 1933.
- [259] C. Crowe, M. Sommerfeld, Y. Tsuji, et al. *Multiphase Flows with. Ž*, 1998.
- [260] R. Clift, J. R. Grace, and M. E. Weber. Bubbles, drops, and particles. 2005.
- [261] T. Hales, M. Adams, G. Bauer, T. D. Dang, J. Harrison, H. Le Truong, C. y Kaliszzyk, V. Magron, S. McLaughlin, T. T. Nguyen, et al. A formal proof of the kepler conjecture. In *Forum of mathematics, Pi*, volume 5. Cambridge University Press, 2017.
- [262] G. D. Scott. Packing of spheres: packing of equal spheres. *Nature*, 188(4754):908–909, 1960.
- [263] Z. Wang, J.M. Pereira, and Y. Gan. Packing of wet monodisperse spheres. *Powder Technology*, 378:60–64, 2021.
- [264] Y. De Strycker. A bubble curtain model applied in chlorate electrolysis. Master's thesis, Chalmers University of Technology, 2012.
- [265] P. Haug, B. Kreitz, M. Koj, and T. Turek. Process modelling of an alkaline water electrolyzer. *International Journal of Hydrogen Energy*, 42(24):15689–15707, 2017.
- [266] E. L. J. Coenen and L. J. J. Janssen. Voidage of bulk solution in a tall vertical gasevolving cell. *Journal of applied electrochemistry*, 27(10):1143–1148, 1997.
- [267] A. N. Colli and J. M. Bisang. Current and potential distribution in two-phase (gas evolving) electrochemical reactors by the finite volume method. *Journal of The Electrochemical Society*, 169(3):034524, 2022.
- [268] H. Vogt. The voidage problem in gas-electrolyte dispersions. *Journal of applied electrochemistry*, 17(2): 419–426, 1987.
- [269] P. C. Johnson and R. Jackson. Frictional–collisional constitutive relations for granular materials, with application to plane shearing. *Journal of fluid Mechanics*, 176:67–93, 1987.
- [270] C. Josserand, P.Y. Lagrée, and D. Lhuillier. Granular pressure and the thickness of a layer jamming on a rough incline. *EPL (Europhysics Letters)*, 73(3):363, 2005.
- [271] Z. Cheng, T. J. Hsu, and J. Calantoni. Sedfoam: A multi-dimensional eulerian two-phase model for sediment transport and its application to momentary bed failure. *Coastal Engineering*, 119:32–50, 2017.
- [272] P. Si, H. Shi, and X. Yu. A general frictional-collisional model for dense granular flows. *Landslides*, 16(3):

- 485–496, 2019.
- [273] P. Tiwari, S. P. Antal, and M. Z. Podowski. Modeling shear-induced diffusion force in particulate flows. *Computers & fluids*, 38(4):727–737, 2009.
- [274] H. Matsushima, Y. Fukunaka, and K. Kuribayashi. Water electrolysis under microgravity: Part ii. description of gas bubble evolution phenomena. *Electrochimica acta*, 51(20):4190–4198, 2006.
- [275] G. Desrayaud, E. Chénier, A. Joulin, A. Bastide, B. Brangeon, J. P. Caltagirone, Y. Cherif, R. Eymard, C. Garnier, S. Giroux-Julien, et al. Benchmark solutions for natural convection flows in vertical channels submitted to different open boundary conditions. *International journal of thermal sciences*, 72:18–33, 2013.
- [276] H. Sun, R. Li, E. Chénier, and G. Lauriat. On the modeling of aiding mixed convection in vertical channels. *Heat and Mass Transfer*, 48(7):1125–1134, 2012.
- [277] B. Brangeon, P. Joubert, and A. Bastide. Influence of the dynamic boundary conditions on natural convection in an asymmetrically heated channel. *International Journal of Thermal Sciences*, 95:64–72, 2015.
- [278] S. Hiraoka, I. Yamada, H. Mori, H. Sugimoto, N. Hakushi, A. Matsuura, and H. Nakamura. Mass transfer and shear stress on a vertical electrode with gas evolution. *Electrochimica acta*, 31(3):349–354, 1986.
- [279] A. Faghri, Y. Zhang, and J. R. Howell. *Advanced heat and mass transfer*. Global Digital Press, 2010.

LIST OF PUBLICATIONS

1. **A.Rajora** and J.W.Haverkort, *An analytical model for the velocity and gas fraction profiles near gas evolving electrodes*, [International Journal of Hydrogen Energy](#) (2023)
2. **A.Rajora** and J.W.Haverkort, *An analytical multiphase flow model for parallel plate electrolyzers*, [Chemical Engineering Science](#) **260**, 117823 (2022).
3. H. Rajaei, **A.Rajora** and J.W.Haverkort, *Design of membraneless gas-evolving flow-through porous electrodes*, [Journal of Power Sources](#) **491**, 229364 (2021).
4. **A.Rajora** and J.W.Haverkort, *An analytical model for liquid and gas diffusion layers in electrolyzers and fuel cells*, [Journal of The Electrochemical Society](#) **168.3**, 034506 (2021).

ACKNOWLEDGMENTS

From the teacher is learned a quarter, a quarter from the student's own intelligence, a quarter from fellow students, and a quarter with the passage of time.

Commentary by Haradatta on the Āpastamba Dharmasūtra (1.7.29), 11th century

Today, I look back at my Ph.D. journey with calm satisfaction that enriched me with its experiences and lifelong lessons. But first, I want to acknowledge the support of many wonderful people who contributed in their ways to help me reach this milestone.

I want to express my gratitude to my co-promotor and daily supervisor, Dr. Willem Haverkort, who impacted my work most. You gave me enormous freedom while ensuring that I learned the art of perseverance. You kept me motivated and believed in me even when I wasn't sure of myself. You were always available, even during your vacations, and still are to this date. I do not think using the words "thank you" sums up my admiration and gratitude. It has been a privilege to learn from you and to be your first Ph.D. candidate.

I am sincerely grateful to my promotor, Prof. Johan T. Padding, for your valuable feedback during my progress meetings and for helping me navigate the administrative responsibilities. Thank you for motivating me and supporting me during this Ph.D.

I would also like to thank my M.Sc. supervisor, Dr. Rene Pecnik, for apprising me of this position and steering me toward the Ph.D. journey. Thank you for inculcating a sense of scientific integrity and believing in my potential. I want to thank my previous mentors, Dr. Prabal Talukdar at IIT Delhi and Dr. Amit Tyagi at IIT(BHU) Varanasi, who also shaped my scientific curiosity through their guidance and support. I also want to express my gratitude to my childhood mentor, Mr. Himanshu Bhaskar, who has been like an elder brother to me. Your teachings, belief, and support were crucial in my formative years, and I am grateful you were there for me. I express my gratitude to my office mates: Hadi, Nico, Joe, Wouter, Arvind, and Sohan, for the engaging discussions and occasional bantering. I also extend my sincere gratitude to all department personnel who handled my administrative requests with a smile. I would also like to thank the committee members for taking the time to evaluate my dissertation.

My Ph.D. journey is the most demanding but rewarding adventure I have embarked on. However, the foundation for the enormous grit required to undertake such a task was laid long before I took this path. I am fortunate to be born to two of the most dedicated, loving, and hard-working people: Dr. Vijendra Singh Rajora and Mrs. Shikha Rajora. Mummy, you are the wind that has kept me afloat with your unconditional love and support. Papa, your work ethic, values, and constant life lessons about the power of hard work and dedication have made this journey a lot easier. You have reminded me that education is not just about knowing something but understanding it. You both have toiled hard and ensured your children get a better life. My success is a result of your silent sacrifices. I am also grateful for the unrestricted love and support I received from my father-in-law, Mr. Surendra Singh Chahar. Your blessings and prayers have always given me strength. Through you, I have rediscovered the meaning of faith and how it keeps us calm during difficult situations.

I want to express my appreciation to my brother, Dr. Rishav, who has been my idol. I have, knowingly or unknowingly, seen him as a source of inspiration. Looking back, I always think I

chose to be a mechanical engineer because he is also a mechanical engineer. His Ph.D. journey and his advice have helped me cope with the pressure. He always makes me feel safe and loved. I also want to express my gratitude to my very supportive sister-in-law, Tina, who has taught me to be cheerful even in the darkest moments. I want to also express my appreciation to my sister-in-law, Shubhangi, and brother-in-law, Parth, who have been very supportive during my Ph.D. Every conversation with you has made me feel loved, and you have reminded me that there are countless people who support me.

Speaking about my support group, my journey was made easier with the wonderful company of my friends, who have always brought out the best in me. I am particularly proud of my friendships with Dr. Manu, Arusha, Anand, Pallavi, Aditya, Deepak, Harshit and Vivek, who have always cheered me up. Vivek, you were the selflessness personified and have left an indelible mark on my life. I am grateful for the time I could spend with you. You have left this world, but for me, you will always be alive in my heart. Special thanks to Anand, who has been there since the beginning of this journey, pulling me out of my moments of despair and sharing many memorable moments.

As this journey ends, I look at you, Pooja, the love of my life and my constant. You have given me support, optimism, and joy in every little moment. Thank you for being there for me unconditionally and walking with me through this journey. You have always believed in me and always pushed me to be better version of myself. With you on my side, I can brave any hurdle. You are my happy place, and this journey belongs not to me but us.

*Aviral
Delft, January 2023*

ABOUT MYSELF

Born on February 5, 1991, in Pantnagar, Uttarakhand, India, I grew up in a vibrant and intellectually stimulating environment that nurtured my thirst for knowledge. This drive led me to excel academically, and in 2006, I was honored with the prestigious National Talent Search Scholarship in India.

In 2013, I earned my Bachelor of Technology degree in Mechanical Engineering with distinction from the esteemed Indian Institute of Technology (BHU), Varanasi, India. Upon graduation, I set out on a professional journey that encompassed both industry and research experiences. Initially, I worked as a Sales Manager at Bharat Petroleum Corporation Limited, India, for a period of six months. This experience allowed me to gain valuable insights into the corporate world while honing my interpersonal skills.

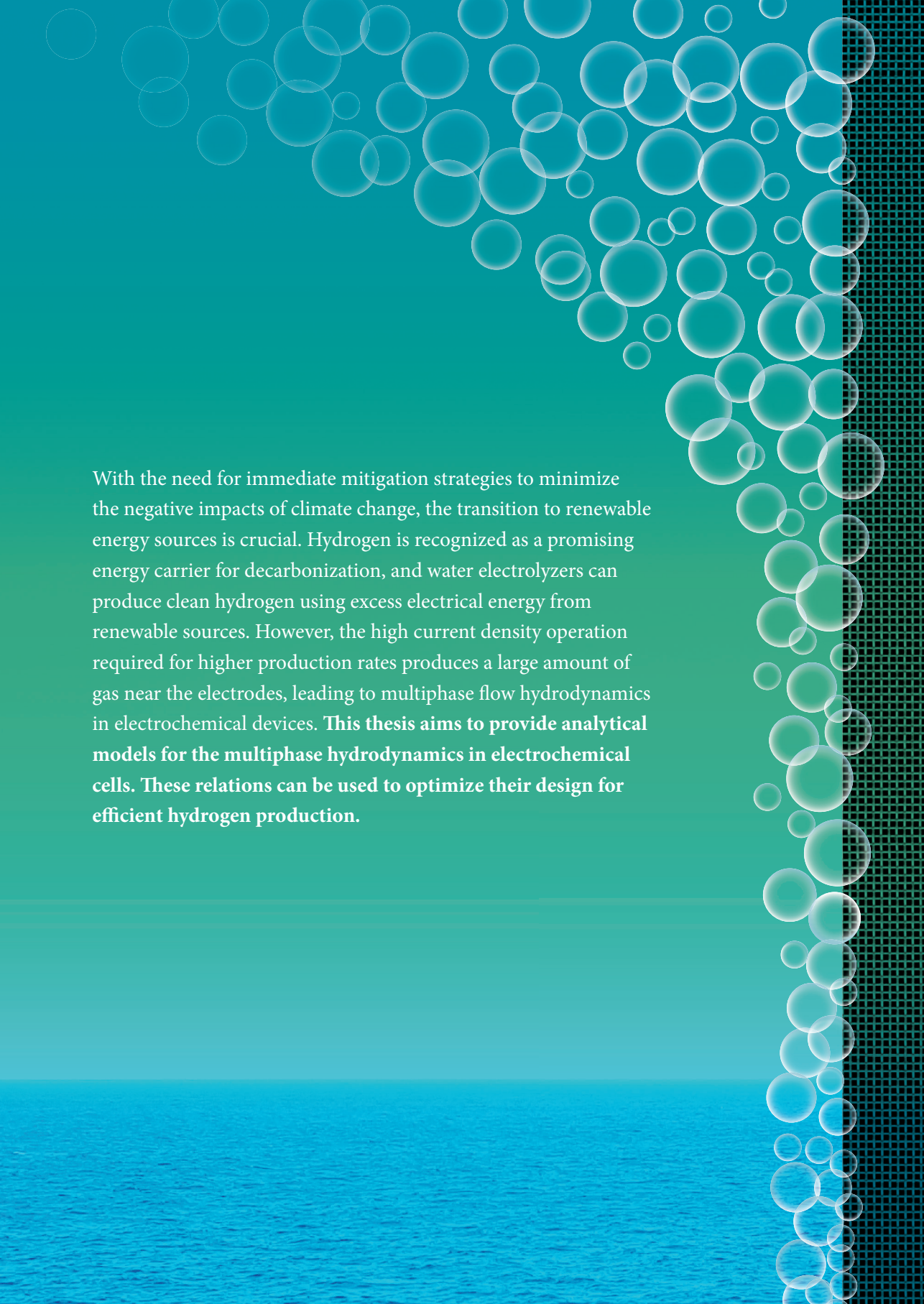
Recognizing my passion for research, I joined the Indian Institute of Technology, Delhi as a junior research fellow. During this enriching one-year, I delved into the field of heat transfer and discrete phase modeling in a pusher-type reheating furnace, marking my initiation into the world of research.

Seeking further academic growth, I made a significant decision to pursue a Master of Science degree in Mechanical Engineering with a specialization in solid and fluid mechanics at the renowned Delft University of Technology in The Netherlands in 2015. Under the guidance of Dr. Rene Pecnik, I embarked on a captivating graduation research project, employing direct numerical simulations to investigate the influence of heated particles on heat transfer in a turbulent channel flow. This endeavor deepened my understanding of multiphase flows.

Fueling my enthusiasm for scientific exploration, I commenced my Ph.D. research journey at the Delft University of Technology in April 2018, under the guidance of Dr. Willem Haverkort. Over the course of my doctoral studies, I delved into diverse research areas, harnessing my expertise in multiphase flows to create new mathematical models for electrochemical systems. The culmination of these efforts forms the foundation of the research presented in this work.

To apply my expertise in a practical context, I recently joined BattolyserSystems as a CFD Engineer in January 2023. In the future, I intend to leverage my knowledge in multiphase flows to develop solutions that create tangible impact in addressing practical challenges related to sustainability and driving meaningful progress.





With the need for immediate mitigation strategies to minimize the negative impacts of climate change, the transition to renewable energy sources is crucial. Hydrogen is recognized as a promising energy carrier for decarbonization, and water electrolyzers can produce clean hydrogen using excess electrical energy from renewable sources. However, the high current density operation required for higher production rates produces a large amount of gas near the electrodes, leading to multiphase flow hydrodynamics in electrochemical devices. **This thesis aims to provide analytical models for the multiphase hydrodynamics in electrochemical cells. These relations can be used to optimize their design for efficient hydrogen production.**